Computational Simulation of Faraday Probe Measurements

by

Jeremiah J. Boerner

A dissertation submitted in partial fulfillment
of the requirements for the degree of
Doctor of Philosophy
(Aerospace Engineering)
in The University of Michigan
2008

Doctoral Committee:

Professor Iain D. Boyd, Chair
Professor Yue Ying Lau
Professor Alec D. Gallimore
Professor Michael Keidar, George Washington University

"Thou dost not see the humor of it? Yet there is humor in all things, even in this!"

W. S. Gilbert and Sir Arthur Sullivan, *Yeomen of the Guard*

Dedicated to my teachers through all the years.

ACKNOWLEDGEMENTS

First and foremost, I am indebted to my advisor Iain D. Boyd. Without his initial and continuing support I would have given up on grad school long ago. Iain provided a comfortable and challenging research environment, and shielded me from the vagaries of funding. He provided much needed insight and guidance when the course of my research changed, and handled my lengthening stay at Michigan with aplomb. All the while he maintained the understanding attitude and soft touch that allowed me to pursue other interests far beyond the scope of aerospace engineering. I cannot thank him enough, and will always look to him as a model advisor.

All the members of my committee have been understanding and generous with their time, and I thank them heartily for that. Each of them invested in me during my time at Michigan, whether it was teaching the science of plasma physics or the art of teaching.

Y.Y. Lau taught one of the best introductory plasma courses I could imagine, and imparted a gut-level understanding and intuition of the physics of plasmas. With that in place, the mathematics comes naturally. His challenging particle kinetic lectures paved the way for my understanding and application of kinetic sheath models.

Michael Keidar asked many valuable questions and encouraged countless refinements of my conference presentations through the years. His insight into how plasma sheath models actually work has been very helpful.

Alec Gallimore lead me through my first electric propulsion course, and later

took me on as a GSI for his Aero 225 class. From taking his classes I learned the fundamental differences between undergrad and grad student understanding, along with the fascinating science of space propulsion. From teaching with him I began to understand exactly how challenging it is to teach well. His easygoing style and friendly personality extend far beyond the classroom, and have earned my deep respect.

There are many other faculty members at the university that I want to thank for helping me along the way: Professor Gilgenbach of NERS taught me the practical use of probe diagnostics, and revealed the arcana of electron plasma measurements. Professor Drake of AOSS showed me the rich and varied complexity of MHD plasmas, and convinced me that pulling a rabbit out of a hat does not count as a valid derivation. Professors Bernal, Dahm, and VanLeer taught me how to see something from the varied viewpoints of empirical relation, mathematical formalism, and physical intuition, and that having all three starts to feel like comprehension.

There are professionals in many places that I want to thank for the support, guidance, and great stories I shared in. Lee Johnson and JPL supported my research and gave critical guidance early on. John "Mike" Fife, Doug VanGilder, and Matt Gibbons introduced me to summer consulting at the Edwards AFRL modeling group. Matt Santi, Shannon Cheng, and Lubos Brieda taught me code-fu on the COLISEUM team.

Then there are all the friends and adopted family who provided me with support, moral and otherwise. Over the years I lived, worked, and played with more than a generation of NGPD research group members. I got started in recreational DSMC in Kooj's basement with the likes of Matt McNenly, Jerry Emhoff, John Yim, and Anton VanderWyst; ran MONACO with Chunpei Cai; climbed rock walls with Jose

Padilla; and diversified to practical molecular dynamics at Colonial Lanes with Tyler Huismann, Ethan Eagle, Tim Deschenes, Andy Porwitzky, and all their special lady friends. Outside of aerospace I trod the boards of Lydia Mendelssohn in the company of Lori Gould, Lawrence Bryk, and Matt Grace. So much of the warmth and happiness that I know in Ann Arbor comes from them, and I can only hope I reflect it back as brightly.

Last but never least, I have the most amazing family. Even hundreds of miles away, my parents have been close and supportive. Dad is always practical, dependable, and quick to make light of things. Mom cares and worries and prays for the best, and doesn't let me forget the greats in my past. Josh, Nate, Zach, and Ashley have given me fond memories, quiet inspiration, reminders to be humble, and a reason for trying harder. I wouldn't have gotten here, and I wouldn't even be me, without them.

TABLE OF CONTENTS

CHAPTER

LIST OF FIGURES

Figure

LIST OF TABLES

Table

LIST OF NOMENCLATURE

Acronyms

CEX	Charge EXchange
CFD	Computational Fluid Dynamics
DSMC	Direct Simulation Monte Carlo
EP	Electric Propulsion
LVTF	Large Vacuum Test Facility
MHD	MagnetoHydroDynamics
PIC	Particle In Cell
PEPL	Plasmadynamics and Electric Propulsion Lab
RPA	Retarding Potential Analyzer
VHS	Variable Hard Sphere

Constants

k_B	Boltzmann constant, 1.381×10^{-23} $\left[\frac{\mathrm{J}}{\mathrm{K}}\right]$
e	electron charge, 1.602×10^{-19} [C]
m_e	electron mass, 9.109×10^{-31} [kg]
g	standard gravity, 9.809 $\left[\frac{\mathrm{m}}{\mathrm{s}^2}\right]$
μ_0	permeability of free space, $4\pi \times 10^{-7}$ $\left[\frac{\mathrm{N}}{\mathrm{A}^2}\right]$
ε_0	permittivity of free space, 8.854×10^{-12} $\left[\frac{\mathrm{C}^2}{\mathrm{Nm}^2}\right]$

Symbols

$\mathbf{a}$	acceleration $\left[\frac{\mathrm{m}}{\mathrm{s}^2}\right]$
v_B	Bohm velocity $\left[\frac{\mathrm{m}}{\mathrm{s}}\right]$

$\triangle v$	change in velocity $\left[\frac{\mathrm{m}}{\mathrm{s}}\right]$
σ_{ab}	collision cross section $[\mathrm{m}^2]$
I	current [A]
λ_D	Debye Length [m]
ρ	density $\left[\frac{\mathrm{kg}}{\mathrm{m}^3}\right]$
$f(\mathbf{x}, \mathbf{v}, t)$	distribution function $[-]$
$\mathbf{E}$	electric field vector $\left[\frac{\mathrm{V}}{\mathrm{m}}\right]$
κ	electrical conductivity $\left[\frac{\mathrm{S}}{\mathrm{m}}\right]$
ν_e	electron collision frequency $\left[\frac{1}{\mathrm{s}}\right]$
μ_e	electron collision reduced mass [kg]
n_e	electron number density $[\mathrm{m}^{-3}]$
$\mathbf{j}_e$	electron current density $\left[\frac{\mathrm{A}}{\mathrm{m}^2}\right]$
T_e	electron temperature [K]
w	exchange frequency $\left[\frac{1}{\mathrm{s}}\right]$
W	exchange frequency, normalized by the plasma frequency $[-]$
$H(M)$	Heaviside function $[-]$
Z_i	ion charge state $[-]$
n_i	ion number density $[\mathrm{m}^{-3}]$
m_i	ion mass [kg]
T_i	ion temperature [K]
τ	ion to electron temperature ratio $[-]$
Kn	Knudsen number, ratio of mean free path to reference length $[-]$
M	Mach number, ratio of flow speed to a characteristic speed $[-]$
$\mathbf{B}$	magnetic field vector [T]
m	mass [kg]
$\dot{m}$	mass flow rate $\left[\frac{\mathrm{kg}}{\mathrm{s}}\right]$
λ_{MFP}	Mean free path [m]

ω_P	plasma frequency $\left[\frac{1}{\mathrm{s}}\right]$
ϕ	plasma potential [V]
Φ	plasma potential, normalized by the electron temperature [−]
P	pressure $\left[\frac{\mathrm{N}}{\mathrm{m}^2}\right]$
$\mathbf{x}$	position vector [m]
z	sheath position; often normalized by the Debye length [m]
I_{sp}	specific impulse [s]
σ	thermal conductivity $\left[\frac{\mathrm{J}}{\mathrm{m \cdot s \cdot K}}\right]$
T	thrust [N]
t	time [s]
$\mathbf{v}$	velocity vector $\left[\frac{\mathrm{m}}{\mathrm{s}}\right]$
V	voltage [V]

Chapter I

Introduction and Overview

Plasma diagnostics are one of the key supporting technologies in every area of plasma physics. In plasma confinement research, immersed probe diagnostics and non-intrusive optical diagnostics make experimental measurements of the basic properties of the plasma. In plasma accelerator and electric propulsion research, the diagnostics measure plasma properties in order to infer performance and operating characteristics. In materials processing applications, diagnostics ensure that the desired plasma conditions are sustained in order to produce the desired surface treatment. For each of these examples, plasma diagnostics provide feedback and measurements that help guide the research or operation to achieve a desired goal.

In general, it is assumed that some quantity measured by the plasma diagnostic can be related back to a desired property in the plasma. For example, the slope of collected current with respect to bias voltage in the I-V characteristic of a Langmuir probe can be related to the electron temperature. Many diagnostic instruments have been developed to extract information about the flow. The drift current can be measured with Faraday probes, the ion velocity can be visualized with laser-induced fluorescence, the electron number density can be found with microwave interferometry, the plasma potential and electric fields can be measured with emissive probes, the ion energy spectrum can be calculated with retarding potential analyzers, and ion charge states can be identified with E×B probes. Of course, many of these instruments can be used to measure more than one plasma property, and for many properties there is more than one measurement technique.

The diagnostics are interpreted by relating a directly measured property, such as collected current, to the desired plasma property. The relation is often developed from elementary principles by making certain assumptions about the plasma. Returning to the Langmuir probe example, the electrons are assumed to have a Maxwellian velocity distribution so that the logarithmic slope of the I-V characteristic is inversely proportional to the electron temperature [1]. These assumptions commonly include a Maxwellian distribution of electron velocities, the Boltzmann relation between electron density and plasma potential, and a lower temperature for ions than for electrons. The measurements are assumed to accurately obtain the plasma properties, provided the plasma conditions meet the assumptions of the diagnostic theory.

In diagnostic theory it is assumed that the instrument does not significantly affect the properties of the plasma at the point where measurements are taken. This assumption is not valid for probe diagnostics in particular, and it is acknowledged that some disturbance is unavoidable. Theory for the plasma sheath on an immersed surface helps to identify and quantify some of the disturbances caused by the probe. The diagnostic techniques for some instruments take the plasma sheath into account in order to relate the measured properties to “undisturbed” plasma properties. However, sheath theory is limited to the effects in the electrostatic or electromagnetic sheath within a few Debye lengths of the probe surface. Diagnostic theory does not account for the effects at longer range, since those effects are not well understood.

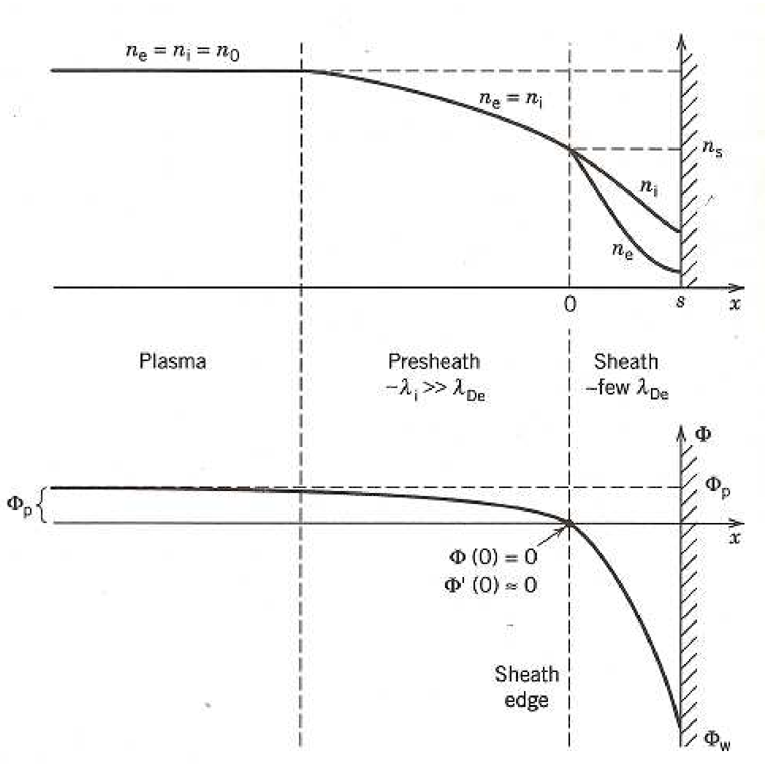

Figure 1.1: Schematic of plasma properties in the collisionless sheath [1].

1.1 Sheaths and other probe disturbances

An immersed diagnostic instrument perturbs the plasma properties in its vicinity. Electric and magnetic fields can penetrate the plasma up to a few Debye lengths from the probe, influencing the charged particle trajectories in the sheath. Farther from the probe, the collective shielding effect isolates the bulk plasma from the fields. The transition from bulk plasma through the sheath to a probe surface is shown schematically in Fig. 1.1. For a positive ion plasma, the electrons are the sole negative charge carriers and are more mobile than the ions. This leads to unequal fluxes to a surface at the same potential as the plasma, with more electrons than ions reaching the surface. If the surface is floating, it will accumulate a net negative charge that repels electrons and attracts ions until the net current is zero.

Sheaths comprise some of the most enduring and widely encountered problems in plasma physics. Langmuir and Tonks investigated sheaths in plasma arc and glow discharges in the late 1920's [2], identifying the major features of the collisionless electrostatic sheath and obtaining analytical solutions for simple geometries.

Bohm investigated the current collection of Langmuir probes in the late 1940's, and established the broadly applicable Bohm criterion for the formation of a steady sheath [3]. The criterion has since been generalized for finite temperature ion distributions and arbitrary ion distributions.

Developments in the 1980's and 1990's produced a kinetic description of the sheath and presheath for application to the strongly flowing plasmas encountered in space environments and fusion plasmas [4, 5, 6]. More recently, much attention has been focused on developing a consistent method to span the interfaces between plasma, presheath, and sheath [7, 8, 9, 10]. This work is motivated in part by the unphysical result in the Bohm sheath solution that the sheath is infinitely long, and that the electric fields at the sheath edge are asymptotically large.

An immersed probe can also affect the flow over longer length scales, since the flow either collides with the probe body or is diverted around the physical obstruction. This can potentially introduce flow features including compression regions upstream of the probe and rarefaction regions in the wake of the probe. Since experimental diagnostic probes are not perfectly absorbing, ions that collide with a probe surface can be neutralized and reflected back into the flow. The neutral gas diffuses away from the probe, extending the region that is perturbed by the probe. Charge exchange or momentum exchange collisions with the neutral gas also have an effect on the overall flow.

The photograph of a Faraday probe in the plume of a Hall thruster in Fig. 1.2 is evocative of the large scale disturbances that can be caused by the probe. The

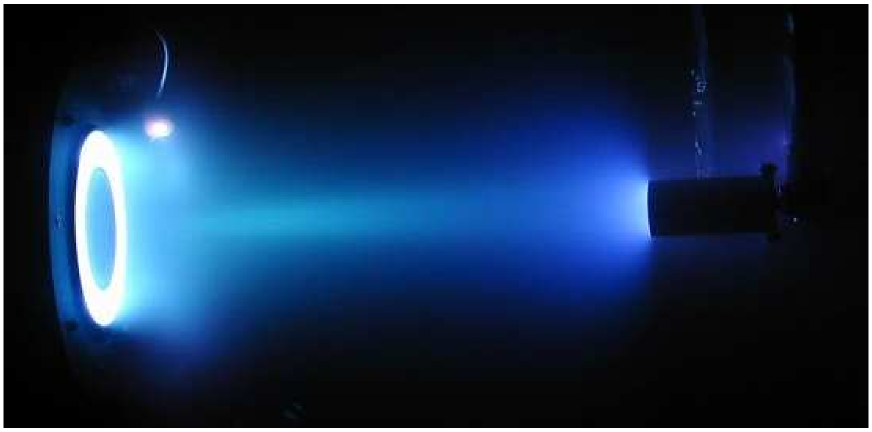

Figure 1.2: Photograph of a Hall thruster plume interacting with a Faraday probe [11].

visible light is associated with recombination and relaxation of excited electronic states in the plasma. A very bright region is apparent at the front surface of the probe, suggesting that there is a region of increased density that promotes collisional relaxation and recombination events.

A quantitative demonstration of the long range effect of the probe can be seen in experimental contours of plasma potential around a Faraday probe in Fig. 1.3, as reported by Walker *et al.* in Ref. [12]. The probe is cylindrical, with the axis of the probe aligned with the Y axis in the figure. In that work the Debye length is estimated as $\lambda_D = 0.3\,\text{mm}$. The observed plasma potential variations extend 2 cm or more from the probe, which is on the order of tens of Debye lengths. The weak fields that extend far from the probe contribute to sheath expansion, where the effective collecting area of the probe is increased due to electrostatic focusing of the ions.

The difference in plasma potential between the left and right sides of the probe is described as a shadowing effect. The bulk velocity of the ions is not aligned with the probe axis, and the electric fields are too weak to turn high speed ions into the region “behind” the probe. This is a second long range effect, and is due to the physical

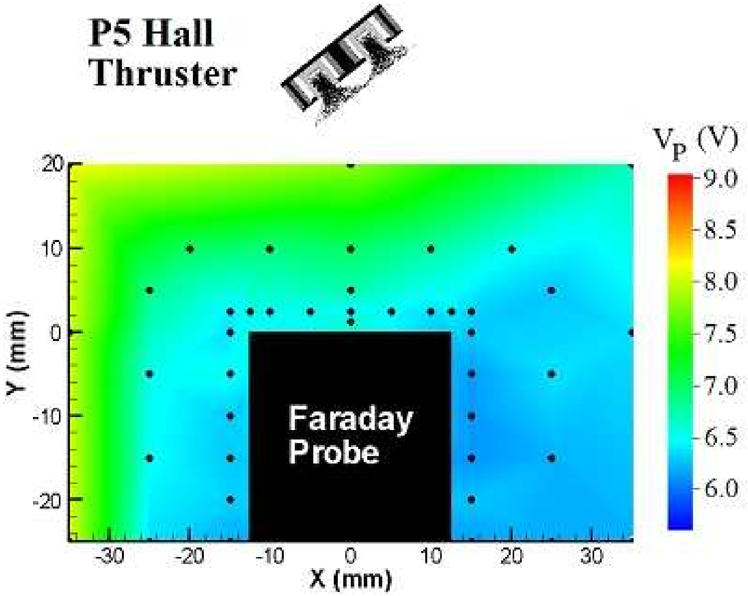

Figure 1.3: Experimental contours of plasma potential around a Faraday probe, courtesy Allen Victor [12].

obstruction of the flow.

The electrostatic sheath on the front surface of the probe should not alter the total current collected at the surface, except near the outer radial edge of the probe where the sheath curves to join the sheath along the side of the probe body. The standard design practice for experimental Faraday probes takes this into account and includes an annular guard ring to eliminate edge effects on the collecting surface. Sheath expansion is not as well-understood, so there are no standard design guidelines or operational methods to ensure that sheath expansion has minimal effect on the measured properties.

Shadowing is unlikely to affect properties on the front surface of the probe, but it would have a significant impact on the properties on the back face of the probe. The effects become especially important in experimental configurations with reversed Faraday probes, which measure the collected current on the wake side of the probe. Shadowing and other long range disturbances are not well-understood either, and there are no design or operational guidelines to account for the effects.

1.2 Objectives of this work

The purpose of this dissertation is to investigate how an immersed Faraday probe affects a plasma flow, and to quantify how the properties measured at the probe surface are related to the "undisturbed" plasma properties that would exist if the probe were not present. Additionally, the results of the investigations are interpreted to give recommendations for the design and use of Faraday probes. This work is conducted using computational techniques in order to achieve a very controlled setting where the undisturbed plasma conditions are known at the outset.

Since plasma properties such as ion density and electron temperature can vary by orders of magnitude in different applications, this dissertation is limited to the conditions relevant to electric propulsion (EP) plasmas. Faraday probes are widely used in experimental investigation of EP devices, and a wealth of information is available in the literature. This facilitates the selection of consistent plasma conditions, and limits the scope of this dissertation to a manageable set of plasma models.

1.2.1 Develop computational models of the plasma flow

The first overarching objective of this dissertation is to accurately describe the plasma flow field around a Faraday probe. Although fully analytical solutions or direct simulations are not practical for the full flow problem, many of the same concepts and techniques can be used to develop and apply simpler models. Several milestone objectives build up to the computational simulations of the flow field that are the first goal in this work:

1. Develop and use simple one dimensional models that include the relevant phys-

ical mechanisms for plasma-probe interactions.

2. Identify significant flow features in the one dimensional model results and establish a baseline for comparison with more sophisticated models.
3. Develop more accurate models that better represent the actual flow geometry and conditions. This includes moving to higher dimensional models and eliminating the assumptions made in the one dimensional models.
4. Compare results from the improved model with previous models to assess the usefulness and accuracy of the simpler models.

Two important supporting tasks in this process are developing flexible model implementations, and ensuring the reliability of the models. Eventually a range of different plasma conditions and probe geometries are simulated, so the models should be implemented in a flexible and general manner. The models must also be computationally stable and produce physically meaningful results.

1.2.2 Quantify the plasma-probe interactions

The second overarching objective of this dissertation is to evaluate how the plasma flow features and the probe measurements are affected by changing the inflowing plasma properties and the probe operational methods. In this stage the simple plasma conditions typically assumed in standard diagnostic theory are modified. The goal is to evaluate how the properties measured at the probe change in response to the modified plasma conditions. Similarly, the operational parameters of the Faraday probe are modified for a fixed plasma distribution. The purpose is again to evaluate how measured properties at the probe are affected as a result of changing the probe conditions.

The ion inflow distribution is modified incrementally until ultimately it is representative of the complex exhaust plasma generated by an EP thruster. The final distribution includes high energy beam ions, low energy charge exchange ions, and multiple charge species. Incremental modification of plasma conditions serves to isolate the effects of each of these components. Results from these simulations are compared against the simpler one dimensional models to assess the impact and relative importance of changing the inflow plasma properties.

The investigations of alternative Faraday probe operating conditions are conducted with a fixed set of realistic plasma conditions. The first investigation of the probe operation condition varies the probe bias potential. This allows the effect of sheath expansion to be observed and assessed in terms of the collected current at the probe surface. The second investigation of probe operation conditions varies the guard ring bias relative to the collecting surface bias. The intent in this study is to identify whether the total collected current varies significantly if there is a mismatch in the bias potential on the guard ring and on the collecting surface.

Additionally, the reversed Faraday probe is simulated to obtain an understanding of the flow field in the wake of the probe. These simulations require a much larger computational domain and would take a prohibitively long time to complete using the original models. As a supporting task, a multigrid method is developed and implemented to enable the reversed Faraday probe simulations to be carried out in an acceptable time.

1.2.3 Make recommendations for Faraday probe design and use

The final major objective of this dissertation is to make recommendations for the design and use of Faraday probes based on the results of the computational simulations. No conflicts are found with the current standard practices for Faraday probe usage. The flow field in the wake of the reversed Faraday probe is more complicated than might be expected, and a few precautionary recommendations are justified.

1.3 Organization

This dissertation is arranged as a linear sequence that starts with a review of experimental and numerical research related to electric propulsion (EP). Chapter II introduces some of the history and elementary concepts of EP, and describes the benefits that make EP such an attractive technology. A selection of the numerous experimental and numerical research activities related to EP are also described, which will inform many decisions about the plasma conditions and numerical models considered in this work. This also provides a perspective on the need for computational study of the interaction between plasmas and diagnostic probes.

In Chapter III, kinetic theory and the magnetohydrodynamic fluid equations are introduced as very general descriptions of a plasma. These descriptions are simplified to obtain analytic solutions for the sheath. The kinetic model leads to a geometric shadowing sheath, where the physical obstruction of the probe is the mechanism that creates sheath features. The MHD fluid equations lead to the planar Bohm sheath, where the electrostatic field drives the properties in the sheath.

Both kinetic and fluid descriptions of a plasma are used to develop an axisymmetric hybrid fluid particle computational code in Chapter IV. The Particle In

Cell (PIC) and Direct Simulation Monte Carlo (DSMC) kinetic models are used for the heavy ion and neutral particles. Three electron fluid models are developed: the Boltzmann model, the non-neutral detailed model, and the Poisson-consistent detailed model. The Boltzmann model is the simplest of the three, and uses the Boltzmann relation to greatly simplify the fluid equations. The non-neutral detailed model uses the full set of fluid equations, and is modified from a previous neutral treatment. The Poisson-consistent detailed model is also derived from the full set of fluid equations, but is manipulated from the outset as a non-neutral model.

The hybrid fluid PIC computational code is used extensively in Chapter V to perform simulations of the plasma flow field around an axisymmetric geometry that represents a Faraday probe. The Boltzmann fluid model is used in a series of studies to investigate how varying the plasma properties affects flow structures in the sheath and the simulated collected current at the probe surface. These studies make incremental changes to the inflow ion distribution function from a cold ion beam to a complex composite distribution constructed from multiple drifting Maxwellian components. The Boltzmann model is also used to study how the operation of the Faraday probe affects the simulated collected current at the probe surface. These studies involve changing the bias of the guard ring relative to the collecting surface or sweeping the probe bias over a range of ion collecting conditions. In all of these studies, the planar Bohm sheath is found to be a reliable predictor for the properties in the sheath.

The non-neutral detailed model and the Poisson consistent models are also used in Chapter V. The non-neutral detailed model is shown to have a serious procedural flaw and is not developed further. The Poisson-consistent model is used successfully to repeat the studies pertaining to ion inflow distribution. The results from these simulations are generally in very good agreement with the Boltzmann model result and the planar Bohm sheath. The only notable exception is when the ion inflow distribution has a significant backflow component. The present implementation of the hybrid fluid PIC model only introduces particles at the upstream and outer edges of the domain, so any backflow component is not well represented.

The hybrid fluid PIC model requires considerable time to run, making it impractical for simulations on larger domains. The computational code is profiled in Chapter VI, revealing that the particle models account for a disproportionately large fraction of the total time. A multigrid method is implemented to solve the PIC model on a coarse grid and solve the electron fluid model on a fine grid. This reduces the computational time spent in the particle models and maintains the grid resolution required for accurate fluid model solutions.

The multigrid version of the code is used to perform simulations of a reversed Faraday probe in Chapter VII. The computed flow field on the wake side of the probe is significantly more complicated than on the ram side of the probe. The simplistic structure predicted from the geometric sheath model does not accurately reflect the actual structures. The numerical simulations also provide an estimate of the exchange frequency, which is an unknown parameter in the geometric shadowing model. Profiles of the exchange frequency show features that are not compatible with the assumptions made in the geometric shadowing model. In these studies, the geometric shadowing model is shown to be a poor predictor of sheath properties.

The dissertation is concluded in Chapter VIII with a review and summary of the results and new contributions of this work. This includes assessment of the analytic sheath models and the numerical models, an evaluation of the multigrid scheme, and discussion of the probe simulations. In fulfillment of the objectives of this dissertation, suggestions are made regarding the design and use of Faraday probes. Finally, a few recommendations for future work in this area are outlined.

Chapter II

Background and Motivation

The work described in this dissertation is performed in the context of electric propulsion research. This setting guides many decisions about the relevant physical processes and representative conditions of interest. It is therefore useful to introduce electric propulsion and some of the active research in that area. This chapter is additionally intended to identify some of the challenges and outstanding questions that this research is intended to address.

2.1 Electric propulsion

Electric propulsion, or EP as it is often abbreviated, refers to spacecraft propulsion systems that utilize electrical processes rather than chemical reactions to accelerate a propellant. EP systems have been in development since the 1960s, although the underlying concepts were described and investigated as early as 1906 [13, 14]. The first test of an EP device on a spacecraft was an ion thruster on the NASA Space Electric Rocket Test 1 (SERT-1) in 1964. EP systems entered limited use beginning in 1972, in the form of Hall thrusters on Soviet Union “Meteor” satellites [15, 16]. Over the following twenty years, various forms of EP were used for satellite stationkeeping by the United States and the Soviet Union. Since the late 1990s, EP devices have also been used as the primary propulsion systems on several deep space missions, including the NASA Deep Space 1 technology demonstration mission [17], the Japanese Aerospace Exploration Agency (JAXA) Hayabusa asteroid sample return mission [18], and the European Space Agency (ESA) SMART-1 lunar mission [19].

2.1.1 Types of electric propulsion

Electric propulsion includes a wide variety of techniques for producing spacecraft thrust. The only common characteristic of EP systems is that the primary energy source is electrical power. That power source might include solar cells, radioisotope thermoelectric generators, nuclear reactors, or some combination of these. The defining characteristic of an EP system is not the particular power source, but rather the mechanism which converts the electrical energy into propulsive thrust. Generally an EP device can be grouped into one of three broad categories [20]: electrothermal, electrostatic, or electromagnetic.

The first category, electrothermal EP, uses electrical heaters or an electrical discharge to heat a working gas. That gas is then expanded through a nozzle as in a conventional rocket. The most common electrothermal devices include resistojets and arcjets. A schematic arcjet is shown in Fig. 2.1.

The second category, electrostatic EP, first ionizes the propellant and then accelerates the charged particles via electric fields between one or more extraction and acceleration grids. A schematic gridded ion thruster is shown in Fig. 2.2. Other electrostatic devices include Hall thrusters, field emission thrusters, and colloid thrusters. Devices in this category typically accelerate positive charge particles or ions, so there is a need for an electron-emitting neutralizer to prevent a net charge buildup on the spacecraft.

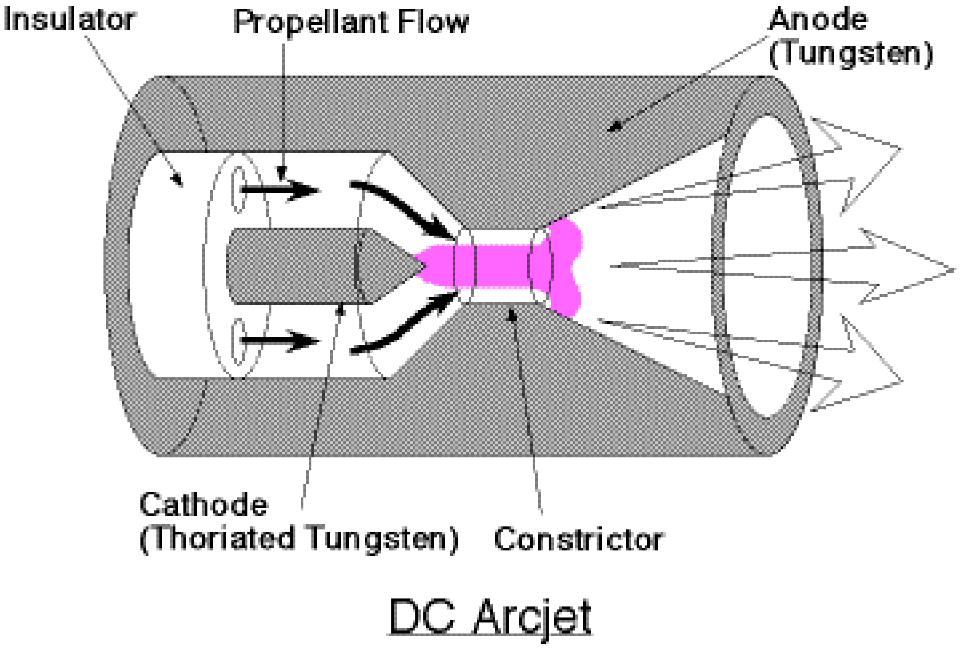

Figure 2.1: Schematic of an arcjet [21], demonstrating an electrothermal propellant acceleration mechanism.

The third category, electromagnetic EP, uses both electrical and magnetic fields to accelerate charged particles. Magnetoplasmadynamic (MPD) thrusters and pulsed plasma thrusters (PPTs) are the most common examples of this category. In PPT concepts, a strong current is driven through surface material to form an ablation plasma that carries the current from anode to cathode. Other concepts may use alternative ionization schemes, and require applied electric fields to drive the plasma. The plasma is accelerated to generate thrust via the Lorentz force of the magnetic fields acting on the plasma current. Figure 2.3 shows a schematic PPT.

2.1.2 Advantages and limitations

Electric propulsion offers several benefits over conventional chemical rockets, but also suffers from a few drawbacks. However, the gains in using an EP system can outweigh the losses for long-term or high-energy missions.

One of the biggest advantages of EP devices is the high exhaust velocity and

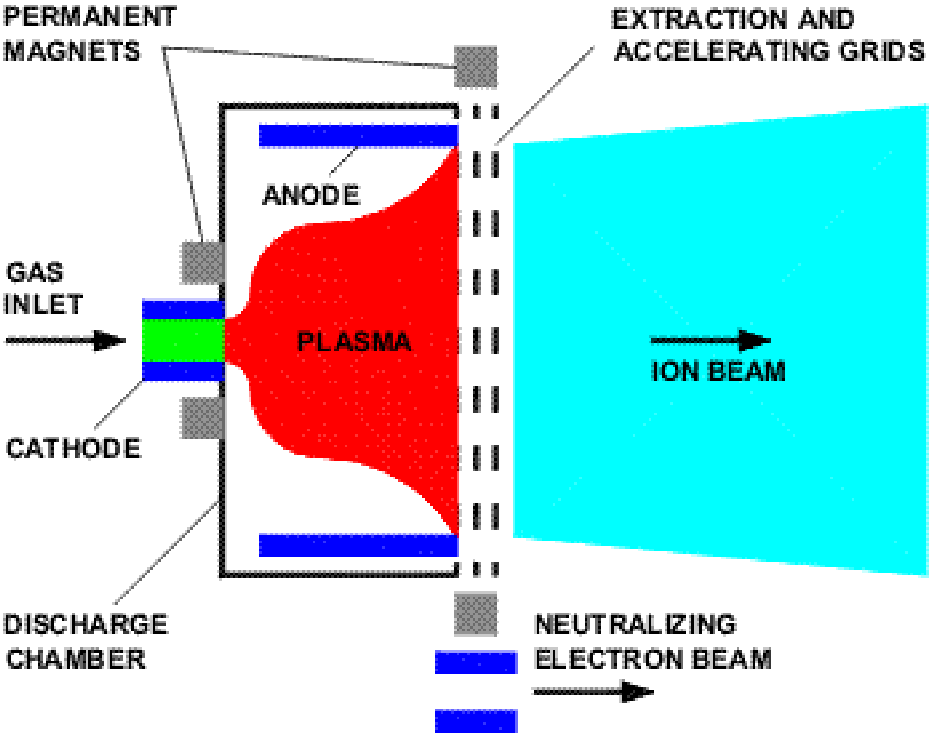

Figure 2.2: Schematic of an ion engine [22], demonstrating an electrostatic propellant acceleration mechanism.

corresponding high specific impulse. Specific impulse, or I_{sp}, is the ratio of thrust T, to propellant weight flow rate as in Eq. 2.1. The weight flow rate is simply the product of the mass flow rate $\dot{m}$ and standard gravity at the surface of the earth g.

$$I_{sp} = \frac{T}{\dot{m}g} \tag{2.1}$$

Various types of EP devices span a range of I_{sp}, from 500-2,000 s for arcjets, to 1,200-6,000 s for Hall thrusters, to 3,000-10,000 s for ion thrusters. For comparison, chemical rockets only range from 250-450 s I_{sp} [24].

The benefit of higher I_{sp} can be demonstrated from the ideal rocket equation, Eq. 2.2, which is derived from conservation of momentum for a system that is emitting mass [25]. For a system with initial total mass m_0 that undergoes a maneuver with a total change in velocity $\triangle v$, the final mass m after the maneuver is a function only

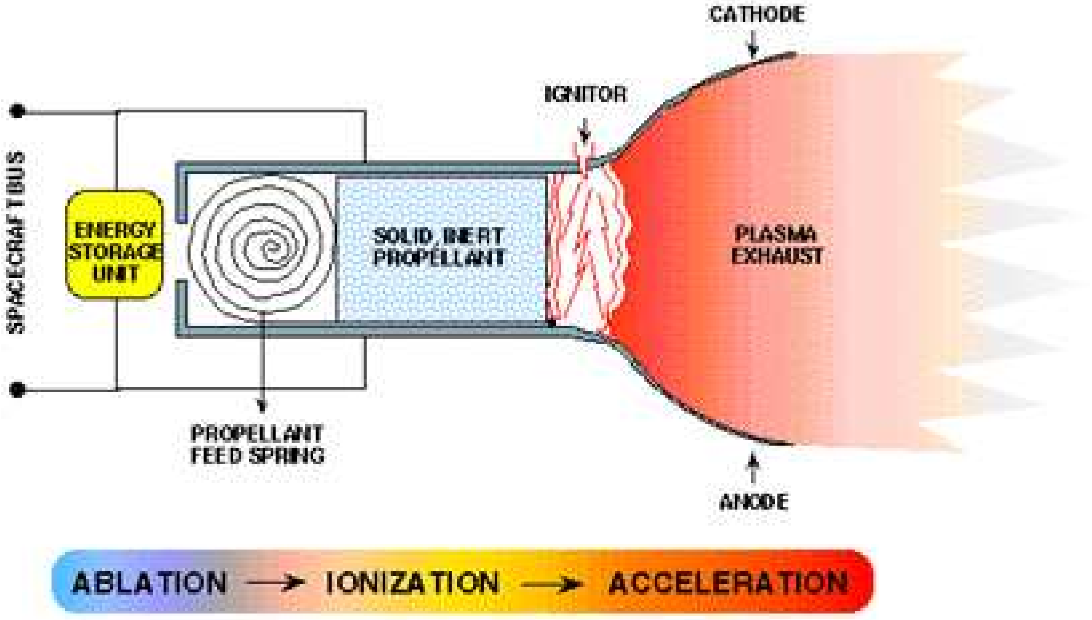

Figure 2.3: Schematic of a pulsed plasma thruster [23], demonstrating an electromagnetic propellant acceleration mechanism.

of the specific impulse I_{sp} and the gravitational constant g.

$$m = m_0 \exp\left(-\frac{\triangle v}{g I_{sp}}\right) \tag{2.2}$$

A spacecraft mission has a known, required $\triangle v$ from orbital mechanics and a limited m_0 based on the launch vehicle, so a higher specific impulse translates into more final payload mass after maneuvering. This can be put to use in several ways.

One option is to increase the payload mass, since an EP system requires less propellant mass than a chemical system for a given mission. Alternatively, the mission or operational lifetime could be extended, since the EP system can achieve a larger $\triangle v$ for a fixed propellant mass. Another route altogether is to eliminate the propellant mass saved by using the EP system and reduce the total mass, possibly allowing a less expensive launch vehicle to be used. These options can be combined to achieve a best compromise for a particular situation.

Another benefit of EP is the flexible control of the devices. Many EP systems are capable of semi-independent control of propellant flow and electrical systems, which allows for throttling of the flow rate, operating voltage, and current to optimize performance at a desired thrust level. This is an improvement over solid rockets, which have no throttle control, and over liquid or hybrid rockets, which can only throttle the flow rate. A mission using EP systems has less restrictive launch windows than a mission using conventional rockets.

Still another potential benefit of EP devices is the robustness of the underlying propulsive concept. Since the acceleration mechanism is not dependent on the particular propellant, an EP device could theoretically operate on a variety of different propellants. This could open the possibility of *in situ* propellant resupply for long-duration missions to comets or asteroids with volatile compounds. However, multiple-propellant thruster designs are beyond the current state of the art.

The two main drawbacks to using an EP device stem from the practical limit on the maximum current density that can be sustained in an electrical arc or plasma current. In electrothermal applications this acts to limit the rate of energy deposition, while in electrostatic and electromagnetic applications this acts to limit the flow rate of accelerated exhaust. In both cases the consequence is that EP systems produce much smaller thrust than chemical systems. For example, thrust levels from EP devices range typically range from a few μN for ion thrusters to less than 10 N for arcjets. In contrast, chemical rockets can achieve 1 kN-1 MN of thrust [24].

As a further negative consequence of low thrust production, EP systems require much longer firing time than chemical systems. While a chemical rocket typically operates for only a few minutes, an EP device must operate for months or years to achieve the full $\triangle v$ indicated from the ideal rocket equation. This introduces long-term performance issues as well as failure and lifetime concerns for EP systems.

Low levels of thrust are not necessarily prohibitive, and certain applications only require low thrust levels. Stationkeeping and orbit transfers are well within the range of thrust provided by EP devices, although orbit transfers will take significantly longer than with a chemical system. Microsatellite formation flight and high-precision stationkeeping maneuvers both benefit from engines that can produce small but highly repeatable thrust bits. One notable example is the planned NASA Laser Interferometer Space Antenna (LISA) mission [26], which requires μN-levels of thrust to maintain proper positioning of the component spacecraft.

2.2 Experimental investigation of electric propulsion

Research on EP devices is ongoing and includes activities at every stage of development: theory and design of novel concepts, testing and validation of designs, long-duration life tests of mature designs, and studies of spacecraft integration issues.

2.2.1 Ongoing Research

Mature technologies such as Hall thrusters and ion thrusters are well characterized in terms of performance. Research related to these systems is directed toward extending operational lifetime, characterizing the spacecraft integration issues, and developing high power configurations.

Since an EP device must operate for months or years, long-duration life tests are carried out in ground-based vacuum chambers. These tests often consider the issue from multiple viewpoints. From an application viewpoint, it is necessary to understand how the actual performance deviates from the ideal performance by measuring changes in thrust, beam divergence, and efficiency over the lifetime of the device [27, 28]. From a design viewpoint, characterization of the wear and damage sustained during prolonged operation is useful for identifying and addressing failure modes, as well as estimating the time to failure.

The exhaust plume from EP devices may include plasma, unaccelerated propellant, and materials eroded from the device. Different lines of research help characterize the resulting conditions near the spacecraft and consider how its performance is affected. Research into sputtering and deposition looks at the physical processes that erode material inside the thruster [29], and the transport and deposition of sputtered material and exhaust particles onto other spacecraft surfaces [30, 31]. Electromagnetic interference [31] is another concern, since charged particles in the exhaust plume can interfere with signal transmission to and from the spacecraft.

There is strong interest in developing high power EP systems that can produce higher thrust levels while maintaining favorable I_{sp} and efficiency. Research in this area is typically directed toward developing larger models of a device (the monolithic approach) [32] or toward developing clusters of existing smaller models of a device [33, 34, 35]. Challenges in a monolithic approach are related to fabrication and inadequate facilities for full-scale testing, while challenges for a clustering approach arise from operational difficulties due to the interaction between individual devices in a cluster.

There is also an active interest in developing novel EP concepts. New designs may incorporate the better elements of two systems, as in hybrid Hall/ion thrusters [36], or extend EP concepts to entirely new designs as in microthruster and MEMS "thruster on a chip" concepts [37, 38]. Hybrid designs are often able to move quickly to a prototype, since much of the fabrication and operation is well understood from existing designs. The more radical MEMS concepts are currently at proof of concept and early prototype stages. If the fabrication issues can be resolved, such concepts would offer even more flexible scalability and control than existing EP systems.

2.2.2 Vacuum facilities

Experimental testing is conducted in ground-based vacuum facilities. The largest academic facility in the United States is the Large Vacuum Test Facility (LVTF) at the Plasmadynamics and Electric Propulsion Lab (PEPL) at the University of Michigan [39]. The main chamber of the LVTF is a cylindrical vessel 9 m long, and 6 m in diameter. A diagram of the facility and several diagnostic instruments in Fig. 2.4 shows the complexity and scale involved. Smaller facilities are significantly less expensive to build, maintain, and operate, so chambers this large are rare.

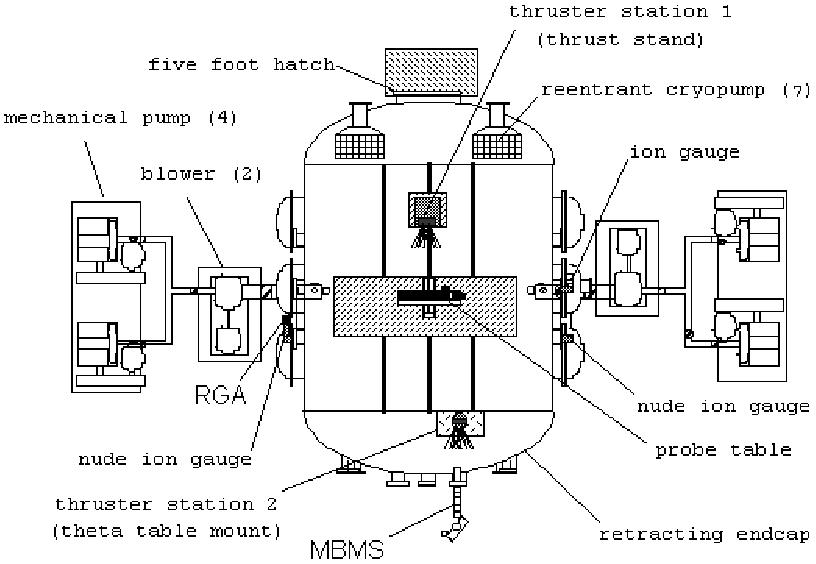

Figure 2.4: Large Vacuum Test Facility at the University of Michigan [39].

Although the LVTF has a very high pumping rate of 240,000 liters per second on xenon, the facility still develops a measurable back pressure during operation of EP thrusters [12]. This residual background pressure is due to the finite pumping capacity and inevitable leaks and outgassing present in any vacuum facility.

The interpretation of experimental measurements is complicated by secondary effects of the background gas. At the thruster itself, background gas can be re-ingested and accelerated, artificially increasing the thrust and propellant efficiency. Collisions between accelerated particles and background particles in the exhaust plume can increase beam divergence, broaden the energy distribution, and produce low energy charge exchange ions. This affects measurements of current density and velocity distribution throughout the plume.

2.2.3 Probe diagnostics

Experimental measurements of many plasma properties can be made using relatively simple plasma probe diagnostics [40]. Three mainstay probe instruments are discussed below: the Faraday probe, the Langmuir probe, and the retarding potential analyzer (RPA). These probes offer good spatial resolution and have well-established techniques for interpreting the measurements. Non-intrusive optical diagnostics are available, but are not as widely used due to the greater cost and complexity.

The nude Faraday probe is the simplest of probe devices, consisting of a current collecting surface that is large compared to the Debye length. One mode of operation is to apply a bias voltage to repel electrons, so that the probe measures only the ion current at a point in the plasma flow. Alternatively, the probe bias can be allowed to float to the plasma potential, so that the net current to the probe is zero. More complicated variations of the Faraday probe incorporate physical or electromagnetic filtering [41, 42] to screen out the electron current or undesired, random ion currents.

The Langmuir probe consists of one or more current collecting wires that are immersed in the plasma. Several configurations are commonly used, including single, double, and triple probes [43, 44, 45]. These variations allow for simplifications in the control system or in the analysis of measurements. Measurements from the current versus voltage characteristic of a Langmuir probe can be used to determine the plasma potential, the floating potential, the electron temperature, and the plasma number density.

The RPA is somewhat more complicated than the previous probes, since it uses a series of biased screens to repel particles below a threshold energy while allowing higher energy particles to reach a collecting surface [40, 46]. By analyzing the derivative of collected current over a range of bias voltage, it is possible to extract the energy distribution function of the ions.

Each of these probe diagnostics is immersed in the plasma flow and causes some disturbance relative to the unimpeded flow if the probe were not present. Recent experimental measurements of the plasma properties around an immersed Faraday probe show that the disturbed flow field around the probe can be observed [12]. In the diagnostic techniques, these disturbances are assumed to be relatively small and confined to a sheath and presheath region around the probe.

2.3 Computational modeling of electric propulsion

Computational research parallels many of the experimental investigations described previously. Experimental and computational investigations are often complementary, although some discrepancies persist between experimental measurements and computational results.

2.3.1 Computational techniques

Several types of EP devices including Hall thrusters, ion thrusters, PPTs, and MPDs generate strongly flowing, low density plasma exhaust plumes. Models of plasma behavior must describe particle motion, along with the self-consistent electric and magnetic fields that govern the motion. Computational models must therefore be capable of solving the equations of motion for particles and the differential equations for electromagnetic fields.

One of the earliest and most widely used computational techniques for simulating plasmas is the Particle In Cell or PIC method [47]. In this type of model the plasma is represented by a reduced number of macroparticles that obey the standard equations of motion and interact with discrete electric fields calculated on a computational grid. In brief, this method separates the particle motion from the calculation of fields and iterates to achieve a consistent solution.

A related technique is Direct Simulation Monte Carlo or DSMC, which also uses macroparticles to simulate gases and incorporates probabilistic models to describe particle collisions [48]. This allows additional physical processes to be considered, including chemistry, ionization and recombination, and surface interactions. DSMC models can be combined with PIC models to add collisions and wall interactions to a plasma simulation. In Chapter V both PIC and DSMC techniques will be described in greater detail for the particular implementation used in this research.

Under conditions where magnetic fields dominate particle motion, an alternative set of models is available. Magnetohydrodynamic (MHD) equations describe a magnetized plasma in the continuum limit, similar to the Navier-Stokes equations as solved in computational fluid dynamics (CFD) models. In non-equilibrium limits, a gyro-kinetic model is necessary to describe particle motion. This model is roughly analogous to the PIC model, but requires an average over the fast gyromotion of magnetically confined particles. Magnetic fields are not significant in the far field of a Hall thruster or ion thruster, so MHD and gyrokinetic models will not be discussed in this dissertation.

2.3.2 Ongoing research

Computational research in EP overlaps experimental investigations in almost every area. Lifetime issues are addressed by investigating sputtering and erosion processes in the thruster [49, 50]. Integration issues are considered through studies of deposition and implantation [51], plume backflow [52], and through plasma control to mitigate signal interference [53]. High-power cluster configurations are simulated to evaluate the performance, with near- and far- field studies to characterize the exhaust plume [54]. Preliminary modeling is already underway to characterize prototype MEMS devices [55].

A broader goal is to develop and refine computational models until they become sufficiently accurate to perform reliable assessment and characterization of EP devices. Meeting that goal would help streamline the design process for new devices and also enable more effective interpretation of experimental results. For example, a sufficiently robust computational model could be used to predict on-orbit performance of a high-power configuration from measurements made in small vacuum chambers where the pumping rate is too low.

At this point there are few or no efforts to comprehensively improve model fidelity. However, narrowly focused efforts to improve specific aspects of a model are often incidental to a computational study. Variations of existing models are implemented to more accurately capture the physics involved in some aspect of a broader study. For a few examples: a wall sputtering model might be added to a thruster simulation in order to compare the calculated performance degradation with experimental results from a long-duration life test [56], or higher fidelity magnetic fields might be incorporated in a Hall thruster acceleration model to assess the impact on the near-field plume [57]. Additionally, many lines of research are directed toward speeding up existing models, either by using alternative techniques to perform similar calculations or by optimization and parallelization of an existing computational code.

2.4 Need for simulation of plasma probes

Experimental and computational researchers continually share results in EP, so it is desirable to have a clear understanding of how experimental measurements relate to undisturbed plasma conditions.

Electric propulsion devices produce highly non-equilibrium plasma flows. The most commonly used electromagnetic and electrostatic devices produce an exhaust plume consisting of high temperature electrons, high energy ions of various charge states formed in the thruster, high energy neutrals and low energy ions formed via charge exchange collisions, and low energy neutrals that diffuse out of the thruster without being ionized or accelerated. The plasma is low density, strongly flowing, and nearly collisionless as a whole.

This is markedly more complicated than the simple conditions of isothermal electrons and cold drifting ions assumed in the theoretical analysis of some plasma probe measurement techniques. One important open question is how well the theoretical probe techniques perform for a more complex, realistic EP plasma flow. A computational setting is especially well suited to evaluating this question, since the plasma conditions can be specified explicitly and probe measurements can be simulated and analyzed according to standard diagnostic techniques. By moving incrementally from the ideal plasma of the diagnostic theory to a realistic plasma, it is also possible to isolate the effects of each deviation from the ideal assumptions.

A second open question is how the insertion of a diagnostic probe disturbs the plasma flow, and whether that disturbance introduces a systematic error in the measurements the probe makes. Put another way, it is not clear whether the disturbed conditions measured by the probe can be related back to the undisturbed plasma conditions. Again, a computational setting is ideal for investigating these effects since the undisturbed conditions are known explicitly as inputs.

The remainder of this dissertation describes the development and use of computational models to help address these open questions.

Chapter III

Governing Equations and Analytical Sheath Models

The flow field around a Faraday probe is characterized by plasma interactions with physical surfaces and electrostatic sheaths. Since this involves numerous physical mechanisms and spans a broad range of scales, it is useful to first consider simplified conditions that can be solved analytically. This chapter introduces the classical descriptions of a plasma and the derivation and use of two analytical models. Later chapters will refer to these analytical models as reference cases.

The first model is described as a shadowing model, alluding to physical obstruction of the flow by the probe body. The flow structures described in this model are on a scale comparable to the probe dimensions. Although the model is developed from a very general kinetic description of the plasma, the analytical solution is limited by the assumption of negligible electric and magnetic fields. Due to that limitation, the shadowing model is only a gasdynamic model and will not capture the more complicated plasmadynamic effects.

The second model is a collisionless planar sheath model. In this model the flow structures are on a scale comparable to the Debye length, which is generally much smaller than the probe dimensions. This model is developed from a fluid description of the ion plasma, and accounts for coupling between the electric fields and the plasma by solving the electrostatic Poisson equation. This model is a plasmadynamic model, and includes most of the relevant physical processes that occur in a sheath.

3.1 Plasma concepts and theories

Plasmas behave like gases in many regards, but the addition of free charged particles makes a plasma electrically conductive. At microscopic scales approaching and smaller than the Debye length, electrostatic forces between particles are significant. However, these inter-particle forces act to redistribute the charge in such a way that local charge is shielded and the plasma appears uniform over larger scales [58]. At the macroscopic scale, the bulk plasma exhibits collective behavior that is consistent with zero internal electric or magnetic fields.

The charge shielding effect is not uniform near the edges of a plasma, for instance at a free surface interface with vacuum or at a conducting wall. External electric and magnetic fields influence charged particles near the edge of the plasma and generate a sheath [1, 2], which in turn acts to isolate the bulk plasma from the external fields. The sheath thickness is determined by the distance that external fields can penetrate into the plasma, and depends on the density and mobility of the charged particles. Like the charge shielding effect, sheath thickness scales with Debye length.

3.1.1 Kinetic description

A plasma is an ionized gas, so a theory that describes gas behavior is a reasonable starting point for describing a plasma. The kinetic theory of gases is a very successful theory based on a statistical description of a gas at the molecular level. Appropriate averages of microscopic properties such as velocity and collision rate can be related to the macroscopic temperature and pressure.

Kinetic theory posits that a gas is composed of a very large number of particles that interact only through collisions [59, 60, 61]. In the simplest form, the particles are assumed to be identical and devoid of internal structure so that a particle can be described completely by its position and velocity. A particle's position and velocity at any later time can be found by integrating the equations of motion. The bulk gas can then be described by a time-varying distribution function $f(\mathbf{x}, \mathbf{v}, t)$ of all the constituent particles over a phase space with three dimensions in both space and velocity. Since the initial positions and velocities of the particles are essentially random, the distribution function is evaluated statistically.

Behavior of the gas then corresponds to evolution of the distribution function. The Boltzmann transport equation, Eq. 3.1, describes how the distribution function changes in space and time. Particles are advected in space due to their velocity $\left(\mathbf{v}\frac{\partial f}{\partial \mathbf{x}}\right)$, and accelerated in velocity space by any external forces $\left(\mathbf{a}\frac{\partial f}{\partial \mathbf{v}}\right)$. The collision operator $C\left(\mathbf{v}_1, \mathbf{v}_2\right)$ is a function that relates the initial and final velocities for colliding particles. In a dilute gas the particle size is much smaller than the average spacing between particles, and binary collisions dominate the collision operator.

$$\frac{\partial f}{\partial t} + \mathbf{v} \cdot \frac{\partial f}{\partial \mathbf{x}} + \mathbf{a} \cdot \frac{\partial f}{\partial \mathbf{v}} = C\left(\mathbf{v}_1, \mathbf{v}_2\right) \tag{3.1}$$

Macroscopic properties of the gas are then obtained by taking moments of the distribution function as in Eq. 3.2. The zeroth and first moments respectively produce the density and mean velocity, and the second central moment yields temperature.

$$\begin{aligned} n\left(\mathbf{x}\right) &= \int_{-\infty}^{\infty} n_{\infty} f(\mathbf{x}, \mathbf{v}) d\mathbf{v} \\ \left\langle \mathbf{v}\left(\mathbf{x}\right) \right\rangle &= \frac{1}{n\left(x\right)} \int_{-\infty}^{\infty} n_{\infty} \mathbf{v} f(\mathbf{x}, \mathbf{v}) d\mathbf{v} \\ T\left(\mathbf{x}\right) &= \frac{1}{n\left(x\right)} \int_{-\infty}^{\infty} n_{\infty} (\mathbf{v} - \left\langle \mathbf{v}\left(\mathbf{x}\right) \right\rangle)^2 f(\mathbf{x}, \mathbf{v}) d\mathbf{v} \end{aligned} \tag{3.2}$$

A solution to Eq. 3.1 can be found for an unbounded gas at equilibrium, with no external forces. It can be shown that the collision term must be zero at equilibrium, corresponding to a detailed balance for the distribution. The energy partition function for the particles in the gas can be analyzed with statistical mechanics, leading to the functional form of the distribution. The remaining parameters of the distribution function can then be determined by comparing the kinetic moments of Eq. 3.2 with classical thermodynamic forms for entropy [61]. The resulting Maxwell-Boltzmann or "Maxwellian" distribution given in Eq. 3.3 describes a gas that is spatially uniform and does not vary in time. The more complicated space and time varying distributions required to describe practical flows are often intractable by analytic methods, and solutions must be obtained numerically.

$$f\left(\mathbf{v}\right)d\mathbf{v} = \left(\frac{m}{2\pi k_B T}\right)^{\frac{3}{2}} \exp\left[-\frac{m}{2k_B T}\left(v_x^2 + v_y^2 + v_z^2\right)\right] d\mathbf{v} \tag{3.3}$$

The kinetic description for a plasma is more complicated than for a gas. Most plasmas are partially ionized, meaning that the bulk plasma consists of neutral gas particles, ions, and electrons. Separate but coupled distribution functions are required for each species in order to completely describe the plasma.

The Lorentz force, as given in Eq. 3.4, describes the electric and magnetic forces that act on the charged particles.

$$\mathbf{a}_{EM} = \frac{e}{m}\left(\mathbf{E} + \mathbf{v} \times \mathbf{B}\right) \tag{3.4}$$

At the microscopic level, strong electromagnetic fields can drive collective drifts or confine particle motion to orbits about magnetic field lines. At the macroscopic level, several kinds of plasma waves arise due to the coupling between electric and magnetic fields as described in Maxwell's laws [62].

In a plasma, collisions can also alter the species of the particles: charged particles can be formed in ionization collisions, lost in recombination collisions, or transferred in charge exchange collisions. A separate collision operator can be defined for each of these processes, including a collision operator between particles of a single species $C\left(\mathbf{v}_1, \mathbf{v}_2\right)$, a momentum exchange operator between different species $C_M\left(f_1, f_2\right)$, a charge exchange operator between different species $C_C\left(f_1, f_2\right)$ that can act as source or sink, an ionization source $S_I\left(f_1, f_2\right)$, and a recombination sink $S_R\left(f_1, f_2\right)$. For brevity, Eq. 3.5 defines a total collision operator C_{Tot} that includes each of these components.

$$C_{Tot} = C\left(\mathbf{v}_1, \mathbf{v}_2\right) + C_M\left(f_1, f_2\right) + C_C\left(f_1, f_2\right) + S_I\left(f_1, f_2\right) - S_R\left(f_1, f_2\right) \tag{3.5}$$

The modified Boltzmann transport equation for the distribution function f_j of one plasma species seen in Eq. 3.6 appears very similar to the earlier form for a gas [58]. All of the complications associated with a plasma have been grouped into more complicated acceleration and collision terms. A full solution for the plasma would require simultaneous solution of an equivalent expression for each ion, electron, and neutral species, which is considerably more difficult than for a single neutral gas species.

$$\frac{\partial f_j}{\partial t} + \mathbf{v} \cdot \frac{\partial f_j}{\partial \mathbf{x}} + \left(\mathbf{a} + \mathbf{a}_{EM}\right) \cdot \frac{\partial f_j}{\partial \mathbf{v}} = C_{Tot} \tag{3.6}$$

More advanced versions of kinetic theory can be devised to incorporate elastic collisions, chemical reactions, and vibrational and rotational modes for molecules [61]. However, analytical solutions are only possible for very simple conditions, and numerical approaches must generally be used instead.

3.1.2 Fluid description

A macroscopic treatment of the flow through a control volume leads to conservation laws for mass, momentum, and energy. Together with a state equation, the conservation equations accurately describe the continuum behavior of a gas. This is not surprising since the conservation laws can be obtained from kinetic theory in the limits of continuum or equilibrium flow [59]. The degree of non-equilibrium in a flow is characterized by the Knudsen number in Eq. 3.7 as the ratio of mean free path between collisions λ_{MFP} to the relevant reference length of interest L. The fluid equations are appropriate when the Knudsen number is small, typically $\mathrm{Kn} < 0.01$, and the flow is near equilibrium.

$$\mathrm{Kn} = \frac{\lambda_{MFP}}{L} \tag{3.7}$$

Starting from the kinetic model of a gas with an assumed Maxwellian distribution (Eq. 3.3), the zeroth, first, and second moments of the Boltzmann transport equation (Eq. 3.1) correspond to conservation of mass, momentum, and energy. A practical difficulty in this approach is that any moment of the transport equation involves contributions from the next higher moment. This closure problem is resolved by enacting a moment closure, where higher order moments are expressed in terms of lower order moments. In practice, a Chapman-Enskog expansion of the equilibrium function is taken to third order terms, and the fourth moment of the expanded distribution then depends only on the lower moments.

Taking the moments of the Maxwellian distribution produces the Euler equations for inviscid fluid flow (Eq. 3.8). One significant limiting factor in the use of the Euler equations is that no gradient transport is possible. Physical phenomena such as heat transfer and momentum transfer at a wall cannot be described.

$$\begin{aligned}
\frac{\partial \rho}{\partial t} + \nabla \cdot (\rho \mathbf{v}) &= 0 \\
\frac{\partial (\rho \mathbf{v})}{\partial t} + \nabla \cdot (\rho \mathbf{v}\mathbf{v}) + \rho \mathbf{a} &= -\nabla P \\
\frac{\partial (\rho e)}{\partial t} + \nabla \cdot (\rho e \mathbf{v}) + \rho \mathbf{a} \cdot \mathbf{v} &= -P \nabla \cdot \mathbf{v}
\end{aligned} \tag{3.8}$$

The well known Navier-Stokes equations in Eq. 3.9 can be obtained in a similar fashion by starting with a first order Chapman-Enskog perturbation of the Maxwellian distribution [59]. Again, moments of the Boltzmann transport equation produce the conservation laws for mass, momentum, and energy.

$$\begin{aligned}
\frac{\partial \rho}{\partial t} + \nabla \cdot (\rho \mathbf{v}) &= 0 \\
\frac{\partial (\rho \mathbf{v})}{\partial t} + \nabla \cdot (\rho \mathbf{v}\mathbf{v}) + \rho \mathbf{a} &= -\nabla P + \nabla \cdot \boldsymbol{\tau} \\
\frac{\partial (\rho e)}{\partial t} + \nabla \cdot (\rho e \mathbf{v}) + \rho \mathbf{a} \cdot \mathbf{v} &= -P \nabla \cdot \mathbf{v} + \boldsymbol{\tau} : \boldsymbol{\epsilon} - \nabla \cdot \mathbf{q}
\end{aligned} \tag{3.9}$$

The Navier-Stokes equations include gradient transport. Momentum transport occurs via shear stress and energy transport occurs via heat flux. However, the deviatoric shear stress tensor $\boldsymbol{\tau}$ and heat flux vector $\mathbf{q}$ introduce a closure problem since neither is explicitly a function of the independent thermodynamic variables. Typically the equation set is closed by assuming constitutive relations, such as Newtonian fluid viscosity to replace the stress tensor and Fourier heat conduction to replace the heat flux vector. The constitutive relations may introduce additional transport coefficients such as viscosity and thermal conductivity that must be determined as well.

Higher order perturbations of the Maxwellian distribution have been considered [59], leading to the Burnett equations. Such models suffer from the same sort of closure problems as the Navier-Stokes equations, and produce significantly more complicated forms of the stress tensor and heat flux. Higher-order models are correspondingly more difficult to solve, and the Burnett equations in particular are unstable without higher-order corrections.

Equivalent conservation laws can be developed for a plasma by including electromagnetic force contributions to momentum and energy [58]. Additionally, Maxwell's laws are used to determine consistent electromagnetic fields. Typically the effects of viscous forces are negligible compared to electromagnetic forces, so contributions from the shear stress tensor are omitted here. Collisional resistance to electrical current affects momentum transport in the flow, giving rise to the resistive term $\sim \frac{\mathbf{j}}{\sigma}$ and the electrical conductivity σ. The equation set in Eq. 3.10 is the basis of the magnetohydrodynamic (MHD) equations for a plasma.

$$\begin{gathered}
\frac{\partial \rho}{\partial t} + \nabla \cdot (\rho \mathbf{v}) = 0 \\
\frac{\partial (\rho \mathbf{v})}{\partial t} + \nabla \cdot (\rho \mathbf{v}\mathbf{v}) + \rho \mathbf{a} + \rho \frac{e}{m} (\mathbf{E} + \mathbf{v} \times \mathbf{B}) = -\nabla P + \rho \frac{e}{m} \frac{\mathbf{j}}{\sigma} \\
\frac{\partial (\rho e)}{\partial t} + \nabla \cdot (\rho e \mathbf{v}) + \rho \mathbf{a} \cdot \mathbf{v} + \rho \frac{e}{m} \mathbf{E} \cdot \mathbf{v} = -P \nabla \cdot \mathbf{v} - \nabla \cdot \mathbf{q} \\
\nabla \cdot \mathbf{B} = 0 \\
\nabla \cdot \mathbf{E} = \frac{e}{\varepsilon_0} (n_i - n_e) \\
\nabla \times \mathbf{E} = -\frac{\partial \mathbf{B}}{\partial t} \\
\nabla \times \mathbf{B} = \mu_0 \mathbf{j} + \varepsilon_0 \mu_0 \frac{\partial \mathbf{E}}{\partial t}
\end{gathered} \tag{3.10}$$

A number of analytic solutions to the MHD equations can be found after taking appropriate limits and substantially rearranging these equations. Such solutions describe many plasma waves, including magnetosonic waves and Alfven waves [63]. However, many practical situations are too complex for analytic solutions, and numerical solutions must be found instead.

3.2 Geometric Shadowing Model

The central premise of the shadowing model is that certain particle trajectories are blocked or shadowed in the vicinity of a physical obstruction. This shadowing causes the distribution function to differ from the distribution at points far from the obstruction. Since the macroscopic plasma properties are calculated as moments of the distribution, plasma at a shadowed point has different properties than unaffected plasma far from the surface.

The model described here was originally developed in the context of strongly flowing, magnetically confined, tokamak fusion plasmas [5, 64, 65]. The derivation given here closely follows the approach described by Valsaque *et al.* [66]. One minor variation from that approach is to normalize the equations with length and velocity scales that are consistent with other models considered in this dissertation.

3.2.1 The Vlasov equation and shadowing solution

In the shadowing model, the inflowing plasma is fully ionized, neutral, and consists of electrons and an arbitrary distribution of ions. The ions are analyzed with a kinetic model derived from the Boltzmann transport equation. A steady, collisionless, planar sheath is assumed by taking the steady state $\left(\frac{\partial f}{\partial t} = 0\right)$ and collisionless $(C = 0)$ limits in Eq. 3.1 and reducing the flow to one dimension. The resulting form in Eq. 3.11 is often referred to as the Vlasov equation. Note that the distribution function reduces to $f\left(x, v_x\right)$ under these simplifications.

$$v_x \frac{\partial f}{\partial x} + a_x \frac{\partial f}{\partial v_x} = 0 \tag{3.11}$$

The acceleration in this case simplifies to the contributions from the electric field along the direction of flow, as in Eq. 3.12. Since the flow is one dimensional, there is no possible magnetic field orientation that would generate a magnetic force contribution along the direction of flow. The electric field is also rewritten in terms of the electric potential for convenience.

$$a_x = \frac{e}{m_i} E_x = -\frac{e}{m_i} \frac{d\phi}{dx} \tag{3.12}$$

The diffusive source term in Eq. 3.13 is added to represent a random transfer of particles between the shadowed region in the sheath and the ambient plasma [66]. The ambient plasma has a freestream distribution function $f_\infty(v_x)$, which should be recovered from $f(x, v_x)$ in the limit as $x \rightarrow -\infty$. A simple exchange frequency parameter w is defined that assumes a uniform diffusion rate of particles into and out of the sheath, regardless of location or particle velocity.

$$S_{Diffusion} = w\left(f_\infty(v_x) - f(x, v_x)\right) \tag{3.13}$$

The schematic diagram in Fig. 3.1 shows the coordinates of the shadowing sheath model and representative forms of the distribution function at a few points in the sheath. The surface of the probe is located at $x = 0$, and the plasma is confined to negative values of x upstream of the probe. The velocity is defined such that positive v_x corresponds to forward flow, toward the probe surface, and negative v_x corresponds to backward flow, away from the probe surface. The ambient plasma distribution is $f_\infty(v_x)$ and remains unchanged at all points in the sheath. The local distribution function in the sheath is $f(x, v_x)$, and far from the probe the local distribution approaches the ambient distribution, $f(x \longrightarrow -\infty, v_x) = f_\infty(v_x)$. At the surface of the probe, the distribution function for backward flowing velocities is identically zero, $f(0, v_x) = 0$ for $v_x < 0$. The exchange frequency w is constant throughout the sheath, and determines the rate that particles diffuse between the ambient and local distributions.

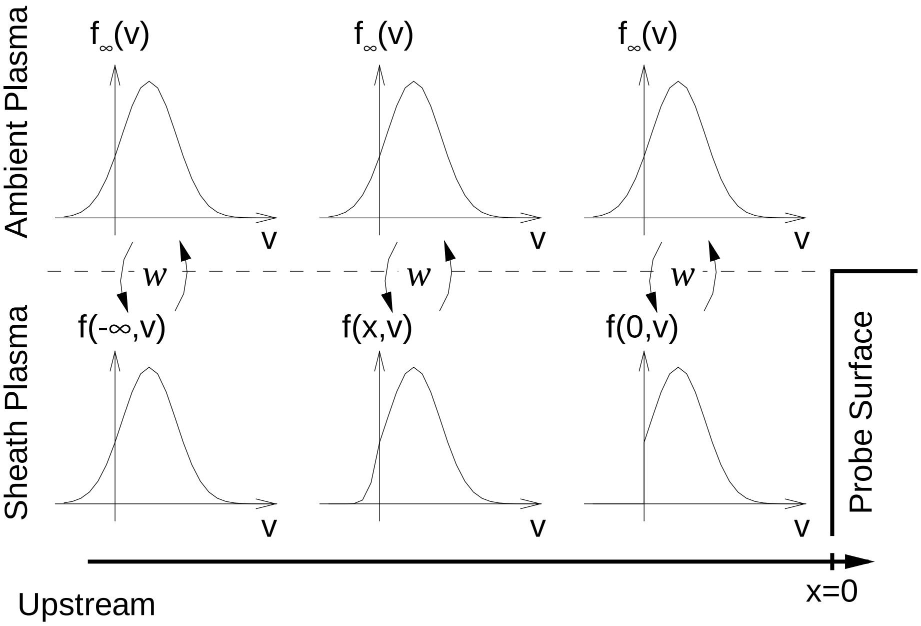

Figure 3.1: Schematic of the geometric shadowing model, showing the regions of the flow and the distribution function.

Combining Eqs. 3.11-3.13 gives a differential equation for the distribution function throughout the sheath as in Eq. 3.14. That expression is only a model of the ion plasma. To model the neutral plasma, a similar expression for the electron plasma would be required and the electrostatic Poisson equation would close the set.

$$v_x \frac{\partial f}{\partial x} - \frac{e}{m_i}\frac{d\phi}{dx}\frac{\partial f}{\partial v_x} = w\left(f_\infty\left(v_x\right) - f\left(x, v_x\right)\right) \tag{3.14}$$

Using the standard plasma parameters of Debye length, λ_D, and plasma frequency, ω_P, as given in Eq. 3.15, this equation can be recast in the normalized variables of Eq. 3.16. The normalized velocity is represented as a Mach number M with respect to Bohm velocity, v_B, and the normalized temperature τ is the ratio of ion to electron temperature. This choice of normalizations is consistent with the planar Bohm sheath model that will follow in Sec. 3.3.

$$\lambda_D = \sqrt{\frac{\varepsilon_0 k_B T_e}{e^2 n_e}},\ \omega_P = \sqrt{\frac{e^2 n_e}{\varepsilon_0 m_e}},\ v_B = \lambda_D \omega_P = \sqrt{\frac{k_B T_e}{m_e}} \tag{3.15}$$

$$z = \frac{x}{\lambda_D},\ W = \frac{w}{\omega_P},\ \Phi = \frac{e\phi}{k_B T_e},\ n_i^{'} = \frac{n_i\left(z\right)}{n_{i,\infty}},\ M = \frac{v_x}{v_B},\ \tau = \frac{T_i}{T_e} \tag{3.16}$$

After normalizing and rearranging, the differential equation for $f\left(z, M\right)$ is:

$$M\frac{\partial f}{\partial z} - \frac{d\Phi}{dz}\frac{\partial f}{\partial M} = W\left(f_\infty - f\right) \tag{3.17}$$

In order to obtain an analytic solution it is necessary to assume negligible electric fields $\left(\frac{d\Phi}{dz} = 0\right)$, which produces the form in Eq. 3.18. The boundary conditions in Eq. 3.19 require the distribution function to approach the ambient distribution far from the probe surface, to have no backward flow at the probe surface.

$$M\frac{\partial f}{\partial z} = W\left(f_\infty - f\right) \tag{3.18}$$

$$f\left(z \to \infty, M\right) = f_\infty\left(M\right),\ f\left(0, M\right) = \begin{cases} 0, & M \leq 0 \\ \\ f_\infty\left(M\right), & M > 0 \end{cases} \tag{3.19}$$

This can then be solved as a non-homogeneous partial differential equation, and the solution takes the form shown in Eq. 3.20. Moments of the modified velocity distribution function can then be taken as defined in Eq. 3.2 to obtain the local density, mean velocity, and temperature.

$$f\left(z, M\right) = f_\infty\left(M\right)\left[1 - \mathrm{H}\left(-M\right)\exp\left(-\frac{W}{M}z\right)\right] \tag{3.20}$$

The Heaviside function $\mathrm{H}\left(-M\right)$ activates an exponential fall off in density for backward flowing particles ($M < 0$) as the flow approaches the surface. This aspect describes a shadowing effect where the backward flowing particles are not present at the surface, but diffuse into the sheath upstream of the surface. Forward flowing particles ($M > 0$) maintain the ambient density at all points in the sheath.

This solution can also be easily modified to consider the sheath on a backward facing surface by changing the boundary conditions. In particular, the inequality in the second condition in Eq. 3.19 must be reversed. The solution retains the same form except that the sign of the Mach number argument is switched in the Heaviside function.

A few immediate observations can be made about this model. First, since the analytic solution neglects any electric and magnetic fields, this is only a gasdynamic model and cannot capture all of the behavior expected for charged particles in an electrostatic sheath. Second, the functional form of the ambient distribution function is not important in this solution, so it is applicable to any inflow condition. However, the nature of the ambient distribution is carried throughout the sheath. Third, this model cannot be translated to physical dimensions unless the normalized exchange frequency W is found.

3.2.2 Results and Discussion

The geometric shadowing model solves for the local ion distribution function in the sheath based on an arbitrary freestream distribution function. In order to facilitate comparison with the planar Bohm sheath model, the inflow distribution is assumed to be a Maxwellian. It is trivial to normalize one velocity component of the Maxwellian distribution function from Eq. 3.3 to the form seen in Eq. 3.21, with the two parameters of drift Mach number $M_D = \frac{v_D}{v_B}$ and freestream ion to electron temperature ratio $\tau_\infty = \frac{T_{i\infty}}{T_e}$.

$$f_\infty(M)\, dM = \frac{1}{\sqrt{2\pi\tau_\infty}} \exp\left(-\frac{(M - M_D)^2}{2\tau_\infty}\right) dM \tag{3.21}$$

The direct result of the analytic solution is a modified distribution function calculated from Eq. 3.20. Examples of the distribution function at several positions in the sheath are shown in Fig. 3.2. The freestream plasma conditions and parameter values for this example are: equal ion and electron temperatures, $\tau = 1$; ion

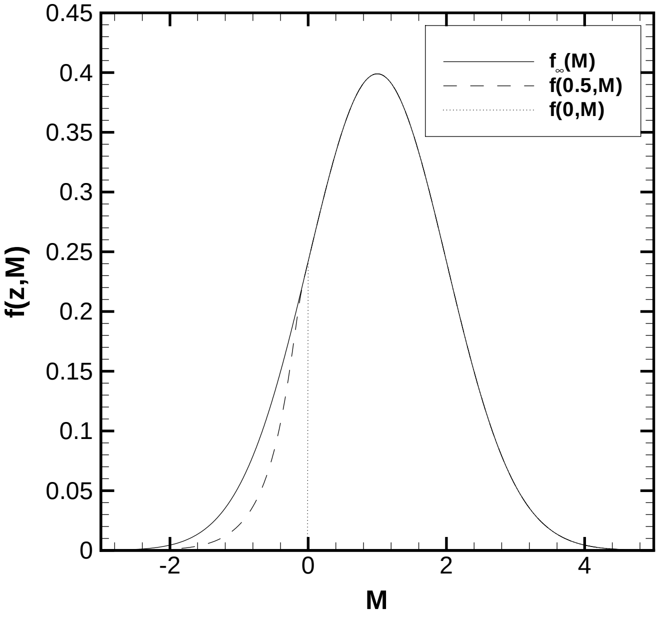

Figure 3.2: Profiles of the local distribution function in the shadowing sheath solution.

drift velocity equal to the Bohm velocity, $M_D = 1$; and exchange frequency equal to the plasma frequency, $W = 1$. Changing the parameters of the ambient distribution function has the usual effect, with larger M_D shifting the entire distribution to higher velocities and larger τ_∞ acting to broaden the distribution.

The effect of changing the exchange parameter W is to scale the rate of exponential falloff for the shadowed velocity range. A more meaningful alternative interpretation is that changing W scales the physical length of the shadowing sheath. As a practical note, the plasma frequency is the fastest time scale for the electrons. The rate of ion transfer presumably occurs on a slower time scale, so the normalized exchange frequency is expected to be small ($W \ll 1$) for a physically realistic plasma.

Far from the probe surface ($z \to -\infty$) the distribution approaches the Maxwellian of Eq. 3.21. For intermediate values of z, the distribution has an exponentially scaled probability for velocities less than zero, and retains the ambient distribution

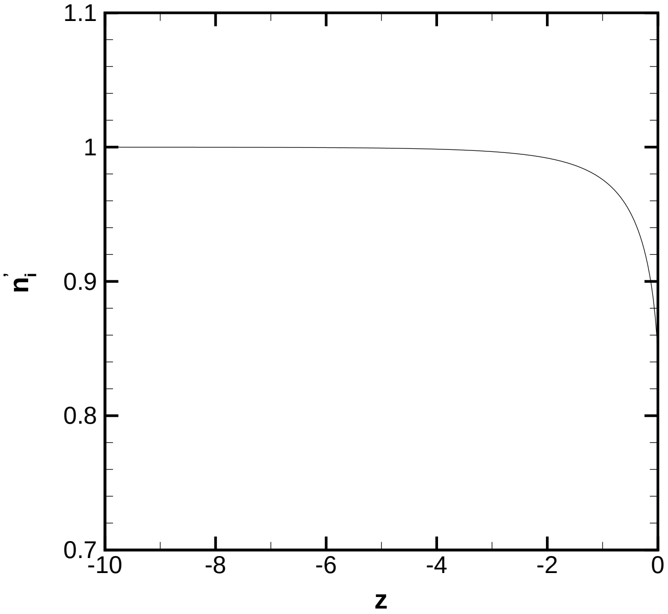

Figure 3.3: Profile of ion number density in the shadowing sheath solution.

for velocities greater than zero. At the surface ($z = 0$) the modified distribution is a truncated Maxwellian, with identically zero probability for all backward flowing velocities. The local distribution function is continuous at all $z < 0$, but has a discontinuity at $z = 0$.

The thermodynamic properties of the local plasma are computed by taking the moments of the modified distribution at each position in the sheath. Since the modified distribution function is not an elementary function, the moments are obtained through numerical integration. The first moment of the distribution yields the local ion density profile in Fig. 3.3 and the second moment yields the mean velocity profile in Fig. 3.4. Each point on these profiles corresponds to an integral over the modified distribution function at that position in the sheath.

Number density drops as the flow approaches the surface, since the backward flowing part of the distribution is shadowed out. Since only particles with negative

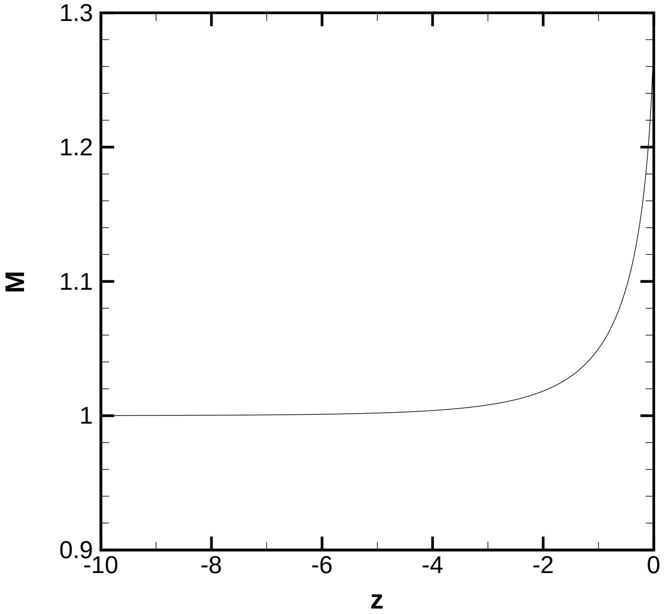

Figure 3.4: Profile of ion mean velocity in the shadowing sheath solution.

velocities are shadowed out, the mean velocity increases near the probe surface. This reflects the decrease in number of particles with negative velocity, but does not indicate any acceleration of the flow. Ion flux is not conserved through the sheath, since the diffusion process represented by the exchange frequency acts to transfer flux between the sheath and the ambient plasma.

The local ion temperature profile can be computed from the second central moment of the local distribution, as in Fig. 3.5. The temperature shows a gradual decrease as the flow approaches the surface, since the distribution tends toward a smaller spread about a higher mean velocity. The low velocity tail becomes less significant in the temperature calculation as the probability of the shadowed velocities decreases near the probe surface.

The electron properties and plasma potential are not solved in this model. In fact, the potential must be constant in order to comply with the assumption of

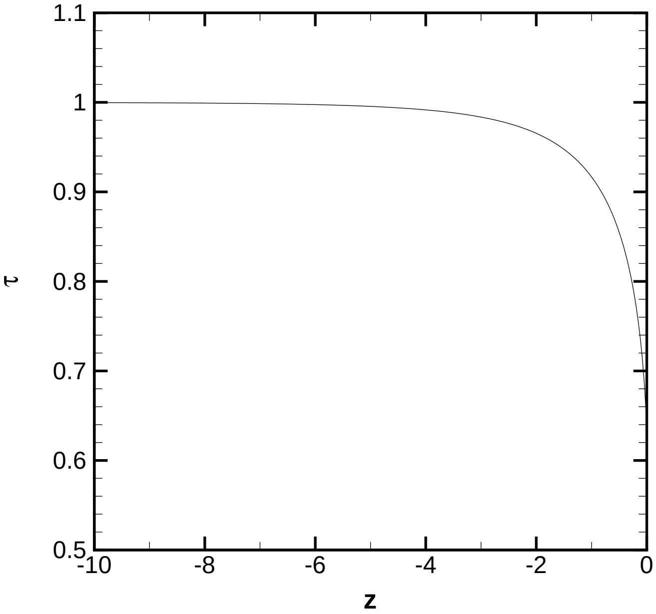

Figure 3.5: Profile of ion temperature in the shadowing sheath solution.

zero electric fields. However, it is illustrative to relax that assumption and derive a plasma potential from the ion density profile. This can be accomplished by assuming plasma neutrality, so that the local electron density is equal to the ion density, and then further assuming the Boltzmann relation for the electrons, so that the electron density is a function of the plasma potential.

The resulting expression for the potential is a function of the ion density as in Eq. 3.22, and the resulting potential profile is shown in Fig. 3.6. In this form it is assumed that the potential far from the surface is zero, and the potential at the surface cannot be assigned.

$$\Phi\left(z\right) = \ln\left(n_i'\right) \tag{3.22}$$

Valsaque *et al.* have compared this derived potential profile with the potential profile obtained from numerical kinetic simulations that include electric fields [66]. The analytical shadowing profile shows surprisingly good agreement with the kinetic

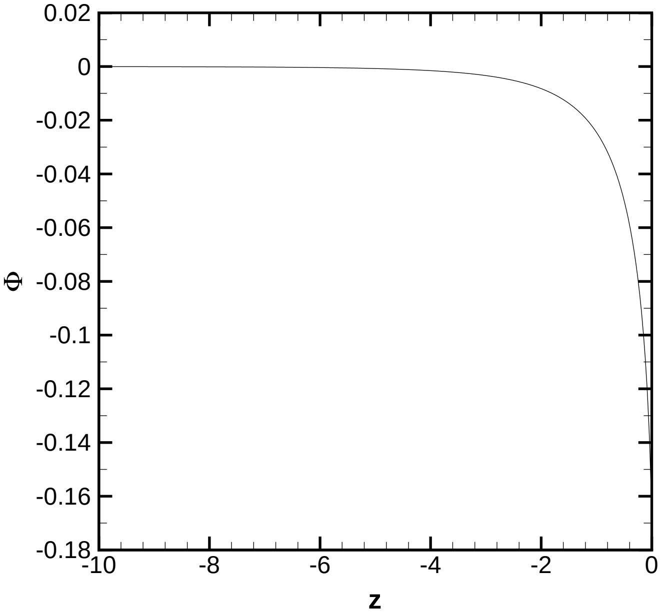

Figure 3.6: Profile of plasma potential in the shadowing sheath solution.

model results in that paper, prompting the conclusion that electric field effects are not predominant and that geometric shadowing is the primary mechanism that drives ion properties in the sheath. The primary effect of the electric field seems to be a smoothing of the distribution function that avoids the abrupt change in derivative at $M = 0$ that appears in the analytical distribution function.

While there is some support for the accuracy of the derived potential, the geometric shadowing model remains fundamentally a gasdynamic model. The trends observed in the local ion density, velocity, and temperature profiles are all consistent with a neutral, expanding flow. Essentially, the backward flowing particles behave as a counterflowing wake region superimposed on the uniform forward flow. A more meaningful alternative interpretation is that backward flowing particles expand into the sheath from the ambient plasma in order to replace the particles that are shadowed out by the surface.

3.3 Collisionless Planar Bohm Sheath

One of the earliest solutions to the plasma sheath is the collisionless planar Bohm sheath model. In this solution, a neutral plasma is modeled with a collisionless fluid description of the ions and the Boltzmann relation for the electrons. Self-consistent electrostatic fields are determined through the electrostatic Poisson equation. The concept of a presheath and an important stability criterion are introduced in the analysis of this sheath model.

The derivation presented here is unique in that it considers multiple ion species with arbitrary charge states. This form is useful for application to the complicated ion distributions expected in an EP exhaust plume. The original single species form can be easily recovered at any point, and is better suited to demonstrate the Bohm criterion.

3.3.1 Fluid equations and a solution

The inflowing plasma in this model is fully ionized, neutral, and consists of isothermal electrons and one or more cold ion species (i.e., $T_i = 0$) flowing toward a perfectly absorbing surface [1, 3]. In the sheath, electrons and ions only interact with the self-consistent potential field. For simplicity, the potential is assumed to be zero and have zero gradient at the sheath edge, $\phi\left(x=0\right)=0$ and $\nabla\phi|_0 = 0$. At the surface, the potential is a fixed negative value $\phi\left(x=L\right)=-\phi_w$. This geometry is shown schematically in Fig. 3.7. The thickness of the sheath L is not known initially.

Under the assumptions that the sheath is steady, collisionless, and planar, conservation of mass for each ion species reduces to conservation of mass flux as in Eq. 3.23, which can be further simplified to conservation of number flux by dividing through by the ion mass. The subscript j refers to the j^{th} ion species, and the subscript s

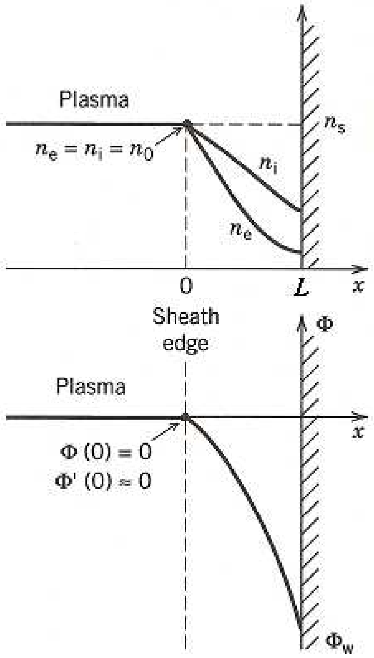

Figure 3.7: Schematic of the planar Bohm sheath geometry.

denotes properties at the edge of the sheath.

$$m_j n_{js} v_{js} = m_j n_j v_j \tag{3.23}$$

Conservation of energy in a steady, collisionless, planar sheath reduces to the Lagrangian form in Eq. 3.24, consisting of a kinetic energy term $\left(\frac{1}{2}mv^2\right)$ and an electrostatic potential energy term $(e\phi)$. The ion charge state is an integer multiple Z_j of the electron charge, which factors into the potential energy term.

$$\frac{1}{2}m_j v_{js}^2 = \frac{1}{2}m_j v_j^2\,(x) + Z_j e\phi\,(x) \tag{3.24}$$

The velocity at any point in the sheath can then be related to initial velocity and local plasma potential by rearranging the conservation of energy to the form in Eq. 3.25. This intermediate result can be combined with the conservation of number flux to yield Eq. 3.26, which expresses the local ion density only in terms of the sheath edge properties and the local plasma potential.

$$v_j\left(x\right)=v_{js}\left(1-2\frac{Z_je\phi\left(x\right)}{m_jv_{js}^2}\right)^{1/2} \tag{3.25}$$

$$n_j\left(x\right)=n_{js}\frac{v_{js}}{v_j\left(x\right)}=n_{js}\left(1-2\frac{Z_je\phi\left(x\right)}{m_jv_{js}^2}\right)^{-1/2} \tag{3.26}$$

The isothermal electron fluid is assumed to follow the Boltzmann relation throughout the sheath. Since the inflowing plasma is neutral, the electron density at the sheath edge must be equal to the total positive charge density due to the ions. That density is found by taking a sum over all ion densities, weighted by the charge state of each species. The resulting n_{es} in Eq. 3.27 gives the electron density at the sheath edge.

$$n_{es}=\sum Z_jn_{js} \tag{3.27}$$

The sheath edge becomes the preferred reference point for the Boltzmann relation, Eq. 3.28, since both the potential and electron density are known there.

$$n_e\left(x\right)=n_{es}\exp\left(\frac{e\phi\left(x\right)}{k_BT_e}\right) \tag{3.28}$$

In Eq. 3.29 the electrostatic Poisson equation relates the potential to the local charge densities. A weighted sum over the various ion species is necessary to obtain the positive charge density.

$$\frac{d^2\phi}{dx^2}=-\frac{e}{\varepsilon_0}\left(\sum Z_jn_j\left(x\right)-n_e\left(x\right)\right) \tag{3.29}$$

Inserting Eqs. 3.26 and 3.28 into this form produces the non-linear differential equation for potential shown in Eq. 3.30. To simplify the notation, $\phi\left(x\right)$ is written as ϕ from this point on.

$$\frac{d^2\phi}{dx^2}=\frac{e}{\varepsilon_0}\left[n_{es}\exp\left(\frac{e\phi}{k_BT_e}\right)-\sum_j Z_jn_{js}\left(1-2\frac{Z_je\phi}{m_jv_{js}^2}\right)^{-1/2}\right] \tag{3.30}$$

This equation can be recast using the normalized variables of Eq. 3.31. The Debye length λ_D and Bohm velocity v_B are appropriate length and velocity scales, and the Mach number with respect to Bohm velocity appears. A new parameter r_{js} is the freestream charge fraction for the j^{th} ion species.

$$z = \frac{x}{\lambda_D},\ M_j = \frac{v_j}{v_B},\ \Phi = \frac{e\phi}{k_B T_e},\ r_{js} = \frac{n_{js}}{n_{es}} \tag{3.31}$$

The differential equation takes the form in Eq. 3.32 after normalizing and rearranging.

$$\frac{d^2\Phi}{dz^2} = \exp\left(\Phi\right) - \sum_j Z_j r_{js} \left(1 - 2\frac{Z_j\Phi}{M_j^2}\right)^{-1/2} \tag{3.32}$$

This form can be integrated once analytically by multiplying the entire expression by $\frac{d\Phi}{dz}dz$ as shown in Eq. 3.33. The limits of integration are from the sheath edge at $z = 0$ to any arbitrary position in the sheath, $0 < z < L$. The boundary conditions on potential at the sheath edge are $\Phi\left(0\right) = 0$ and $\frac{d\Phi}{dz}|_0 = 0$. Note that each term in the summation can be integrated separately.

$$\int_0^z \frac{d^2\Phi}{dz^2}\frac{d\Phi}{dz}dz = \int_0^z \exp\left(\Phi\right)\frac{d\Phi}{dz}dz - \int_0^z \sum_j Z_j r_{js}\left(1 - 2\frac{Z_j\Phi}{M_j^2}\right)^{-1/2}\frac{d\Phi}{dz}dz \tag{3.33}$$

The slightly more complicated form in Eq. 3.34 is found after integration. At this point a numerical method is required to integrate a second time to obtain the potential. The modified form in Eq. 3.35 is better suited to numerical integration, although some care must be taken to choose the proper root of the radical.

$$\frac{1}{2}\left(\frac{d\Phi}{dz}\right)^2 = \exp\left(\Phi\right) - 1 + \sum_j r_{js} M_j^2 \left[\left(1 - 2\frac{Z_j\Phi}{M_j^2}\right)^{1/2} - 1\right] \tag{3.34}$$

$$\frac{d\Phi}{dz} = \sqrt{2\left\{\exp\left(\Phi\right) - 1 + \sum_j r_{js} M_j^2 \left[\left(1 - 2\frac{Z_j\Phi}{M_j^2}\right)^{1/2} - 1\right]\right\}} \tag{3.35}$$

Since the length of the sheath is not known, it is useful to perform a coordinate transform such that the probe surface is at $z = 0$ and then integrate this equation

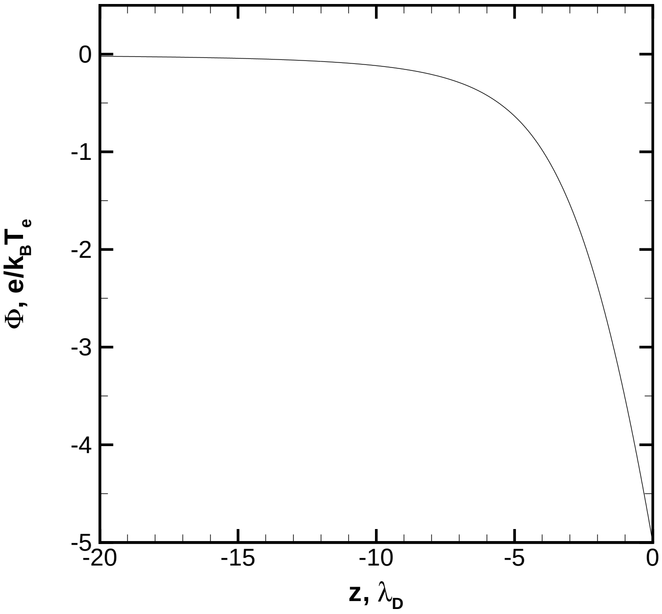

Figure 3.8: Profile of plasma potential in the Bohm sheath solution.

by marching from the surface out to the sheath edge at $z = -L$. Since the potential at the surface is known, $\frac{d\Phi}{dz}$ can be calculated and Eq. 3.35 can then be solved as an initial value problem. This approach reveals that the solution for potential approaches $\Phi = 0$ asymptotically, leading to an infinitely long sheath. In practice, the solution can be terminated at an arbitrary distance or potential.

An example solution is obtained for the case $M = 1$. The profile of plasma potential is shown in Fig. 3.8. Once the potential has been obtained, the local plasma properties can be calculated from previous expressions. The ion velocity and density can be calculated from Eqs. 3.25-3.26, and the electron density can be calculated from Eq. 3.28. The profiles of ion and electron density are shown in Fig. 3.9.

3.3.2 The Bohm criterion

Since the conditions for a steady solution are not readily apparent from Eq. 3.35, consider the simplification to a plasma with one species of single charge ions. The

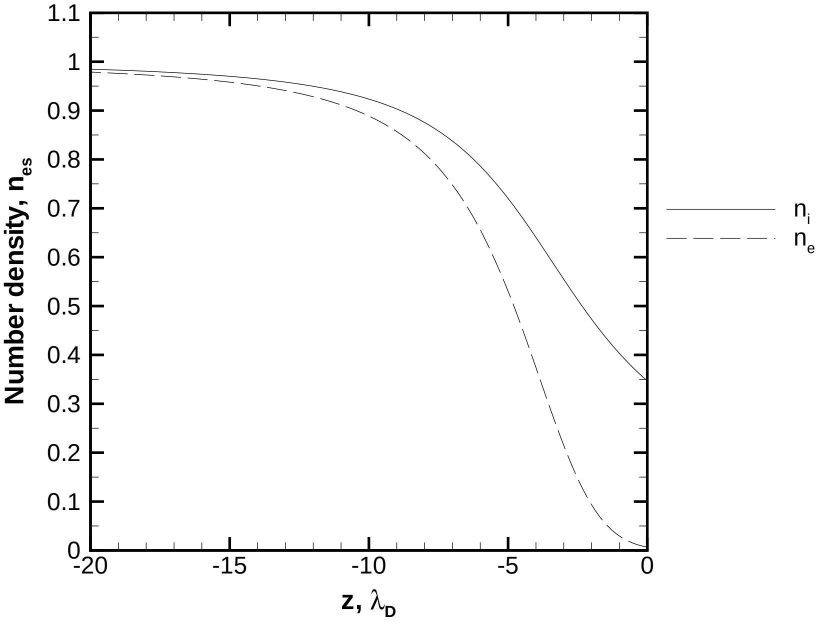

Figure 3.9: Profiles of ion and electron number density in the Bohm sheath solution.

summation over species simplifies to a single term, the freestream charge fraction becomes $r_{js} = 1$, and the charge state becomes $Z_j = 1$ as in Eq. 3.36. The boundary conditions on potential at the sheath edge remain $\Phi(0) = 0$ and $\frac{d\Phi}{dz}|_0 = 0$.

$$\frac{d\Phi}{dz} = \sqrt{2\left\{\exp(\Phi) - 1 + M^2\left[\left(1 - 2\frac{\Phi}{M^2}\right)^{1/2} - 1\right]\right\}} \tag{3.36}$$

The quantity in the radical must be positive for a non-oscillatory sheath solution, and this imposes a constraint on the Mach number when the potential Φ is small. In order to evaluate that constraint, both terms containing the potential are expressed as Taylor expansions about $\Phi = 0$ in Eqs. 3.37 and 3.38, following the analysis by Bohm [3]. The expansions are carried out to second order, since the lower order terms will cancel out.

$$\exp(\Phi) = 1 + \Phi + \frac{\Phi^2}{2} + \ldots \tag{3.37}$$

$$\left(1 - \frac{2}{M^2}\Phi\right)^{1/2} = 1 - \frac{1}{2}\left(\frac{2}{M^2}\Phi\right) - \frac{1}{8}\left(\frac{2}{M^2}\Phi\right)^2 + \ldots \tag{3.38}$$

The expansions are then inserted into the argument of the radical in Eq. 3.39 and simplified to the result in Eq. 3.40. The inequality indicates the condition to ensure a stable sheath solution.

$$1 + \Phi + \frac{\Phi^2}{2} - 1 + M^2 \left[1 - \frac{1}{2}\left(\frac{2}{M^2}\Phi\right) - \frac{1}{8}\left(\frac{2}{M^2}\Phi\right)^2 - 1\right] \geq 0 \tag{3.39}$$

$$\frac{\Phi^2}{2}\left(1 - \frac{1}{M^2}\right) \geq 0 \tag{3.40}$$

Drawing a conclusion from the inequality, a steady solution for the sheath only exists if $M > 1$. This is the Bohm criterion, which has the physical interpretation that the ion speed must be greater than the Bohm velocity at the edge of the sheath. However, in many applications a stationary bulk plasma is in contact with a surface. In such cases a presheath region is required, where small electric fields act to accelerate ions up to the Bohm velocity at the edge of the sheath. A presheath requires the original assumption of zero electric field at the sheath edge to be relaxed.

3.3.3 Results and Discussion

Exact similarity with the geometric shadowing sheath model conditions cannot be achieved. However, the potential at the surface and the inflow Mach number can be matched in order to facilitate a comparison between the results from both models. The shadowing model example was solved for a single ion population with a Mach number $M_D = 1$, and the calculated potential at the probe surface in Fig. 3.6 is $\Phi_w = -0.1728$ at $z = 0$. These conditions satisfy the Bohm criterion, so the same wall potential and Mach number are assumed in this example solution of the Bohm sheath model.

The differential equation in Eq. 3.36 is solved for the potential profile in the sheath as shown in Fig. 3.10. Since the Bohm criterion is satisfied, the solution has

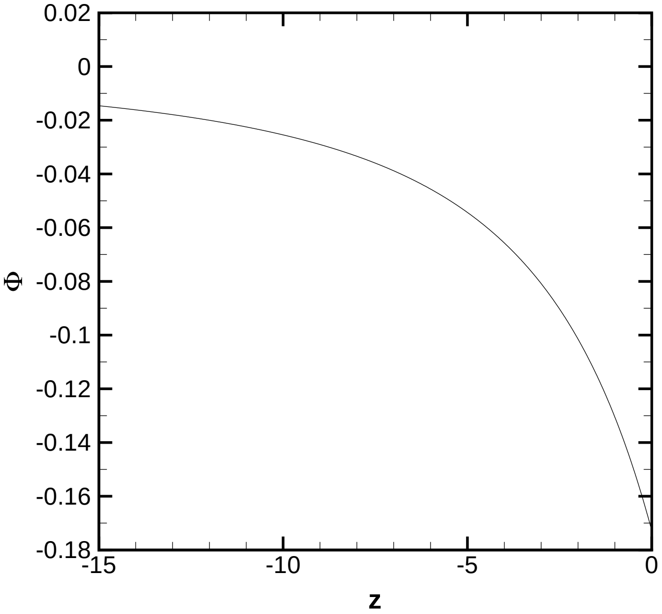

Figure 3.10: Profile of potential from the Bohm sheath.

no oscillatory aspect and decreases monotonically from the freestream to the surface at $z = 0$. The potential asymptotically approaches zero far from the surface as mentioned previously.

The ion and electron densities can then be calculated from this potential using normalized forms of the Boltzmann relation from Eq. 3.28, and local ion density from Eq. 3.26. The Bohm sheath solution indicates a non-neutral region near the probe, as evidenced by separation of the density profiles in Fig. 3.11. The non-neutral region is a physically meaningful feature, since the large disparity between ion and electron mass makes the electrons more mobile than the ions. Electrons respond to the negative probe potential more strongly than ions, leading to a region of non-neutral plasma near the surface.

Although both ion and electron density decrease as the flow approaches the surface, two different processes are responsible. The negative potential acts to accelerate

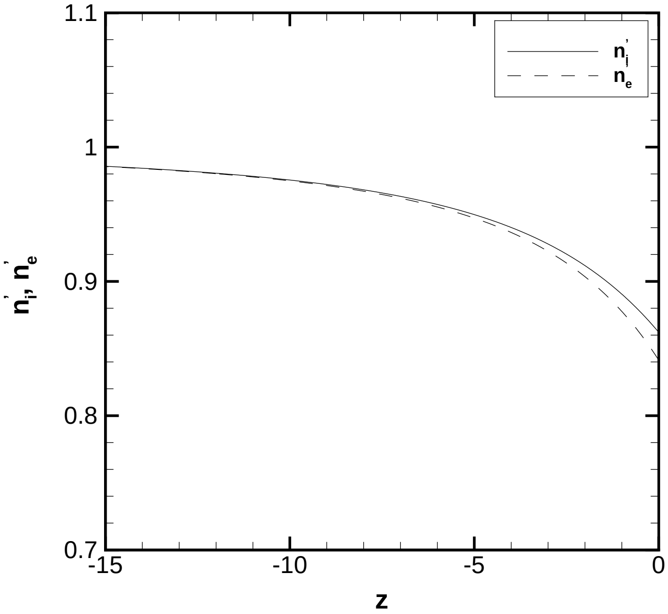

Figure 3.11: Profiles of ion and electron density from the Bohm sheath.

the ions toward the probe, as seen from the profile of ion velocity in the sheath in Fig. 3.12. The flux is the product of local density and local velocity, and it is clear from Eqs. 3.25-3.26 that the flux must be constant for the ions. Since the ion flow maintains a constant flux, the ion density decreases as the ion velocity increases.

In contrast, the negative potential acts to repel the electrons, so only those electrons with sufficient initial kinetic energy are able to reach the local potential. In this model the electrons follow the Boltzmann relation, so the electron density shows an exponential fall off as the potential decreases. Since the wall potential is relatively small compared to the electron temperature in this example, there is not a significant decrease in electron density.

One of the attractive features of the Bohm sheath model is that the solution can be readily returned to dimensional variables if the electron temperature and freestream density are known. This process is equally straightforward for the situation with

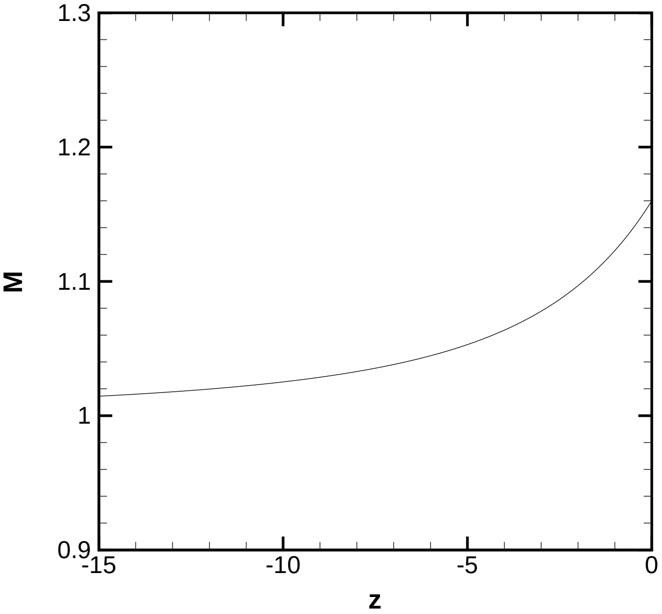

Figure 3.12: Profile of ion velocity from the Bohm sheath.

multiple ion components. This makes the Bohm sheath a useful tool for practical design purposes in both experimental and computational settings.

3.4 Comparison of model results

The geometric shadowing sheath model and the planar Bohm sheath model cannot reproduce exactly the same inflow conditions. This limitation stems from the different assumptions about the inflowing ions made in the models. The Bohm sheath model assumes one or more cold ion species, with zero ion temperature, while the shadowing sheath model assumes a Maxwellian ion distribution with a non-zero temperature.

The shadowing sheath model could achieve a cold ion condition by taking the limit of $\tau_\infty = 0$, corresponding to an ion temperature that is negligible compared to the electron temperature. However, that causes the normalized Maxwellian distribution (Eq. 3.21) to approach a delta function at the drift Mach number. All of the interesting behavior in the shadowing model derives from partial shadowing of the distribution function, so that limit would produce constant properties throughout the sheath.

Instead, it is more useful to achieve partial similarity by matching the inflowing ion Mach number and some property at the surface. The obvious choice is to set the potential at the surface, since that is usually controlled in experimental applications. In the shadowing sheath model however, the surface potential is not coupled into the solution and is only found afterward. As such, the shadowing sheath model must be solved first, and the calculated surface potential can then be used in the Bohm sheath model.

This process was carried out in Secs. 3.2.2 and 3.3.3. The ion density profiles offer the most meaningful comparison, since both sheath models actually calculate ion density. Then a visual inspection of Fig. 3.3 for the shadowing sheath and the ion density profile of Fig. 3.11 for the Bohm sheath gives some insight into how well the models agree. At first glance, there seems to be no agreement at all. The profile in the shadowing model shows a thin sheath, with all of the density variation occurring within 5 Debye lengths of the surface. The profile from the Bohm sheath model shows a much thicker sheath, with nearly 7% deviation from the freestream density at more than 15 Debye lengths from the surface.

However, the shadowing sheath model has one undetermined parameter, the exchange frequency W. The exchange frequency is equal to the plasma frequency in the previous solution, which implies that ion particle exchange occurs on an electron timescale. In fact the ion exchange frequency should occur on an ion timescale, which would correspond to a much smaller value of W. The exchange frequency modifies the length scale of the shadowing sheath, and a smaller value produces a thicker sheath.

An estimate of the exchange frequency that brings the shadowing sheath model into better agreement with Bohm sheath model is obtained by a least-square error technique. An ion number density profile is computed from the shadowing sheath model for varying W. Since the distribution at the surface is not affected, the potential at the surface is unchanged and the previous Bohm sheath solution can be used as a fixed reference. A value of W is found that minimizes the sum of square error between the ion density profiles from both models, computed at 1500 fixed points along the profiles.

For the inflow conditions of $M_D = 1$ and $\tau_\infty = 1$, the least-square fit for the exchange frequency is found to be $W = 0.088$. The resulting profiles of ion density are shown in Fig. 3.13, and profiles of potential are shown in Fig. 3.14. For the ion density the agreement between the shadowing sheath model and the Bohm sheath model is generally very good. The potential shows larger discrepancies, but recall that in the shadowing sheath model the potential is assumed to be related to the ion density via neutrality and the Boltzmann relation.

It should be noted that the value of the exchange frequency reported above is only effective at the given flow conditions. There is no single value that can achieve consistent agreement between the two sheath models over a broad range of plasma conditions. It may be possible to develop a functional form of the exchange frequency as $W\left(M_D, \tau_\infty\right)$, but that lies beyond the scope of this work.

From a philosophical viewpoint, the two models are intended to describe different aspects of the sheath. The Bohm sheath model isolates the effects of self-consistent electrostatic fields, while the shadowing model isolates the effects of non-equilibrium in the local distribution function. Together these models provide some understand-

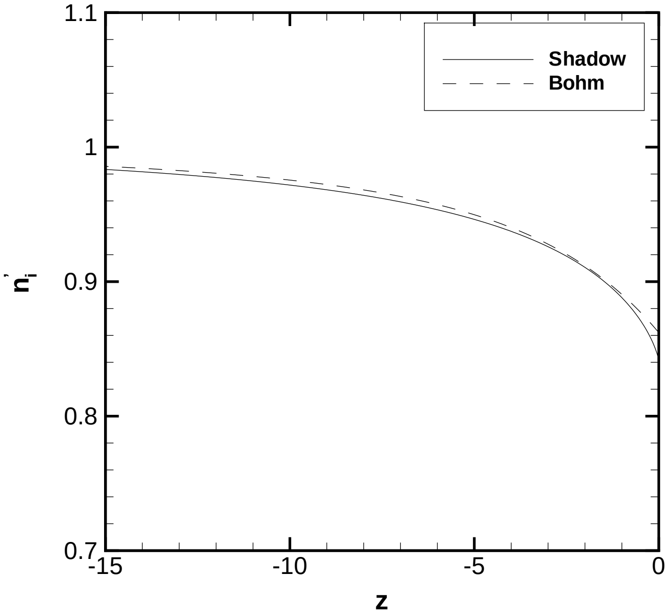

Figure 3.13: Profiles of ion density from the Bohm sheath and the best-fit shadowing sheath.

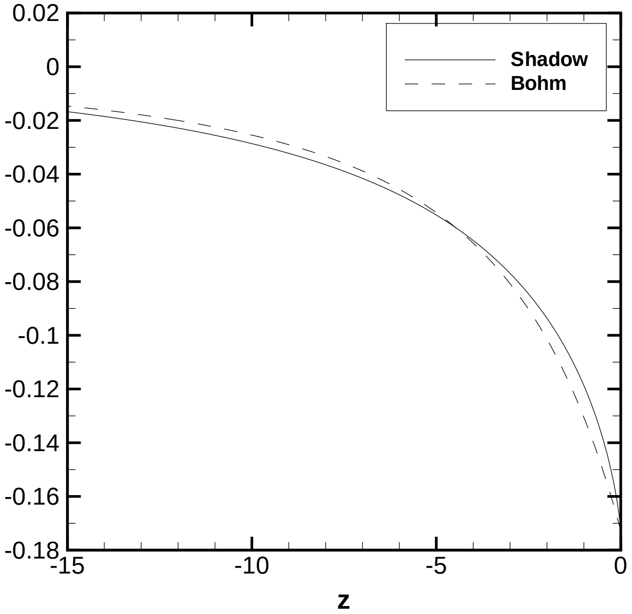

Figure 3.14: Profiles of potential from the Bohm sheath and the best-fit shadowing sheath.

ing of the physical processes at work, and form the foundation for more advanced modeling techniques. In the next chapter, a computational code is discussed that incorporates elements from the kinetic description and the fluid description in order to achieve a high-fidelity simulation of a plasma.

Chapter IV

Hybrid Fluid PIC-DSMC Numerical Model

A recurring theme is that the governing equations for a plasma cannot be solved analytically for most practical applications. As a result, a variety of techniques have been developed to obtain numerical solutions to the kinetic models, Euler equations, Navier-Stokes equations, and MHD equations. This chapter describes a hybrid model that incorporates both a particle method and a fluid method to describe a plasma.

When choosing a numerical model it is important to identify the degree of non-equilibrium in the flow. For strongly collisional flows that remain near equilibrium, a fluid method is much less computationally intensive than a particle method and should produce equally accurate results. At the other extreme, nearly collisionless flows or flows that incorporate a strongly non-equilibrium process may require a particle method to obtain accurate results at all. In some cases one region of a flow might be adequately treated with a fluid method, while another region of the flow requires the increased fidelity of a particle method. Flows with localized non-equilibrium can benefit from hybrid techniques described by Schwartzentruber *et al.* [67] that use either fluid or particle methods for distinct regions of a flow.

Plasmas are composed of both ions and electrons, and the large mass ratio between those particles introduces additional forms of non-equilibrium. Ionization energy from generating the plasma is carried primarily by the electrons, resulting in a higher temperature for electrons than for ions. The combination of higher temperature and lower mass leads to a higher collision rate for electrons, so that the electron relaxation time is much shorter than the ion relaxation time. Although collisions between ions and electrons generally act to bring the entire plasma toward equilibrium, the mass ratio makes these collisions much less effective than collisions between two electrons or collisions between two ions.

Since there is a significant difference between the electron and ion time scales, it is useful to consider an intermediate time scale where the ion motions are accurately resolved and the electron motions can be averaged. This leads to a hybrid approach that uses a particle method to model the ions and a fluid method to model the electrons. Hybrid techniques of this sort have been used successfully for EP modeling [68, 69, 70], and are also well-suited to plasma diagnostic modeling.

4.1 Ion and neutral particle models

It is not feasible to solve the full kinetic description of an ion plasma, but probabilistic particle simulations incorporate much of the same underlying physical reasoning. Two complementary methods are used to model the ion and neutral particles in this work. The Particle In Cell (PIC) method is used to move the ion and neutral particles and to calculate self-consistent electric fields that act on charged particles. The Direct Simulation Monte Carlo (DSMC) method is used to model particle collisions.

4.1.1 Particle In Cell

The motion of a charged particle is determined by the collective electric and magnetic fields generated by all other charged particles in the plasma. In order to obtain a physically meaningful solution, the differential equations for electric and magnetic fields in Maxwell's laws must be solved in tandem with the particle equations of motion.

The PIC method [47] accomplishes this by tracking macroparticle motion and electric field calculations on a computational grid. Each macroparticle represents many ions or neutrals, and is assigned average properties from the prescribed distribution function. Particle movement can be decoupled from the field calculations by choosing a time step such that the displacement is small and the local fields do not vary significantly. This method consists of the following four main steps.

First, the charge density is weighted from particle position to the nodes of the computational grid. In this work, the weighting scheme is a simple bilinear interpolation for an axisymmetric, structured, rectangular grid. Alternative weighting schemes can be devised for this and other computational grid geometries.

Second, electric fields are calculated by solving the appropriate electrostatic or electrodynamic equation over all the nodes of the computational grid. Often the electric potential is solved instead by using the electrostatic Poisson equation, and electric fields are then calculated from the gradient of the potential. Maxwell's equations must be solved if magnetic fields are significant or if accurate time evolution is required.

Third, the particle acceleration is calculated by weighting the electric fields from the nodes to the particles. The particle velocity can then be updated as well. Again, a simple bilinear interpolation is used in this work.

Fourth, particles are moved for a time step with the new velocity. Any boundary interactions are handled at this point, including particle injection at the inlet and particle removal at edges. The velocity of new particles is assigned probabilistically from the assigned distribution function at the inlet.

These four steps are then repeated over a desired number of iterations. Depending on how the particles are initialized in the computational domain, some initial transients may occur. Sampling of the instantaneous density and electric fields allows the statistical scatter to be reduced over a number of iterations.

The PIC method is essentially a collisionless formulation of kinetic theory for a plasma. However, collisions provide the mechanism for ionization and recombination and contribute to the electrical resistance in a plasma. Since these processes may affect the current, it is important for a plasma diagnostic simulation to have the capability to model collisions.

4.1.2 Direct Simulation Monte Carlo

Collisions are incorporated through the DSMC method, which was developed extensively by Bird [48]. Since the actual number of particles and collisions is far too large for direct simulation, DSMC tracks macroparticle motion on a computational grid. At each collision time step, particles are paired up by computational cell and collisions are evaluated statistically. This method can be readily integrated with the PIC method to include both collisions and charged particle motion with self-consistent electric fields.

In a PIC-DSMC formulation, the main role of the DSMC method is to handle collisions. This involves a series of calculations to determine the number of collisions in each cell, the collision probability for each pair of particles, and the new particle properties after a collision occurs.

The number of simulated collisions in a cell can be calculated by taking the product of collision frequency and the collision time step, with an additional factor accounting for the macroparticle weights in the cell. The result from kinetic theory in Eq. 4.1 gives the collision frequency ν_{ab} of species a with species b as a function of the density of the target species n_b, the mean relative speed $\overline{v_{ab}}$, and a collision cross section σ_{ab} [59]. In this work only xenon-xenon collisions are modeled. A variable hard sphere (VHS) model with $\omega = 0.12$ is used to calculate the atom-atom collision cross section as in 4.2. The cross section for atom-ion charge exchange collisions is given by the empirical fit in Eq. 4.3 [71]. In these expressions the relative speed is in units of $\frac{m}{s}$. No ion-ion collisions are modeled.

$$\nu_{ab} = n_b \overline{v_{ab}} \sigma_{ab} \tag{4.1}$$

$$\sigma_{Xe-Xe} = \frac{2.12 \times 10^{-18}\, m^2}{v_{ab}^{2\omega}} \tag{4.2}$$

$$\sigma_{Xe-Xe^+} = 2\left[142.21 - 23.30 \log |v_{ab}|\right] \left(\frac{12.13}{13.6}\right)^{-\frac{3}{2}} \times 10^{-20}\, m^2 \tag{4.3}$$

A random pair of particles is selected from the cell for each simulated collision. Whether or not the collision occurs is determined statistically by an acceptance-rejection method, where a random number is compared to the collision probability. If the random number is larger than the probability, the collision occurs and the particles velocities are processed.

The post-collision particle velocities are calculated as a result of random scattering, subject to conservation of momentum and energy for the particles. A new relative velocity is calculated, and a new angle is selected. The new velocities for both particles are then calculated from the new relative velocities and the center of mass velocity.

These steps are repeated at every collision time step. As was assumed in the PIC method, the collision time step is small enough that particle displacement is small and the particle movement can be decoupled from the collision calculations. Again, sampling can be used to reduce the statistical scatter introduced by this treatment of the collisions.

4.2 Electron fluid models

The electron fluid models used in this work are derived from the MHD equations presented in Chapter III. Three distinct models are used: the Boltzmann model, the non-neutral detailed model, and the Poisson-consistent detailed model. These models progressively increase the fidelity of the electron fluid from a simple Boltzmann relation to a coupled electrostatic fluid model. Each of the models has unique requirements and limitations as described in the following sections.

4.2.1 Derivation from electrostatic MHD equations

Each of the three electron fluid models can be derived from the electrostatic MHD equations. The electrostatic MHD equations are obtained by taking the limit of zero magnetic fields ($\mathbf{B} = 0$) in the fluid conservation laws and Maxwell's laws. The resulting equation set includes conservation of mass or continuity, Eq. 4.4, conservation of momentum, Eq. 4.5, conservation of energy, Eq. 4.6, and the electrostatic Poisson equation, Eq. 4.7. These equations are written specifically for an electron fluid, and the negative electron charge has been taken into account by adjusting the signs of the relevant terms.

$$\frac{\partial \rho_e}{\partial t} + \nabla \cdot (\rho_e \mathbf{v}_e) = 0 \tag{4.4}$$

$$\frac{\partial (\rho_e \mathbf{v}_e)}{\partial t} + \nabla \cdot (\rho_e \mathbf{v}_e \mathbf{v}_e) = -\nabla P_e - \rho_e \frac{e}{m_e} \mathbf{E} + \rho_e \frac{e}{m_e} \frac{\mathbf{j}_e}{\sigma} \tag{4.5}$$

$$\frac{\partial (\rho_e e)}{\partial t} + \nabla \cdot (\rho_e e \mathbf{v}_e) = -P_e \nabla \cdot \mathbf{v}_e - \rho_e \frac{e}{m_e} \mathbf{E} \cdot \mathbf{v}_e - \nabla \cdot \mathbf{q} \tag{4.6}$$

$$\nabla \cdot \mathbf{E} = \frac{e}{\varepsilon_0} (n_i - n_e) \tag{4.7}$$

A number of assumptions and simplifications are common to all three electron fluid models. The first simplification is to take the steady state limit, so that $\frac{\partial}{\partial t} = 0$ in each of the conservation laws.

The density ρ_e in the conservation laws is rewritten in terms of number density n_e according to Eq. 4.8. This provides a single consistent variable for the conservation laws and the electrostatic Poisson equation, and also avoids any numerical complications from working with the small value of the electron mass.

$$\rho_e = m_e n_e \tag{4.8}$$

The ideal gas law is assumed as the equation of state for the electron fluid. The pressure and internal energy can then be replaced by the forms in Eq. 4.9 and Eq. 4.10, which use the density and temperature.

$$P_e = n_e k_B T_e \tag{4.9}$$

$$e = \frac{3}{2} \frac{k_B T_e}{m_e} \tag{4.10}$$

The electric field is expressed in terms of the plasma potential ϕ as given in Eq. 4.11. With this substitution, the electrostatic Poisson equation becomes a mathematical Poisson equation for the potential.

$$\mathbf{E} = -\nabla\phi \tag{4.11}$$

The heat flux vector is assumed to follow the Fourier heat conduction law given in Eq. 4.12, with the electron thermal conductivity κ as a parameter.

$$\mathbf{q} = -\kappa \nabla T_e \tag{4.12}$$

The electron transport coefficients are evaluated using the basic definitions from molecular transport [60]. The electrical conductivity σ in Eq. 4.13, and the thermal conductivity κ in Eq. 4.14, both depend on the total electron collision frequency ν_e.

$$\sigma = \frac{n_e e^2}{m_e \nu_e} \tag{4.13}$$

$$\kappa = \frac{2.4 n_e k_B^2 T_e}{m_e \nu_e} \left(\frac{1}{1 + \frac{\nu_{ei}}{\nu_e \sqrt{2}}} \right) \tag{4.14}$$

The total electron collision frequency is the sum of the electron-ion collision frequency ν_{ei} and the electron-neutral collision frequency ν_{en} as defined in Eq. 4.15. The electron-ion collision frequency in Eq. 4.16 is calculated from classical elastic scattering [60], while the electron neutral collision frequency in Eq. 4.17 is calculated using an empirical fit [72] of the electron-neutral cross section $Q_{en}(T_e)$ in the general form of Eq. 4.1.

$$\nu_e = \nu_{ei} + \nu_{en} \tag{4.15}$$

$$\nu_{ei} = n_i \frac{4\sqrt{2\pi}}{3} \left(\frac{m_e}{k_B T_e} \right)^{\frac{3}{2}} \left(\frac{e^2}{4\pi\varepsilon_0 m_e} \right)^2 \ln \left| 12\pi \left(\frac{\varepsilon_0 k_B}{e^2} \right)^{\frac{3}{2}} \left(\frac{T_e^3}{n_e} \right)^{\frac{1}{2}} \right| \tag{4.16}$$

$$\nu_{en} = n_n \frac{4}{3} \left(\frac{8 k_B T_e}{\pi \mu_{en}} \right)^{\frac{1}{2}} Q_{en}(T_e) \tag{4.17}$$

After making these assumptions and substitutions, the equation set can be written as in Eqs. 4.18-4.21. The remaining terms on the left hand side of the momentum and energy equations have been expanded and simplified using the continuity equation. In this form it appears that there are four coupled equations for five independent variables: n_e, $\mathbf{v}_e$, T_e, ϕ, and $\mathbf{j}_e$. However, the current can be expressed in terms of the density and velocity as $\mathbf{j}_e = e n_e \mathbf{v}_e$. For now the current is left in place as a reference marker for further manipulation.

$$\nabla \cdot (n_e \mathbf{v}_e) = 0 \tag{4.18}$$

$$m_e n_e \mathbf{v}_e \nabla \cdot \mathbf{v}_e = -\nabla (n_e k_B T_e) + n_e e \nabla\phi + n_e e \frac{\mathbf{j}_e}{\sigma} \tag{4.19}$$

$$n_e \mathbf{v}_e \cdot \nabla \left(\frac{3}{2} k_B T_e \right) = -n_e k_B T_e \nabla \cdot \mathbf{v}_e + n_e e \nabla\phi \cdot \mathbf{v}_e + \nabla \cdot (\kappa \nabla T_e) \tag{4.20}$$

$$\nabla^2 \phi = -\frac{e}{\varepsilon_0}\left(n_i - n_e\right) \tag{4.21}$$

Following the example of Boyd and Yim [73], there are a few additional manipulations that will simplify the numerical solution.

By introducing a stream function Ψ as defined in Eq. 4.22, the continuity equation becomes a Laplace equation as given in Eq. 4.23. With this modification, all of the differential equations from the conservation laws and the electrostatic Poisson equation are ultimately expressed in terms of the Laplacian operator. A single solution technique can then be used to solve each of the differential equations.

$$\nabla \Psi = n_e \mathbf{v} \tag{4.22}$$

$$\nabla^2 \Psi = 0 \tag{4.23}$$

The momentum equation can be simplified by neglecting the inertial term ($\sim m_e n_e \mathbf{v}$), since it is much smaller than the other terms. The remaining terms can then be rearranged as Eq. 4.24 to isolate the electron current.

$$\mathbf{j}_e = \sigma \left[\frac{k_B}{e}\left(\nabla T_e + T_e \frac{\nabla n_e}{n_e}\right) - \nabla \phi\right] \tag{4.24}$$

The energy equation can be rearranged as shown in Eq. 4.25, which facilitates a solution for the temperature.

$$\nabla^2 T_e + \left(\frac{\nabla \kappa}{\kappa} - \frac{3}{2}\frac{k_B}{\kappa} n_e \mathbf{v}\right) \cdot \nabla T_e - \left(\frac{k_B}{\kappa} n_e \nabla \cdot \mathbf{v}\right) T_e - \frac{e}{\kappa} n_e \nabla \phi \cdot \mathbf{v} = 0 \tag{4.25}$$

All three electron fluid models work with this modified set of equations: the electrostatic Poisson equation, Eq. 4.21, the continuity equation, Eq. 4.23, the current equation, 4.24, and the temperature equation, Eq. 4.25. Further development of the three models diverges at this point, so each model is described separately in the following sections.

4.2.2 Boltzmann model

The Boltzmann model is obtained by making the assumptions that lead to the Boltzmann relation. Briefly, the electron fluid must be unmagnetized, collisionless, isothermal, and currentless. The first assumption, that the fluid is unmagnetized, has already been made early in the preceding development as $\mathbf{B} = 0$.

The collisionless assumption is equivalent to the limit $\nu_e \to 0$. Referring to the transport coefficients in Eqs. 4.13 and 4.14, this limit corresponds to infinite electrical and thermal conductivities. This is actually consistent with the other assumptions of isothermal and currentless fluid. A gradient in temperature drives heat flux, which acts to reduce the gradient. In the limit of infinite thermal conductivity, the heat flux redistributes the thermal energy instantaneously and produces a uniform temperature. A uniform charge distribution results from the limit of infinite electrical conductivity, so no gradient in charge exists to a drive current.

The isothermal assumption makes T_e constant throughout the flow, which replaces the temperature equation of Eq. 4.25 entirely. It also eliminates a term from the current equation, since $\nabla T_e = 0$.

The currentless assumption is applied by setting $\mathbf{j}_e = 0$ in the current equation. Factoring out the conductivity leaves only two terms from the right hand side of Eq. 4.24, which must sum to zero as in Eq. 4.26.

$$0 = \frac{k_B T_e}{e} \frac{\nabla n_e}{n_e} - \nabla \phi \tag{4.26}$$

This can be rearranged and solved by separation of variables, using the reference condition $n_e = n_{e0}$ where $\phi = \phi_0$.

$$\frac{\nabla n_e}{n_e} = \frac{e}{k_B T_e} \nabla \phi$$

$$\ln\left|\frac{n_e}{n_{e0}}\right| = \frac{e}{k_B T_e}\left(\phi - \phi_0\right)$$

Finally, the solution can be rearranged to the Boltzmann relation form in Eq. 4.27, which gives the electron density in terms of the plasma potential.

$$n_e = n_{e0}\exp\left[\frac{e}{k_B T_e}\left(\phi - \phi_0\right)\right] \tag{4.27}$$

This fluid model is exactly consistent with the Boltzmann relation assumed in the analytic sheath models. The hybrid fluid PIC results from this model correspond closely to the analysis in the planar Bohm sheath model, so results from this model are expected to be in excellent agreement with the planar Bohm sheath. Comparison of results with the analytic sheath solution can be used to validate the overall operation of the hybrid model.

The Boltzmann model is also useful for identifying and quantifying any two dimensional effects, since the only substantive difference from the planar Bohm sheath is the axisymmetric geometry. This is a useful baseline comparison to have before considering the more complicated detailed fluid models.

4.2.3 Non-neutral detailed model

The non-neutral detailed model is obtained by applying the charge continuity condition of Eq. 4.28.

$$\nabla \cdot \mathbf{j}_e = 0 \tag{4.28}$$

Inserting the expression for current from Eq. 4.24 into this form produces Eq. 4.29, which is a significantly more complicated expression of the charge continuity condition.

$$\nabla \cdot \left\{\sigma\left[\frac{k_B}{e}\left(\nabla T_e + T_e\frac{\nabla n_e}{n_e}\right) - \nabla\phi\right]\right\} = 0 \tag{4.29}$$

Since the energy equation is solved for temperature, this equation can either be solved for plasma potential or for electron number density. In the work by Boyd and Yim, this was solved for the plasma potential [73], and the assumption of plasma neutrality was used in place of the electrostatic Poisson equation.

Expanding Eq. 4.29 and rearranging to the form in Eq. 4.30 shows the character of the differential equation when solved for plasma potential. The coefficients on the potential terms are simple, but there is a complicated source term.

$$\nabla^2\phi + \left(\frac{\nabla\sigma}{\sigma}\right)\cdot\nabla\phi - \frac{k_B}{e}\nabla\cdot\left[\sigma\left(\nabla T_e + T_e\frac{\nabla n_e}{n_e}\right)\right] = 0 \tag{4.30}$$

The assumption of neutrality is not valid in a plasma sheath, so the electrostatic Poisson equation is solved for electron density in Eq. 4.31 to complete the non-neutral detailed model. This calculation is not computationally reliable: the coefficient $\frac{\varepsilon_0}{e}$ is very large, $\sim 5.5 \times 10^7$, but the calculated value of the Laplacian of the potential is very small. Put another way, there is very poor resolution of electron density from this calculation.

$$n_e = n_i - \frac{\varepsilon_0}{e}\nabla^2\phi \tag{4.31}$$

This formulation is sensitive to statistical scatter in the ion density reported from the PIC model. Averaging techniques can be used to reduce the scatter, but it is more effective to maintain a large number of computational particles per cell. Additionally, any averaging introduces some lag into the coupling between electron density and potential. This raises the possibility of artificial oscillation in the plasma potential and electron density that could overwhelm the expected physical behavior.

Since the Laplacian of electron density appears in Eq. 4.30 and the density itself is calculated from the Laplacian of plasma potential, the differential equation for potential begins to resemble a biharmonic equation. That is, taking the gradient or

Laplacian of number density introduces higher order derivatives into the differential equation for potential. The boundary conditions on potential must then be handled carefully to avoid introducing singularities in higher order derivatives. One approach is to calculate fourth order accurate boundary values, but this is difficult to enforce at points near the corners of the probe. An alternative approach is to use a stencil to calculate average values of $\nabla^2\phi$ along boundaries.

The original neutral detailed model has been used successfully, and there is reason to believe that relaxing the assumption of neutrality would result in a functional non-neutral model. However, as will be seen in the next chapter, the specific implementation of the non-neutral model in this work does not function as intended. The initialized conditions and order of calculations during iteration can only lead to a neutral solution with $\nabla^2\phi = 0$ throughout the flow field.

4.2.4 Poisson-consistent detailed model

The Poisson-consistent detailed model is also obtained by applying the charge continuity condition, and derives from the same intermediate result in Eq. 4.29. However, that equation is solved for electron number density in this model, rather than for plasma potential.

The alternative arrangement in Eq. 4.32 shows the character of the differential equation when solved for number density. The identity $n_e \nabla \frac{1}{n_e} = -\frac{\nabla n_e}{n_e}$ has been used to obtain a similar form in the ∇n_e coefficient.

$$\nabla^2 n_e + \left(\frac{\nabla(\sigma T_e)}{\sigma T_e} - \frac{\nabla n_e}{n_e}\right) \cdot \nabla n_e + \frac{1}{\sigma T_e} \nabla \cdot \left[\sigma\left(\nabla T_e - \frac{e}{k_B}\nabla\phi\right)\right] n_e = 0 \qquad (4.32)$$

This form is more complicated than the differential equation for potential. One particular issue is that the ∇n_e coefficient is non-linear. There are no source terms in this arrangement, but that is not a significant advantage.

The perceived benefit of the Poisson-consistent model is that the electrostatic Poisson equation can be solved for plasma potential. This avoids the poor resolution issue in the non-neutral model, since the ion and electron densities are of the same order and contribute to a source term in the differential equation for plasma potential.

This formulation also precludes the problems with statistical scatter and boundary conditions that hampered the non-neutral model. Differential equations are much more forgiving of localized statistical scatter than algebraic equations, since the integration procedure that leads to the solution acts to dissipate random variations. The PIC model ion density can be used directly in the electrostatic Poisson equation without any averaging, even with a relatively small number of particles per cell.

Unlike the non-neutral model, the differential equation for number density does not indirectly include higher order derivatives. The electrostatic Poisson equation relates the Laplacian of plasma potential to the electron number density, so at worst the differential equation for number density has additional non-linearity in its coefficients. Standard second order accurate boundary conditions are sufficient for this model.

The Poisson-consistent model is used for the first time in this work. Although the non-linearity in this model initially presented a significant obstacle, the problem was overcome by assuming constant coefficients during each solution of the differential equation. In the next chapter it will be shown that the Poisson-consistent detailed model accurately captures the features of the electrostatic sheath.

4.2.5 Summary of the electron fluid model equations

It is convenient to have the various equations for each fluid model organized in the side-by-side comparison of Table 4.1. The iteration procedure is also more readily apparent in this form.

Table 4.1: Summary of electron fluid model equations

	Boltzmann	Non-neutral	Poisson-consistent
Continuity	Eq. 4.23$\longrightarrow \Psi$, $\mathbf{v}_e$	Eq. 4.23$\longrightarrow \Psi$, $\mathbf{v}_e$	Eq. 4.23$\longrightarrow \Psi$, $\mathbf{v}_e$
Current	Eq. 4.27$\longrightarrow n_e$	Eq. 4.30$\longrightarrow \phi$	Eq. 4.32$\longrightarrow n_e$
Poisson	Eq. 4.21$\longrightarrow \phi$	Eq. 4.31$\longrightarrow n_e$	Eq. 4.21$\longrightarrow \phi$
Temperature	Isothermal	Eq. 4.25$\longrightarrow T_e$	Eq. 4.25$\longrightarrow T_e$

4.3 Hybrid fluid PIC model iteration cycle

Since the PIC, DSMC, and fluid models have been decoupled over different time scales, the models can be solved iteratively. The cycle for an iteration weights particle density to the grid first, so that the electron fluid equations can be solved for the present ion particle distribution. All of the electron fluid equations are solved next, which involves a subcycle iteration for the coupled momentum and energy equations. The new potential field is used to update the electric fields. The ions are then accelerated according to the new electric fields, moved, collided, and sampled. The whole cycle is given here:

1. Weight particle density to the nodes of the grid
2. Solve electron continuity equation on grid nodes
3. Solve electron momentum equation on grid nodes
4. Solve electron energy equation on grid nodes
5. Repeat steps 3-4 to converge coupled equations
6. Weight electric fields from grid nodes to particles

7. Move particles in the grid cells
8. Collide PIC particles in grid cells
9. Sample particle properties on the grid

These steps do not necessarily have to be performed every time step, since the models are decoupled over different time scales. The cell spacing and the time step are determined in the next chapter based on the stability requirements for the electron fluid model. The ion particles do not move very far during a single time step, and require several iterations to cross a computational cell. In order to accelerate the overall convergence, the ions are moved several times between each solution of the electron fluid model equations.

4.4 Discretization and ADI solver

The fluid equations in the preceding sections are developed as continuous functions. In order to solve these equations on the nodes of a computational grid, the equations must be expressed using discrete operators. A finite difference form offers computational advantages and simplifications for the axisymmetric, structured, rectangular grid used in this work.

4.4.1 Finite difference operators

Consider the typical node in an axisymmetric computational grid. The central node has indices (i, j), and the adjacent nodes have indices of $(i \pm 1, j)$ and $(i, j \pm 1)$ as in Fig. 4.1. Values of the variables, including any spatial derivatives, are computed and stored at the nodes.

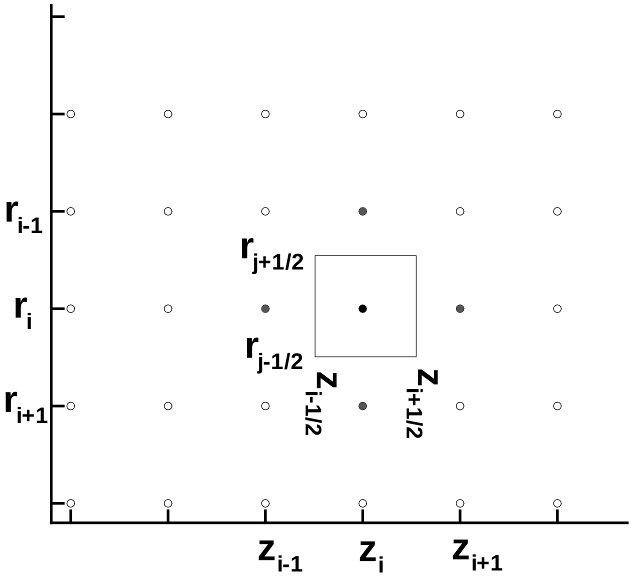

Figure 4.1: A typical computational node and its surroundings.

In order to discretize the fluid equations, the gradient operator ∇ and the Laplacian operator ∇^2 are needed. The gradient operator can be obtained in a second order accurate form by taking the Taylor expansion of an arbitrary quantity Q about the central node at (i, j). This results in the finite difference form in Eq. 4.33. Note that under the axisymmetric assumption there is no azimuthal variation, so the $\hat{\theta}$ contributions to the operator are identically zero. The constant subscript has been omitted for clarity, so $Q_{i+1,j}$ is denoted as Q_{i+1}.

$$\nabla Q = \frac{Q_{i+1} - Q_{i-1}}{x_{i+1} - x_{i-1}}\hat{z} + \frac{Q_{j+1} - Q_{j-1}}{r_{j+1} - r_{j-1}}\hat{r} \tag{4.33}$$

As given in Eq. 4.34, the Laplacian operator can be related to the gradient operator by Green's first identity. This identity states that the integral of $\nabla^2 Q$ over a volume V is equal to the surface integral of ∇Q normal to the surface S that encloses the volume.

$$\iiint_V \nabla^2 Q dV = \oint_S \nabla Q \cdot \hat{n} dS \tag{4.34}$$

For the axisymmetric geometry, the volume associated with a node is an annular cylinder. The bounding surface consists of four surfaces: two annular surfaces in the $\hat{r} - \hat{\theta}$ plane to the left and right of the node, and two cylindrical surfaces at constant radius above and below the node. As depicted in Fig. 4.1, these surfaces lie halfway between adjacent nodes.

The desired finite difference form of $\nabla^2 Q$ is a constant value stored at the node, so the volume integral reduces to the product on the left hand side of Eq. 4.35. Assuming that the finite difference form of ∇Q is also constant over each bounding surface, the surface integral can likewise be reduced to a summation over the four bounding surfaces.

$$V\nabla^2 Q = \sum_{\mathbf{A}} \nabla Q \cdot \mathbf{A} \tag{4.35}$$

The right hand side can be expanded and simplified for the simple bounding surfaces, resulting in the compact form of Eq. 4.36. The areas and the partial finite difference differentials are defined in Table 4.2. Note that the surface coordinates require slight modification for nodes along boundaries. The relevant coordinate of the center node should be used when an adjacent node does not exist (along edges of the domain) or lies on a solid surface (along edges of the probe).

$$\nabla^2 Q = \frac{dQ}{dx}_{i+\frac{1}{2}} \frac{A_R}{V} - \frac{dQ}{dx}_{i-\frac{1}{2}} \frac{A_L}{V} + \frac{dQ}{dr}_{j+\frac{1}{2}} \frac{A_o}{V} - \frac{dQ}{dr}_{j-\frac{1}{2}} \frac{A_i}{V} \tag{4.36}$$

Table 4.2: Areas and differentials in the finite difference Laplacian operator

Left annulus	$A_L = \pi\left(r^2_{j+\frac{1}{2}} - r^2_{j-\frac{1}{2}}\right)$	$\frac{dQ}{dx}_{i-\frac{1}{2}} = \frac{Q_i - Q_{i-1}}{x_i - x_{i-1}}$
Right annulus	$A_R = \pi\left(r^2_{j+\frac{1}{2}} - r^2_{j-\frac{1}{2}}\right)$	$\frac{dQ}{dx}_{i+\frac{1}{2}} = \frac{Q_{i+1} - Q_i}{x_{i+1} - x_i}$
Inner cylinder	$A_I = 2\pi r_{j-\frac{1}{2}}\left(x_{i+\frac{1}{2}} - x_{i-\frac{1}{2}}\right)$	$\frac{dQ}{dr}_{j-\frac{1}{2}} = \frac{Q_j - Q_{j-1}}{r_j - r_{j-1}}$
Outer cylinder	$A_O = 2\pi r_{j+\frac{1}{2}}\left(x_{i+\frac{1}{2}} - x_{i-\frac{1}{2}}\right)$	$\frac{dQ}{dr}_{j+\frac{1}{2}} = \frac{Q_{j+1} - Q_j}{r_{j+1} - r_j}$
Volume	$V = \pi\left(r^2_{j+\frac{1}{2}} - r^2_{j-\frac{1}{2}}\right)\left(x_{i+\frac{1}{2}} - x_{i-\frac{1}{2}}\right)$	
Coordinates	$x_{i-\frac{1}{2}} = \frac{1}{2}\left(x_{i-1} + x_i\right)$	$x_{i+\frac{1}{2}} = \frac{1}{2}\left(x_i + x_{i+1}\right)$
	$r_{j-\frac{1}{2}} = \frac{1}{2}\left(r_{j-1} + r_j\right)$	$r_{j+\frac{1}{2}} = \frac{1}{2}\left(r_j + r_{j+1}\right)$

After inserting the forms from Table 4.2 into Eq. 4.36 and simplifying, the finite difference form of the Laplacian operator can be written in the unwieldy form of Eq. 4.37.

$$\begin{aligned} \nabla^2 Q \quad = \quad & \frac{Q_{i+1} - Q_i}{\left(x_{i+1} - x_i\right)\left(x_{i+\frac{1}{2}} - x_{i-\frac{1}{2}}\right)} - \frac{Q_i - Q_{i-1}}{\left(x_i - x_{i-1}\right)\left(x_{i+\frac{1}{2}} - x_{i-\frac{1}{2}}\right)} \\ & + \frac{2r_{j+\frac{1}{2}}\left(Q_{j+1} - Q_j\right)}{\left(r_{j+1} - r_j\right)\left(r^2_{j+\frac{1}{2}} - r^2_{j-\frac{1}{2}}\right)} - \frac{2r_{j-\frac{1}{2}}\left(Q_j - Q_{j-1}\right)}{\left(r_j - r_{j-1}\right)\left(r^2_{j+\frac{1}{2}} - r^2_{j-\frac{1}{2}}\right)} \end{aligned} \tag{4.37}$$

This can be written in the compact form of Eq. 4.38 by using the coefficients defined in Table 4.3.

$$\nabla^2 Q = C_R Q_{i+1} + C_L Q_{i-1} + C_O Q_{j+1} + C_I Q_{j-1} + C_C Q \tag{4.38}$$

Table 4.3: Finite difference Laplacian coefficients

Left node	$C_L = \frac{1}{\left(x_i - x_{i-1}\right)\left(x_{i+\frac{1}{2}} - x_{i-\frac{1}{2}}\right)}$
Right node	$C_R = \frac{1}{\left(x_{i+1} - x_i\right)\left(x_{i+\frac{1}{2}} - x_{i-\frac{1}{2}}\right)}$
Inner radial node	$C_I = \frac{2r_{j-\frac{1}{2}}}{\left(r_j - r_{j-1}\right)\left(r^2_{j+\frac{1}{2}} - r^2_{j-\frac{1}{2}}\right)}$
Outer radial node	$C_O = \frac{2r_{j+\frac{1}{2}}}{\left(r_{j+1} - r_j\right)\left(r^2_{j+\frac{1}{2}} - r^2_{j-\frac{1}{2}}\right)}$
Center node	$C_c = -\left(C_R + C_L + C_I + C_O\right)$

The finite difference operators for the gradient, Eq. 4.33, and the Laplacian, Eq. 4.38, can be used to formulate the discrete electron fluid equations on the axisymmetric computational grid. The next task is to obtain a solution to the differential equations.

4.4.2 Solution technique for differential equations

Each of the differential equations that appear in the electron fluid models can be rearranged to the form $F\left(Q\right) = 0$, where Q is the independent variable that is being solved, and $F(Q)$ is the rearranged finite difference form of the differential equation. By analogy, the solution is the flow field value of Q that corresponds to a "root" of $F(Q)$.

This type of differential equation can be solved using a Newton-Raphson iteration scheme. The Newton-Raphson method treats the problem essentially as a root finding exercise in an arbitrary number of dimensions. The iterative equation in Eq. 4.39 resembles a Taylor expansion for the current value of the flow field variable Q_t near the desired solution. The desired outcome from this calculation is an updated value of the flow field variable Q_{t+1} that satisfies $F\left(Q_{t+1}\right) = 0$.

$$Q_{t+1} = Q_t - F\left(Q_t\right)\left(\frac{dF}{dQ}_t\right)^{-1} \tag{4.39}$$

Rearranging this to be more compatible with the linear form $A\boldsymbol{x} = \mathbf{b}$ yields the iteration rule in Eq. 4.40. The solution of this equation gives the quantity $\delta Q = \left(Q_{t+1} - Q_t\right)$, which is a correction to the current flow field Q_t. Many numerical techniques are available to solve linear equations in this form.

$$\frac{dF}{dQ}_t\left(\delta Q\right) = -F\left(Q_t\right) \tag{4.40}$$

The greatest challenge in using Newton-Raphson iteration stems from determining the iterative differential $\frac{dF}{dQ}_t$. Provided that the operators in the differential equation are linear, the differential and operator order can be interchanged and the iterative differential can be found easily.

As a simple example, consider Eq. 4.23, the continuity equation that is solved in all three fluid models. The stream function is the independent variable, so $Q = \Psi$ and $F(\Psi)$ is simply the continuity equation, as in Eq. 4.41. Since the Laplacian operator is a linear operator, the order of the operations can be interchanged as in the intermediate relations of Eq. 4.42. This result can be then inserted into Eq. 4.40 as an operator on $\delta\Psi$ to obtain the iteration rule for the continuity equation in Eq. 4.43. Note that the subscript t is omitted except where required for clarity.

$$F(\Psi) = \nabla^2\Psi = 0 \tag{4.41}$$

$$\frac{dF}{d\Psi} = \frac{d}{d\Psi}\left(\nabla^2\Psi\right) = \nabla^2\left(\frac{d}{d\Psi}\Psi\right) = \nabla^2 \tag{4.42}$$

$$\nabla^2(\delta\Psi) = -\nabla^2\Psi_t \tag{4.43}$$

The temperature equation of Eq. 4.25 provides a second example. The number density, potential, and velocity are held constant during the iteration for temperature, so the source term and coefficients can be replaced by constants as in Eq. 4.44. Interchanging the order of operations leads to Eq. 4.45 for the iterative differential for temperature. The source term had no temperature dependence, and does not appear in the iterative differential.

$$F(T_e) = \nabla^2 T_e + c_1 \cdot \nabla T_e - c_2 T_e - c_3 = 0 \tag{4.44}$$

$$\frac{dF}{dT_e} = \nabla^2 + c_1 \cdot \nabla - c_2 \tag{4.45}$$

The differential equation for plasma potential in the non-neutral detailed model, Eq. 4.30, can be handled in the same fashion. Number density, velocity, and temperature are constant during iteration for potential, leading to the constant coefficient form in Eq. 4.46. That form readily produces the iterative differential in Eq. 4.47.

$$F\left(\phi\right) = \nabla^2\phi + c_1 \cdot \nabla\phi - c_2 = 0 \tag{4.46}$$

$$\frac{dF}{d\phi} = \nabla^2 + c_1 \cdot \nabla \tag{4.47}$$

If the form of the differential equation is non-linear, it is more difficult to find the iterative differential. Consider the electrostatic Poisson equation for the Boltzmann model in Eq. 4.48, where the electron density has been expressed according to the Boltzmann relation with $\phi_0 = 0$ for simplicity. The first two terms can be handled as in the previous examples.

The derivative must be taken of the exponential of the potential in the third term. This produces a differential iterator that has some dependence on the current value of ϕ_t. The differential iterator and the corresponding iteration rule are shown respectively in Eqs. 4.49 and 4.50.

$$F\left(\phi\right) = \nabla^2\phi + \frac{e}{\varepsilon_0}n_i - \frac{e}{\varepsilon_0}n_{e0}\exp\left(\frac{e\phi}{k_B T_e}\right) = 0 \tag{4.48}$$

$$\frac{dF}{d\phi} = \nabla^2 - \frac{e^2 n_{e0}}{\varepsilon_0 k_B T_e}\exp\left(\frac{e\phi}{k_B T_e}\right) \tag{4.49}$$

$$\nabla^2\delta\phi - \frac{\delta\phi}{\lambda_D^2}\exp\left(\frac{e\phi_t}{k_B T_e}\right) = \nabla^2\phi_t + \frac{e}{\varepsilon_0}\left[n_i - n_{e0}\exp\left(\frac{e\phi_t}{k_B T_e}\right)\right] \tag{4.50}$$

The final equation is also the most difficult to evaluate. The differential equation for electron number density in the electrostatic Poisson equation has a non-linear coefficient on the ∇n_e term. The other coefficients can be replaced with constants as in Eq. 4.51, since the velocity, temperature, and potential are held constant during the solution for number density.

$$F\left(n_e\right) = \nabla^2 n_e + \left(c_1 - \frac{\nabla n_e}{n_e}\right) \cdot \nabla n_e + c_2 n_e = 0 \tag{4.51}$$

The iterative differential is straightforward except for the non-linear term:

$$\frac{d}{dn_e}\left(-\frac{\nabla n_e}{n_e}\cdot\nabla n_e\right)$$

This expression can be evaluated in a number of different ways, but not every evaluation leads to a stable iteration rule. In fact the best computational performance is obtained by calculating the coefficient once, and then leaving it as a constant for the rest of the iteration. Under that assumption, the function and iterative differential are simple linear operators as seen in Eqs. 4.52 and 4.53.

$$F\left(n_e\right)=\nabla^2 n_e+c_1\cdot\nabla n_e+c_2 n_e=0 \tag{4.52}$$

$$\frac{dF}{dn_e}=\nabla^2+c_1\cdot\nabla+c_2 \tag{4.53}$$

It should be noted that all of the results in this section are valid for both continuous and discrete operators. The finite difference operators from Sec. 4.4.1 can substituted into these expressions without any modification.

4.4.3 ADI solver

The iteration rules from the preceding discussion (such as Eq. 4.43 or Eq. 4.50) take the form of banded diagonal matrices when expressed using the finite difference operators of Sec. 4.4.1. Numerical techniques including the Alternating Direction Implicit (ADI) method [50, 74] have been developed to solve these types of linear equations.

Banded diagonal matrices are significantly more difficult to solve than tridiagonal matrices. However, an approximate solution can be obtained by neglecting the terms in the bands and solving just the tridiagonal system. For the differential equations in the fluid models, this process is equivalent to solving the differential equations along just one direction. A consistent solution can be obtained by solving the equations alternately for rows and columns.

This work uses a standard implementation of the ADI method to solve the differential equations that appear in the electron fluid models. The solution technique is well known, and details can be found in most numerical and programming handbooks [75].

4.5 ADI accuracy and stability for the detailed models

The complicated differential equations that appear in the detailed models are not well understood, and have not been evaluated in terms of well-posedness or uniqueness. At the outset it is not certain that the ADI solver will be able to solve the equations and obtain a stable, physically meaningful solution.

Inspection of the equations, particularly the forms in Eq. 4.46 and Eq. 4.52, reveals a strong similarity to one dimensional differential equations with analytic solutions. Therefore the difficult equations from the non-neutral and Poisson-consistent detailed models are solved analytically in one dimensional limits with constant coefficients.

As a test of the ADI solver, the differential equations are also solved on a domain consisting of a single row. The ADI solver performance will be evaluated by comparing the accuracy of those solutions against the exact analytic solutions. Challenging conditions are tested to verify that the ADI solver can handle difficult solutions that include oscillations or unbounded behavior.

4.5.1 One dimensional non-neutral detailed model

The differential equation for potential from the non-neutral model, Eq. 4.46, can be rewritten in the form of Eq. 4.54. In this form the source term is represented by a forcing function f, and the coefficient is denoted as $\boldsymbol{\alpha}$ to distinguish it from constants of integration later. The analytic solution is more readily apparent if the equation is cast in terms of the electric field as in Eq. 4.55, using the usual electrostatic relation.

$$\nabla^2 \phi + \boldsymbol{\alpha} \cdot \nabla \phi = f \tag{4.54}$$

$$\nabla \mathbf{E} + \boldsymbol{\alpha} \cdot \mathbf{E} = -f \tag{4.55}$$

In the limit of one dimensional flow, this simplifies to the non-homogeneous constant coefficient differential equation of Eq. 4.56. Note that this equation is essentially an initial value problem with the x coordinate acting as the time variable.

$$\frac{dE_x}{dx} + \alpha E_x = -f \tag{4.56}$$

The solution has the general form of Eq. 4.57, where the non-homogeneous solution is a constant value c_2. Assuming an "initial" condition $E_x(0) = E_w$ and a "steady state" condition $E_x(x \longrightarrow \infty) = E_\infty$ allows the constants of integration to be determined.

$$E_x = c_1 \exp\left(-\alpha x\right) + c_2 \tag{4.57}$$

$$c_1 = \left(E_w - E_\infty\right),\ c_2 = E_\infty$$

The potential can then be found by integrating the electric field as in Eq. 4.58, since $E_x = -\frac{d\phi}{dx}$ in one dimension.

$$\phi\left(x\right) = -\int E_x dx = -\int \left(E_w - E_\infty\right) \exp\left(-\alpha x\right) + E_\infty dx \tag{4.58}$$

The integration is straightforward and produces the form in Eq. 4.59. An initial condition on the potential is $\phi\left(0\right) = \phi_w$,which allows the last constant of integration to be determined.

$$\phi\left(x\right) = \frac{1}{\alpha}\left(E_w - E_\infty\right) \exp\left(-\alpha x\right) - E_\infty x + c_3 \tag{4.59}$$

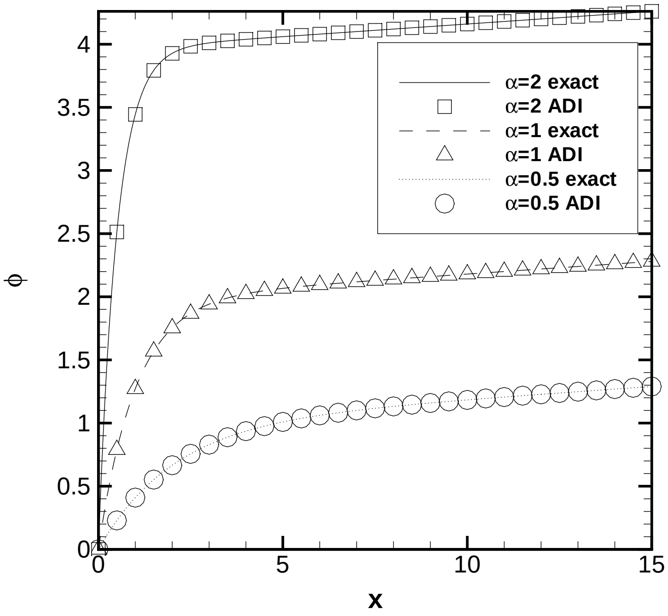

Figure 4.2: ADI solutions of the 1D non-neutral model potential equation

$$c_3 = \phi_w - \frac{1}{\alpha}\left(E_w - E_\infty\right)$$

Inserting the constant and rearranging produces the final form of the solution in Eq. 4.60.

$$\phi\left(x\right) = \frac{1}{\alpha}\left(E_w - E_\infty\right)\left[\exp\left(-\alpha x\right) - 1\right] - E_\infty x + \phi_w \tag{4.60}$$

The magnitude of the coefficient α determines the overall nature of the solution. The two limiting cases are a predominantly linear solution when $\alpha \gg (E_w - E_\infty)$, or a predominantly exponential solution when $\alpha \ll 1$. For intermediate values of α, the solution will appear exponential at small values of x but level off and appear linear at large values of x.

The ADI results are compared with exact solutions in Fig. 4.2 for the conditions $E_w = -2$, $E_\infty = -0.02$, and $\phi_w = 0$ over a range of α values. The effect of the α coefficient on the solution is clearly visible. The ADI solver reproduces the exact solutions to within machine precision in every case.

4.5.2 One dimensional Poisson-consistent model

The differential equation for number density from the Poisson-consistent model, Eq. 4.32, can be rewritten with constant coefficients $\boldsymbol{\alpha}$ and β as Eq. 4.61.

$$\nabla^2 n_e + \boldsymbol{\alpha} \cdot \nabla n_e + \beta n_e = 0 \tag{4.61}$$

In the limit of one dimensional flow, this simplifies to the homogeneous constant coefficient differential equation of Eq. 4.62. Note that this equation has exactly the same form as a damped harmonic oscillator problem with the x coordinate acting as the time variable.

$$\frac{d^2 n_e}{dx^2} + \alpha \frac{dn_e}{dx} + \beta n_e = 0 \tag{4.62}$$

This has an analytic solution [76] that can be underdamped ($\zeta < 1$), critically damped ($\zeta = 1$), or overdamped ($\zeta > 1$), depending on the relative magnitudes of the coefficients α and β.

$$n_e(x) = \exp(-\zeta\omega x) \begin{cases} \sqrt{n_{e0}^2 + \theta_{ud}^2} \sin\left(\omega\sqrt{1-\zeta^2}x + \arctan\left(\frac{n_{e0}}{\theta_{ud}}\right)\right) & 0 < \zeta < 1 \\ n_{e0} + (dn_{e0} + \omega n_{e0})\, x & \zeta = 1 \\ \frac{1}{2}(n_{e0} - \theta_{od}) \exp\left(-\omega\sqrt{\zeta^2 - 1}x\right) & \\ \quad + \frac{1}{2}(n_{e0} + \theta_{od}) \exp\left(\omega\sqrt{\zeta^2 - 1}x\right) & \zeta > 1 \end{cases} \tag{4.63}$$

$$\omega = \sqrt{\beta},\ \zeta = \frac{\alpha}{2\omega},\ \theta_{ud} = \frac{dn_{e0} + \zeta\omega n_{e0}}{\omega\sqrt{1-\zeta^2}},\ \theta_{od} = \frac{dn_{e0} + \zeta\omega n_{e0}}{\omega\sqrt{\zeta^2 - 1}}$$

The ADI results are compared with exact solutions in Fig. 4.3 for the conditions $n_{e0} = 5$, $dn_{e0} = 3$, and $\omega = 1$ over a range of ζ values. The ADI solver performs excellently, and reproduces the exact solutions to within machine precision.

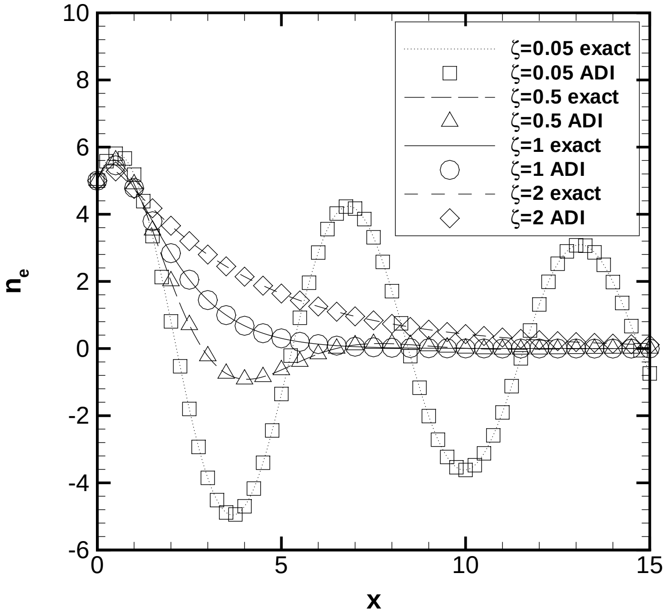

Figure 4.3: ADI solutions of the 1D Poisson-consistent model number density equation

In the Poisson-consistent model, the coefficient $\boldsymbol{\alpha}$ is non-linear. This is beyond the capabilities of the simple analytic solution that is available, so the ADI solver is not tested against that case. The cases shown are certainly not exhaustive. It is possible that the ADI solver may become unstable or inaccurate for other untested conditions. However, the preceding results are very promising and indicate that the ADI solver is capable of solving the complicated differential equations of the detailed models.

Chapter V

Faraday Probe Simulations

The hybrid fluid PIC model is used to simulate the flow around an axisymmetric Faraday probe geometry for a variety of inflow plasma conditions and probe operating conditions. An initial study validates the operation of the hybrid fluid PIC model by comparing its results against the planar Bohm sheath solution. Further studies change the inflowing ion distribution, add neutral gas particles, or vary the operational settings of the Faraday probe.

The Boltzmann model is used extensively to develop an understanding of the flow over a broad range of conditions. The effects of inflow plasma properties are explored by making incremental changes to the inflow ion distribution. Over several steps the distribution is modified from a cold ion beam to a complicated multiple Maxwellian ion and neutral distribution that approximates an EP exhaust plume.

Probe performance is also investigated, using the Boltzmann model in two studies that vary the operating conditions of the probe. Performance is evaluated by comparing the simulated collected current to the freestream current, and by observing streamlines of current upstream of the collecting surface.

The non-neutral detailed model is only used in a validation test, where the implementation is shown to be flawed. This model is not used for any additional simulations in this dissertation and is not developed any further, since an alternative detailed model is available.

The Poisson-consistent detailed model is used to repeat the studies of the inflow ion distribution. Since this model uses a detailed electron momentum equation and includes an electron energy equation, these studies can also be used to assess the validity of the Boltzmann relation for the electrons. Results from these studies are shown to be in excellent agreement with the Boltzmann fluid model results, provided the inflow distribution has a sufficiently small fraction of backward flowing particles.

A review of the results from all the studies leads to a few comments and recommendations for probe design and operation. The Faraday probe is predicted to be reliable and accurate over all the conditions considered. Standard practices for the design and use of Faraday probes are deemed to be effective at obtaining an accurate measurement of the ion current.

5.1 Basis for simulation

These simulations are intended to be representative of a Faraday probe at a point far off-axis in the plume of a Hall thruster. Plasma conditions are determined from complementary numerical simulations and experimental measurements of a thruster plume, made available by other researchers. The Faraday probe is described in detail in an experimental reference, and that geometry is adapted for use here.

5.1.1 Hall thruster plume properties

Busek Co. manufactures the BHT-200, a small, low power Hall thruster. The plume of this device has been investigated via experiments and numerical simulations, providing several sources [33, 35, 73, 77] to help determine the plasma conditions. The two primary sources are the numerical simulations by Boyd and Yim [73], and the experimental measurements by Ma [77].

The flow conditions at a point 50 cm downstream and 75° off-axis are determined from a previous numerical simulation by Boyd and Yim [73], and are summarized in Table 5.1. The plasma is neutral at that point, so it is assumed that $n_i = n_e$ and $v_i = v_e$ for simplicity. The exact values are not critical, and it will be convenient to modify these conditions in order to maintain a constant ion current density.

Table 5.1: Plasma properties 50 cm downstream and 75° off-axis in the BHT-200 plume.[73]

n_i	$1.1 \times 10^{14}\,\mathrm{m}^{-3}$
v_i	$2,381\,\frac{\mathrm{m}}{\mathrm{s}}$
T_e	1 eV
ϕ	$\sim 1\,\mathrm{V}$

For the reported conditions, the Debye length is $\lambda_D = 0.0709\,\mathrm{cm}$ and the Bohm velocity is $v_B = 855\,\frac{\mathrm{m}}{\mathrm{s}}$, giving a Mach number with respect to Bohm velocity of $M = 2.78$. This corresponds to a stable Bohm sheath solution. Additionally, all of the freestream ion current should reach the front surface of the probe, since the probe will be biased to negative potential for all the simulations in this dissertation.

5.1.2 Faraday probe

The Faraday probe in Ref. [77] is a nude planar probe depicted in Fig. 5.1. The circular collecting surface has a radius of 0.952 cm, and the annular guard ring has an outer radius of 1.272 cm. There is a 0.066 cm radial gap between the collecting surface and the guard ring. The gap is smaller than the Debye length for these conditions, so the sheath should remain essentially uniform over the entire collecting surface.

Figure 5.1: Faraday probe used in experimental BHT-200 measurements [77].

The collecting surface and guard ring are held at a fixed bias potential of -5 V to repel electrons. Again, the exact value of the bias potential is not important and it can be changed for convenience. Since the length of the sheath increases with the wall potential, most of the simulations use a small bias potential to reduce the domain length and computational time.

5.2 Simulation geometry and numerical parameters

The cylindrical geometry of the Faraday probe lends itself to an axisymmetric computational domain. Using the planar Bohm sheath solution as a guide, the domain can be sized and boundary conditions for the fluid and PIC models can be formulated. Computational mesh dimensions must be small enough to resolve the Debye length, and the time step must be selected such that particles do not cross multiple cells per iteration.

5.2.1 Computational domain

For the conditions in Table 5.1 and a maximum wall potential of -15 V, the Bohm sheath solution suggests $15\,\lambda_D(1.06\,\mathrm{cm})$ as an estimate of the required domain length. The appropriate radial extension beyond the side of the probe body is not easily determined, and is set at one quarter-radius beyond the outer probe edge. Since the flow is supersonic and nearly collisionless, the placement of the outer edge of the domain should not greatly affect the properties on the upstream face of the probe.

Experience with the detailed models suggests that the maximum cell spacing should be at least a factor of 12 smaller than the Debye length. Rounding in favor of conservative values, the rectangular cells are uniformly sized at 4×10^{-5} m on a side. The final geometry extends 390 cells (1.560 cm) along the probe axis and 390 cells (1.560 cm) radially, with 238 elements (0.952 cm) along the collecting surface and 80 elements (0.320 cm) along the guard ring surface. This geometry is shown in Fig. 5.2 for reference. Altogether there are 112,350 cells outside of the probe body. At steady state, there are approximately 1.5-2 million particles in the domain, depending on the inflow ion distribution.

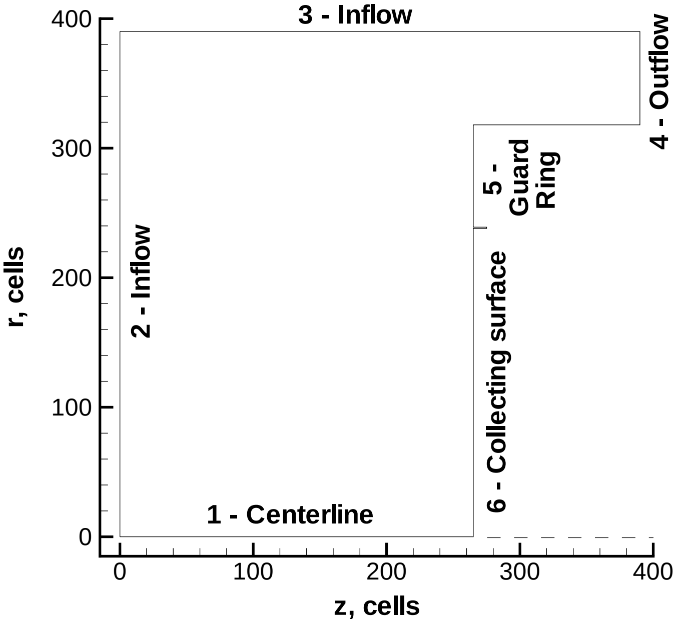

Figure 5.2: Computational domain for Faraday probe simulations.

5.2.2 Time step and global iteration

The simulation time step is selected so that the fastest ions travel less than one cell length per iteration. Ions that enter at twice the thermal speed beyond the drift velocity arrive at the probe with a velocity of $6,945\ \frac{\mathrm{m}}{\mathrm{s}}$. Dividing the cell length by this speed and rounding down sets the time step at 5×10^{-9} s.

The simulation is allowed to iterate for 10,000 time steps to reach a converged state, followed by 20,000 sampled time steps. The total simulation time is 30-35 hours, depending on the specific ion inflow distribution.

5.2.3 Boundary conditions

The PIC model and the electron fluid models require boundary conditions along all the edges of the domain and at the surfaces of the probe. Referring to the labels in Fig. 5.2, there are six regions of boundary conditions.

Region 1 is the axisymmetric centerline. Particles are automatically rotated at the centerline as part of the axisymmetric move routine. A zero gradient condition is enforced on the radial component of all variables in the fluid models, including the stream function Ψ, plasma potential, electron number density, and electron temperature.

Region 2 is the upstream inlet for the flow. Particles are introduced at this boundary with a random position and statistically sampled velocity in each cell. The number of particles introduced per time step is determined from the assigned inlet density and mean velocity, adjusted by the particle weight in the cell. Particles that cross this boundary are removed from the simulation.

The electron temperature and gradient of stream function (equivalent to the electron number density flux) are assigned along the inlet. The plasma potential and electron number density are set using Robin or third kind boundary conditions. As an example, Eq. 5.1 sets the plasma potential ϕ_1 at the boundary node based on the potential at the second node ϕ_2 that simultaneously satisfies both the assigned potential ϕ_0 and assigned axial gradient $\frac{d\phi}{dz}\big|_0$ at an imaginary node one cell length $\triangle z$ outside of the domain.

$$\phi_1 = \frac{3}{4}\phi_0 + \frac{1}{4}\phi_2 + \frac{1}{2}\left.\frac{d\phi}{dz}\right|_0 \triangle z \tag{5.1}$$

Region 3 is the outer radial inlet. Particles are injected along this edge using the same procedure as in Region 2, and particles that cross this boundary are removed from the simulation. A constant gradient condition is enforced on the radial component of the stream function, and zero gradient conditions are enforced on the radial component of plasma potential, electron number density, and electron temperature.

Region 4 is the downstream flow exit. Particles are only removed along this edge. A constant gradient condition is enforced on the stream function, and zero gradient conditions are enforced on the axial component of plasma potential, electron number density, and electron temperature.

Region 5 is the body of the probe. Particles undergo diffuse reflection from this surface with full thermal accommodation, and ion particles are neutralized. The gradient of stream function is assigned, which is equivalent to setting the electron current flux to the surface. The plasma potential, electron number density, and electron temperature are assigned at the surface.

Region 6 is the collecting surface of the probe. The same boundary conditions as in Region 5 are enforced on particles and electron fluid variables. When ion particles are neutralized at this surface, the collected current is incremented by the charge of the ion particle. This gives the simulated collected current, which is averaged over the sampling time steps.

The boundary conditions on electron number density are only required for the Poisson-consistent detailed model. Since it is not practical to solve the differential equation for n_e at the surface, a kinetic approximation to the number density is used instead. Electrons are assumed to follow a Maxwellian distribution at the inlet of the domain. Using a Lagrangian formulation for conservation of energy, the distribution function at the wall $f_w(v)$ can be related to the inlet distribution function $f(v)$ by the velocity shift in Eq. 5.2. Since the wall potential ϕ_w is negative, a given velocity at the wall corresponds to a larger velocity at the inlet.

$$f_w(v)\,dv = f\left(\sqrt{v^2 - 2\frac{e}{m}\phi_w}\right)dv \tag{5.2}$$

It is assumed that all electron particles that reach the wall are absorbed, so the distribution function is zero for $v < 0$. Integrating over the distribution function as in Eq. 5.3 gives the boundary value of electron number density at the probe surface.

$$n_{e,w} = \int_0^\infty f_w(v)\,dv \tag{5.3}$$

This is not an exact solution to the differential equation for electron number density, but it serves as an acceptable approximation for the boundary condition.

5.3 Hybrid PIC Boltzmann model studies

The Boltzmann model is used to obtain the results in five main studies here. Three studies are designed to explore the flow field by varying the geometry and inflow ion conditions. Two additional studies investigate the performance of the Faraday probe for various operating conditions.

The first study is a quasi one dimensional simulation that is used to validate the operation of the hybrid fluid PIC computational code. The second study simulates the same conditions on the two dimensional axisymmetric probe geometry to identify any higher dimensional effects. The third study is an investigation of inflow ion distribution effects, conducted by incrementally adding component distributions to the inflow plasma.

In the fourth study, the guard ring bias potential is varied relative to the collecting surface bias to determine the effective collecting area of the probe. The fifth study is a sweep over a broad range of bias voltage, to characterize the probe performance over a range of bias potentials.

5.3.1 Quasi one dimensional study

The first aspect of the quasi one dimensional study is to perform a validation of the hybrid PIC fluid code by reproducing the conditions of the planar Bohm sheath model. To that end, the computational domain is limited to a cylinder that lies immediately upstream of the collecting surface, with a new outer radial edge at $r = 0.0952\,\mathrm{cm}$.

The boundary conditions on the outer radial edge are modified to simulate a symmetry plane as follows. No particles are injected, and particles that cross the boundary are specularly reflected back into the domain. Zero gradient conditions are enforced on the stream function, plasma potential, electron number density, and electron temperature.

Since the planar Bohm sheath model assumes a cold ion beam, the ion temperature at the inlet is set to 300 K. This is much lower than the electron temperature, but still high enough to avoid the computational difficulties associated with zero temperature. All other plasma properties remain as given in Table 5.1. This condition is referred to as the cold ion case.

A radial average is taken of the hybrid fluid PIC model results in order to make useful comparisons with the Bohm sheath solution. This is accomplished by averaging the first 100 cells (0.004 m) from the centerline at a fixed axial position. The resulting profile is representative of the plasma properties near the centerline of the simulated probe.

The Boltzmann model hybrid fluid PIC results are excellent for the cold ion case. Contours and profiles of plasma potential, Figs. 5.3-5.4, electron number density, Figs. 5.5-5.6, and ion number density, Figs. 5.7-5.8, show excellent agreement with the Bohm sheath solution. The contours of each variable are normal to the axis, indicating that quasi one dimensional flow has been achieved. The profiles of simulated properties are indistinguishable from the Bohm sheath solution profiles for every property.

This level of agreement indicates that the Boltzmann model can very accurately simulate the physics underlying the formation of an electrostatic sheath. It should be noted that the electron number density is a function of the plasma potential by the Boltzmann relation. As such, the simulated electron number density is not truly an independent variable, and will show the same trends as the plasma potential.

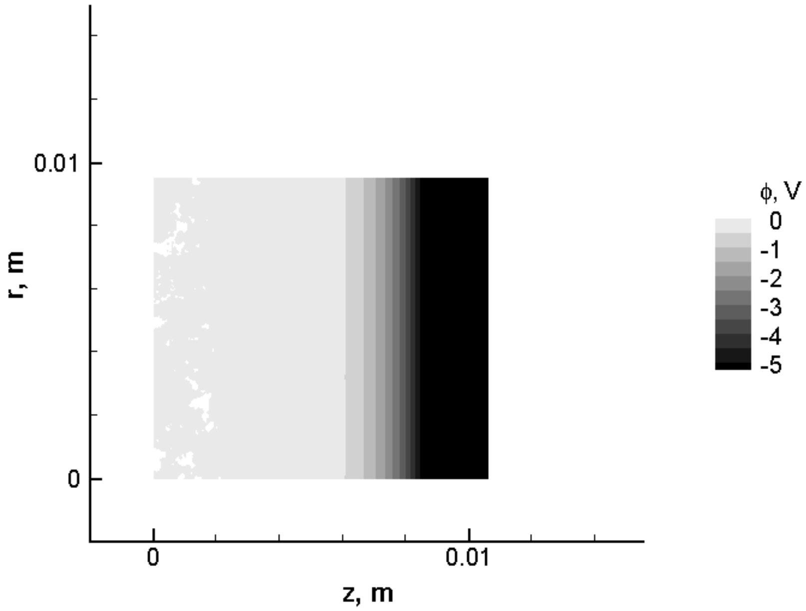

Figure 5.3: Contours of plasma potential for the one dimensional cold ion case.

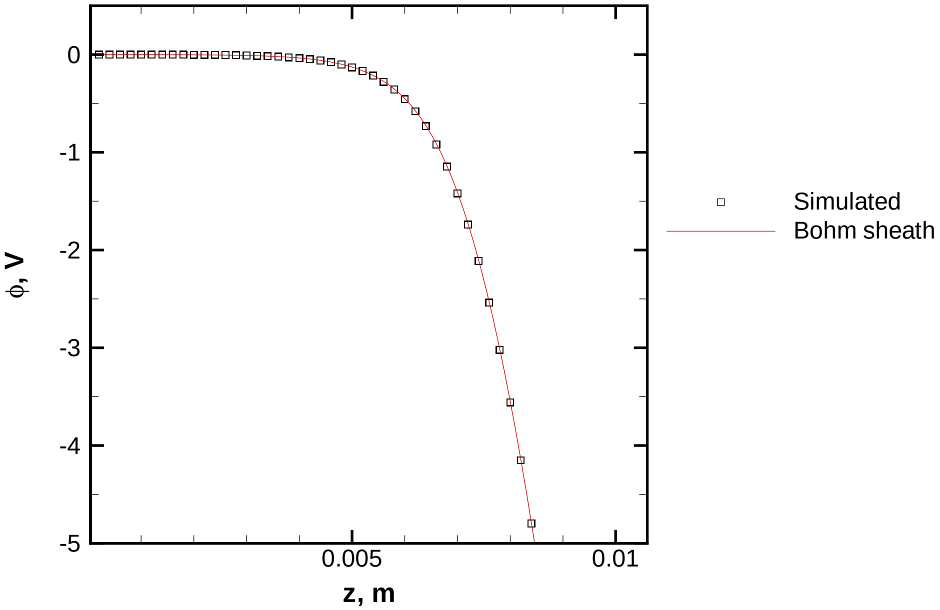

Figure 5.4: Profiles of plasma potential for the one dimensional cold ion case.

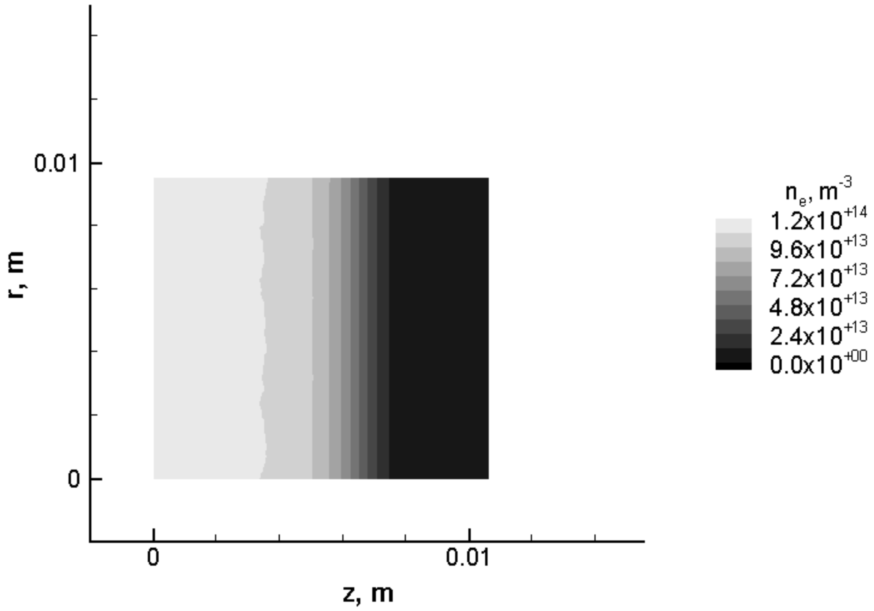

Figure 5.5: Contours of electron number density for the one dimensional cold ion case.

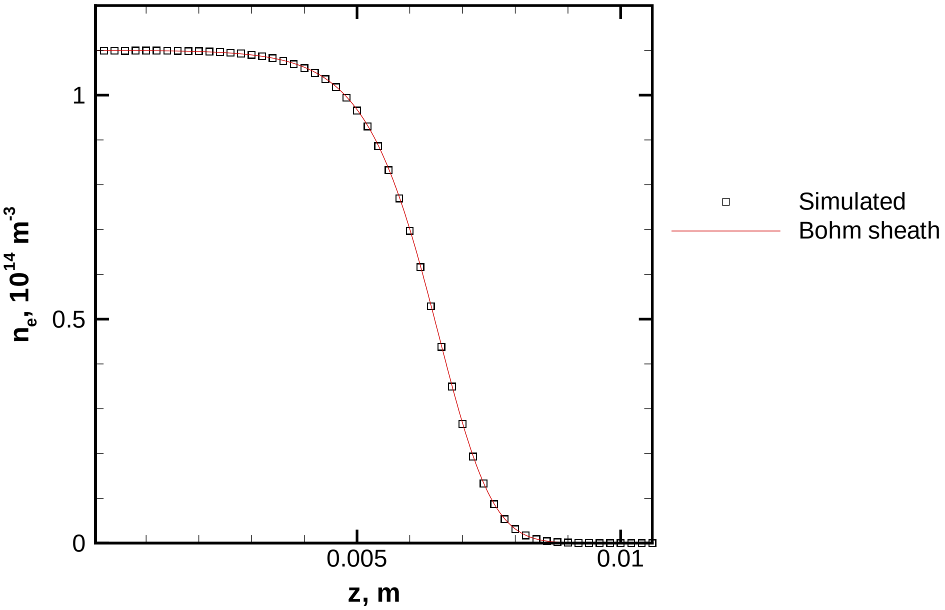

Figure 5.6: Profiles of electron number density for the one dimensional cold ion case.

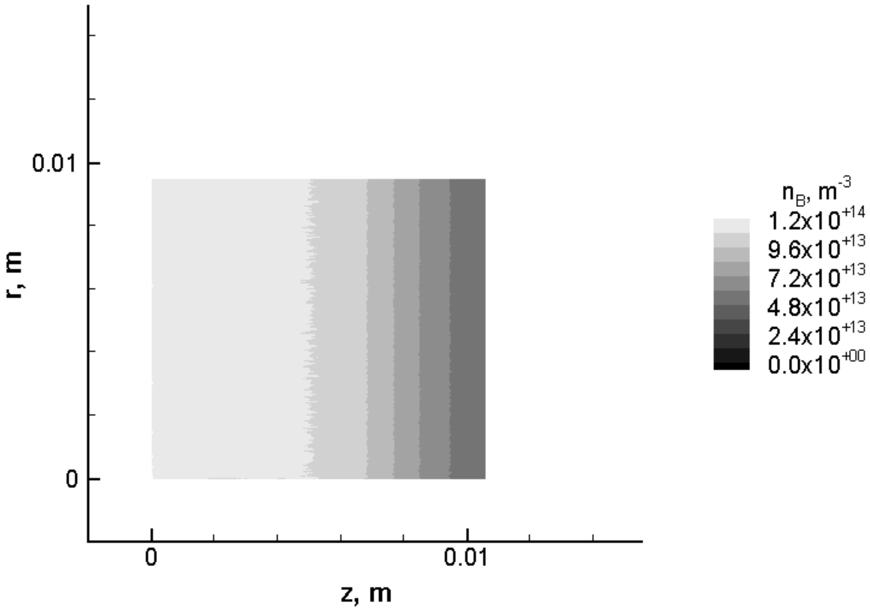

Figure 5.7: Contours of ion number density for the one dimensional cold ion case.

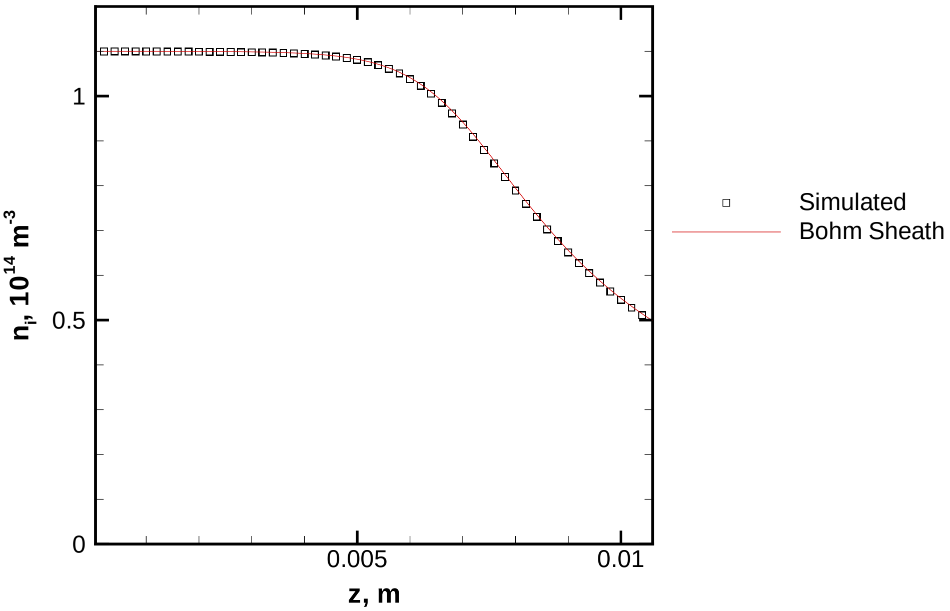

Figure 5.8: Profiles of ion number density for the one dimensional cold ion case.

The second aspect of the quasi one dimensional study is to isolate the effect of ion temperature on the properties in the sheath. The hot ion case uses an inlet ion temperature of 1 eV, along with the other conditions in Table 5.1. In this case the ion temperature is large enough that there is a significant spread in velocities about the mean velocity.

The simulations of the hot ion case maintain quasi one dimensional flow in this geometry, so the contours are omitted. The profiles of plasma potential, Fig. 5.9, and electron number density, Fig. 5.10, still show very good agreement with the Bohm sheath solution profiles. However, the ion number density, Fig. 5.11, is about 5% lower than expected through most of the sheath.

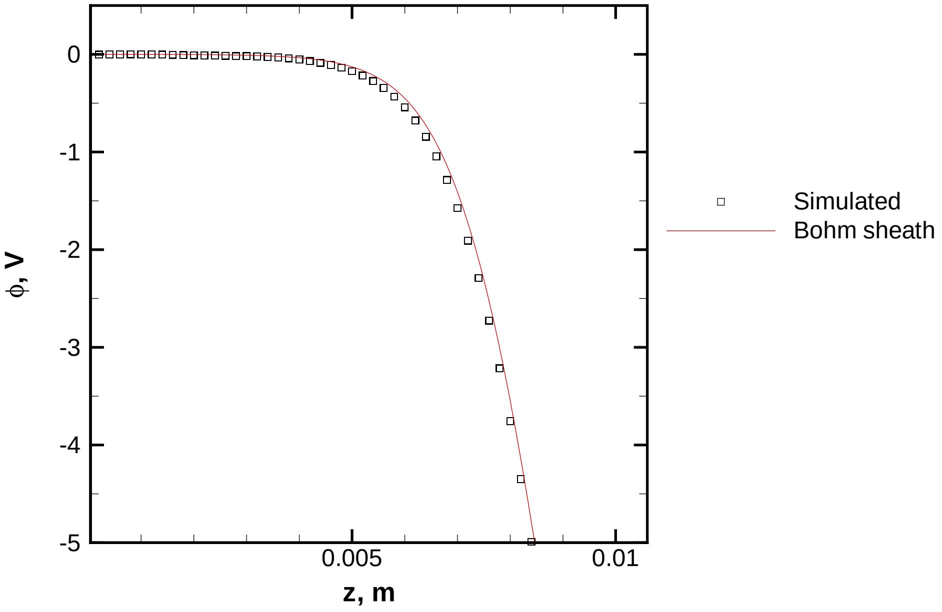

Figure 5.9: Profiles of plasma potential for the one dimensional hot ion case.

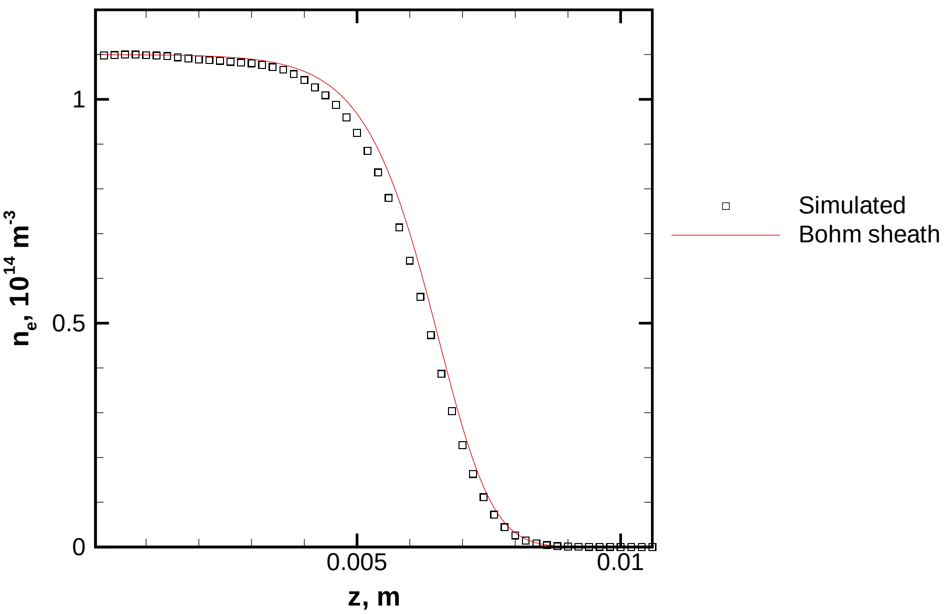

Figure 5.10: Profiles of electron number density for the one dimensional hot ion case.

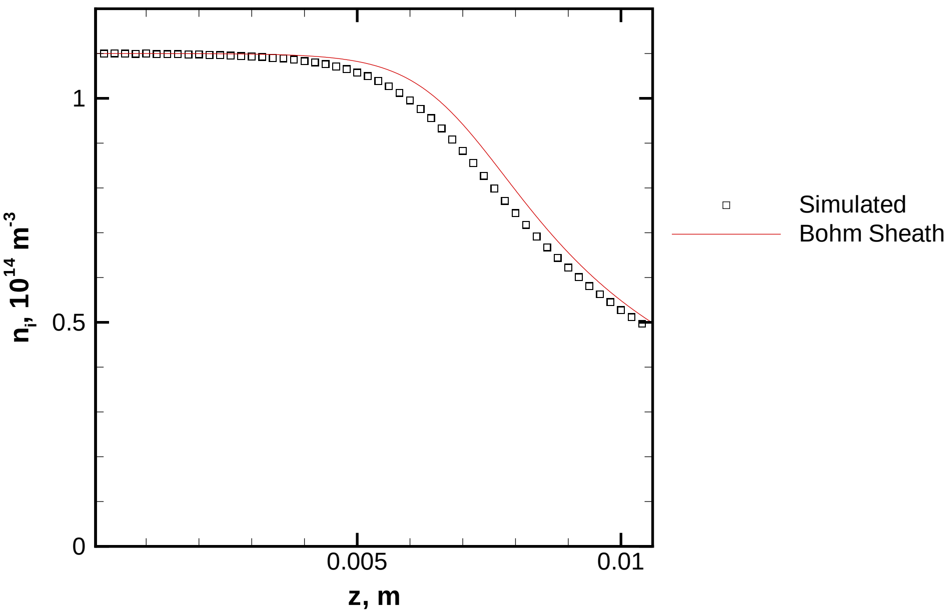

Figure 5.11: Profiles of ion number density for the one dimensional hot ion case.

This difference can be explained by the presence of low speed ions in the distribution for the hot ion case. A given difference in electrostatic potential leads to a larger increase of velocity for slow particles than for fast particles. Since the ion number density flux is constant, the density decreases as the mean velocity increases. The mean velocity will increase faster for a distribution with low speed ions than for a distribution of uniform speed ions, which results in a lower density at a corresponding plasma potential.

5.3.2 Two dimensional study

The next study using the Boltzmann model is conducted on the axisymmetric probe geometry. For the sake of easy comparison with the quasi one dimensional results, the guard ring is eliminated so that the outer diameter of the probe is at the radius of the collecting surface. The conditions of the cold ion case are simulated to reproduce the planar Bohm sheath conditions.

Contours and profiles of plasma potential, Figs. 5.12-5.13, electron number density, Figs. 5.14-5.15, and ion number density, Figs. 5.16-5.17, show excellent agreement with the Bohm sheath solution near the centerline. Edge effects are visible as strong curvature in the contours near the front corner of the probe. However, the effects are only significant for $\sim 0.0015\,\mathrm{m}$ or $2\,\lambda_D$ from the outer edge of the probe.

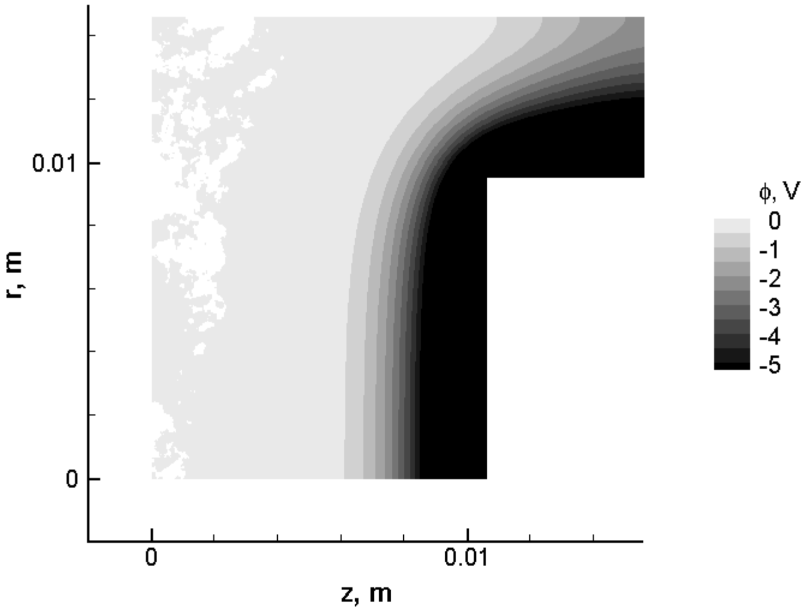

Figure 5.12: Contours of plasma potential for the cold ion case.

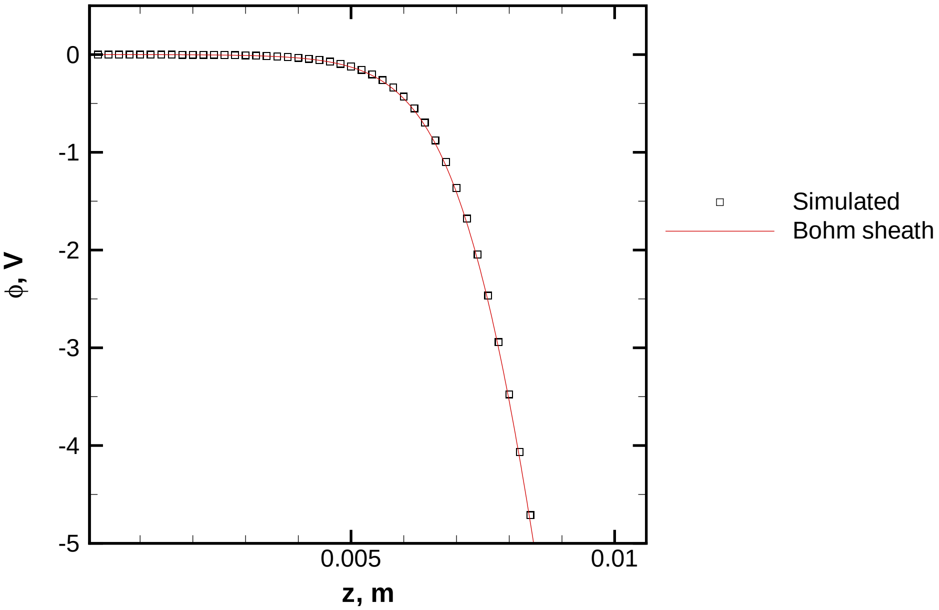

Figure 5.13: Profiles of plasma potential near the centerline for the cold ion case.

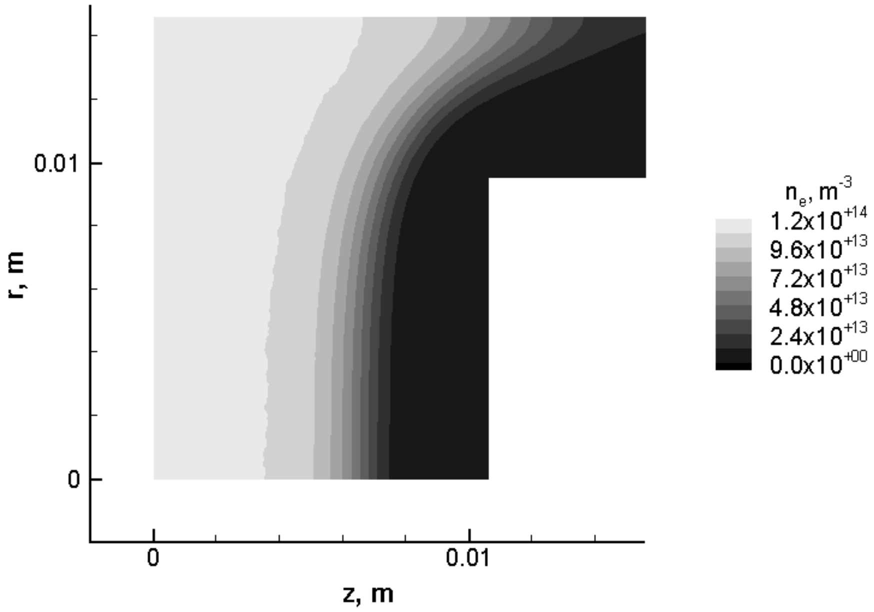

Figure 5.14: Contours of electron number density for the two dimensional cold ion case.

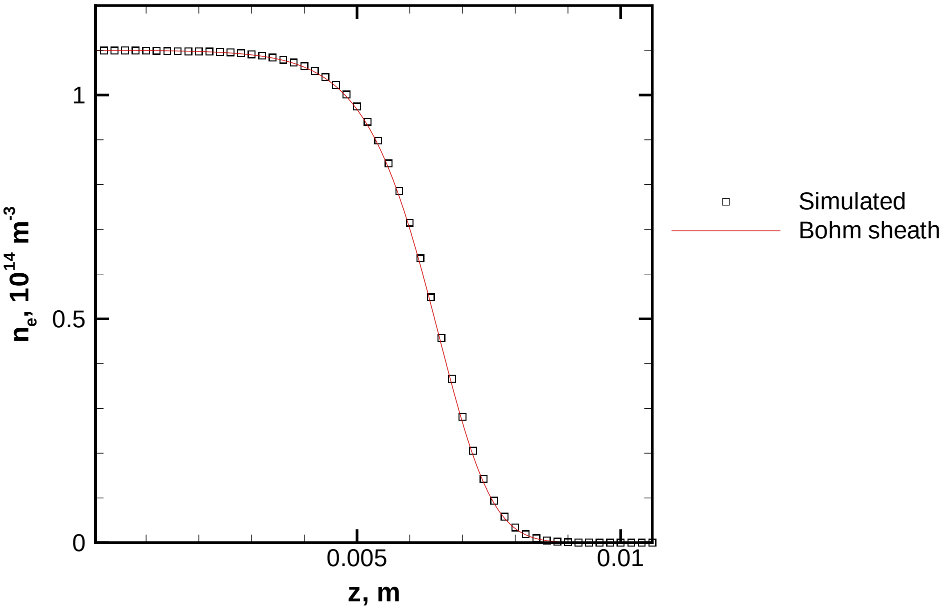

Figure 5.15: Profiles of electron number density near the centerline for the cold ion case.

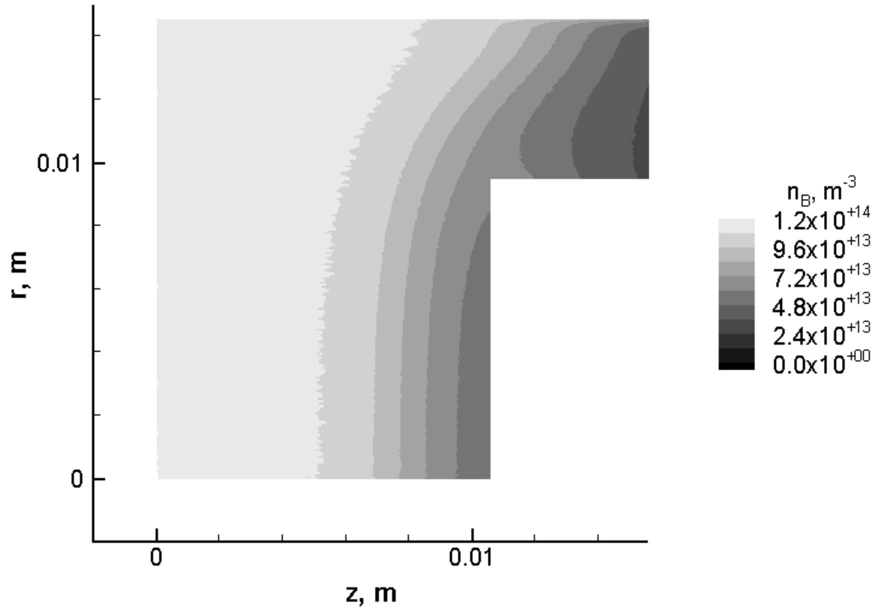

Figure 5.16: Contours of ion number density for the two dimensional cold ion case.

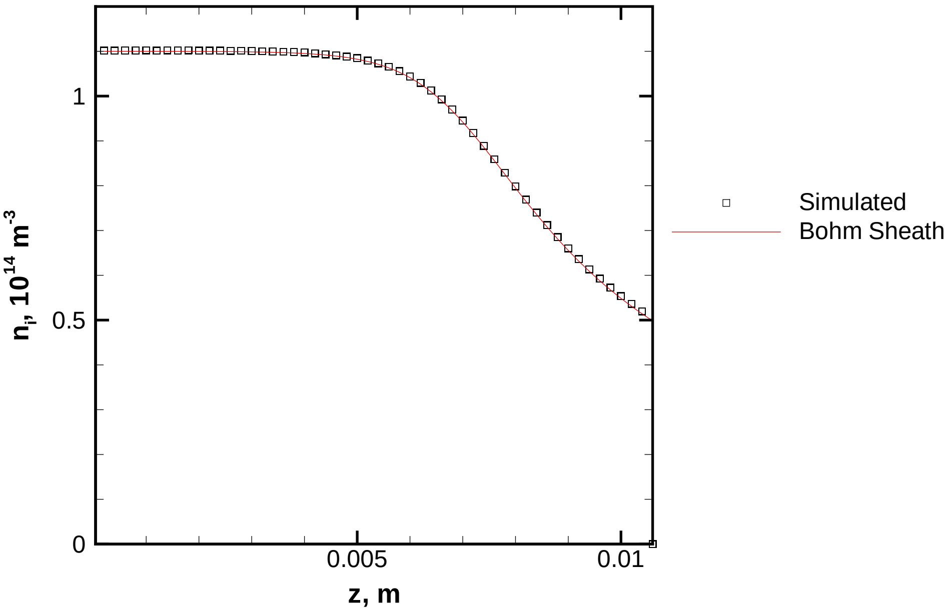

Figure 5.17: Profiles of ion number density near the centerline for the cold ion case.

The hot ion case shows very similar features on the axisymmetric probe geometry. The contours are visually indistinguishable from those of the cold ion case, so they are not shown here. The profiles of plasma potential, Fig. 5.18, electron number density, Fig. 5.19, and ion number density, Fig. 5.20, are marginally closer to the Bohm sheath solution than the hot ion case in the quasi one dimensional model.

The slight improvement is likely due to the weak focusing effect of the curved potential field. The low speed ions are still accelerated, but part of the acceleration is radial and does not affect the flux. As a consequence the ion number density stays slightly higher and attains better agreement with the Bohm sheath profile.

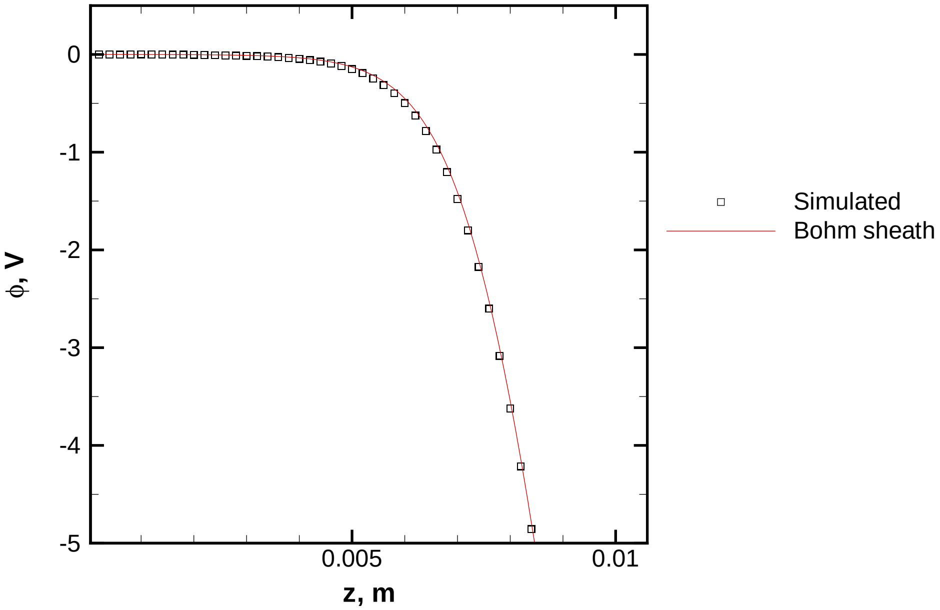

Figure 5.18: Profiles of plasma potential near the centerline for the hot ion case.

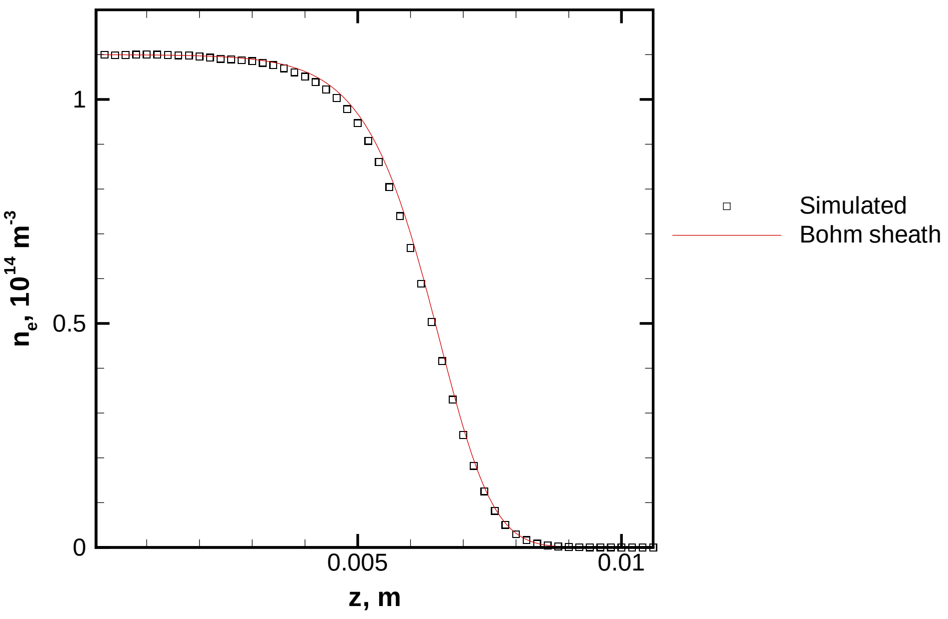

Figure 5.19: Profiles of electron number density near the centerline for the hot ion case.

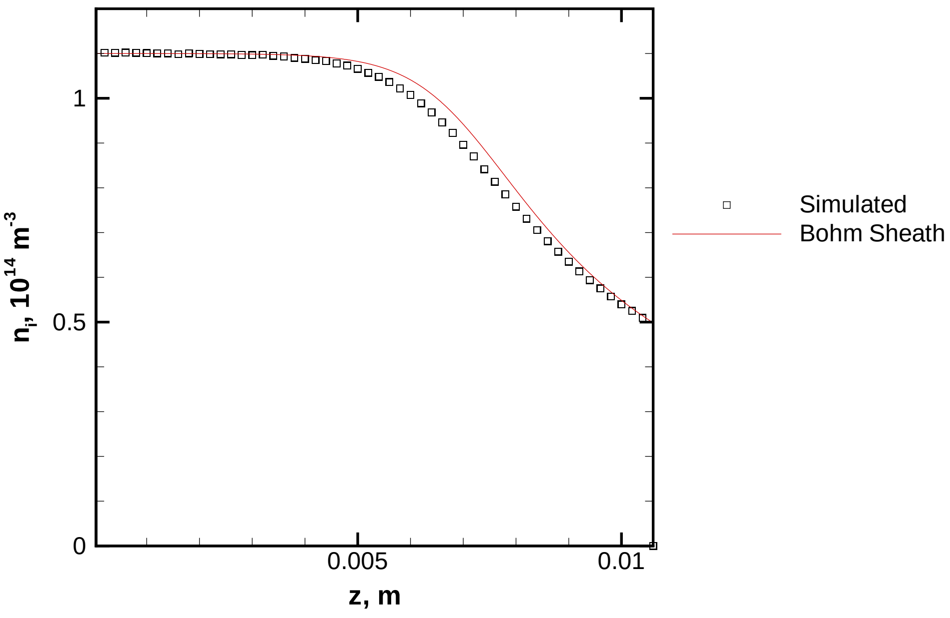

Figure 5.20: Profiles of ion number density near the centerline for the hot ion case.

5.3.3 Multiple component studies

The third study using the Boltzmann model builds a complicated inflow ion distribution by adding together several Maxwellian components. The interaction of the different component populations is evaluated by comparing the ion number density profile for one component simulated separately against the profile for the same component simulated with one or more additional components.

This is accomplished in two stages, first a combination of high speed, high temperature beam ions and low speed, low temperature charge exchange (CEX) ions is simulated. Second, a combination of beam, CEX, and double charge ions is simulated. The plasma conditions are reported in Table 5.2 for the beam-CEX case, and Table 5.3 for the beam-CEX-double composite case. In both of these cases the total freestream current density is held constant by adjusting the density of the component populations.

The number density, drift velocity, and temperature for the component distributions are selected in keeping with the assumption that the probe is placed far off-axis in a Hall thruster plume. For the sake of comparison with other results, the ion current density is held constant at the same value as in the single component cases. Experiments that compare collimated and uncollimated Faraday probe measurements suggest that CEX ions account for the majority of the current at high angles from the centerline [41]. Using a similar ratio, the CEX component is assumed to carry 75% of the ion current density, and the beam component carries the remainder. The beam velocity is kept at the same value as in the previous single component cases. The CEX velocity is determined by assuming a slightly supersonic condition, $M_{CEX} = 1.20$. The number density of the components can then be calculated from the component current density and velocity.

Table 5.2: Plasma properties for the beam-CEX component case.

	n_i, $10^{14}\,\mathrm{m}^{-3}$	v_i, $\frac{\mathrm{m}}{\mathrm{s}}$	T_i, K
Beam	0.480	2,381	11,600
CEX	1.439	1,026	300
Electrons	1.919	1,365	11,600

For the beam-CEX-double composite case, the double charge ions are assumed to carry 10% of the total current. Experimental measurements report a comparable fraction in the far field, for low power thrusters [78] and high power thrusters [79, 80]. In this case the double charge component is assumed to have a drift velocity equal to the average speed of the beam and CEX populations. Assuming the same total ion current density as before, these assumptions can be used to determine a unique velocity and number density for the double charge ions. The double charge temperature is not well defined, since the particles are assumed to be drawn from both the beam and CEX populations. The double charge temperature is therefore set at 11,600 K to represent the broad range in velocity.

Table 5.3: Plasma properties for the beam-CEX-double composite case.

	n_i, $10^{14}\,\mathrm{m}^{-3}$	v_i, $\frac{\mathrm{m}}{\mathrm{s}}$	T_i, K
Beam	0.432	2,381	11,600
CEX	1.295	1,026	300
Double	0.096	1,365	11,600
Electrons	1.919	1,365	11,600

Note that the assumptions for the CEX and double components are not entirely representative of an EP plume. Since charge exchange ions are formed throughout the plume, there is likely to be a broad velocity distribution that would be better represented by a high temperature. Double charge ions are formed in the thruster or by collisions in the near field, and acceleration by the electrostatic fields would produce a final drift velocity that is higher than the single charge ions achieve. A variation of the composite distribution that takes these effects into consideration is described and used in Sec. 5.5.2. However, these details are not crucial for evaluating the interaction between two or more components.

For these simulations, the most useful comparisons can be made from the profiles of ion number density. The plasma potential and electron number density maintain the same level of agreement with the Bohm sheath solution that has been demonstrated previously.

For the beam-CEX case, Figs. 5.21 and 5.22 are respectively the profiles of beam and CEX ion number density when simulated as separate plasmas. Notice that the separate components demonstrate the behavior discussed previously: the cold CEX ions are in very good agreement with the Bohm sheath solution, and the hot beam ions are at about 5% lower density throughout the sheath.

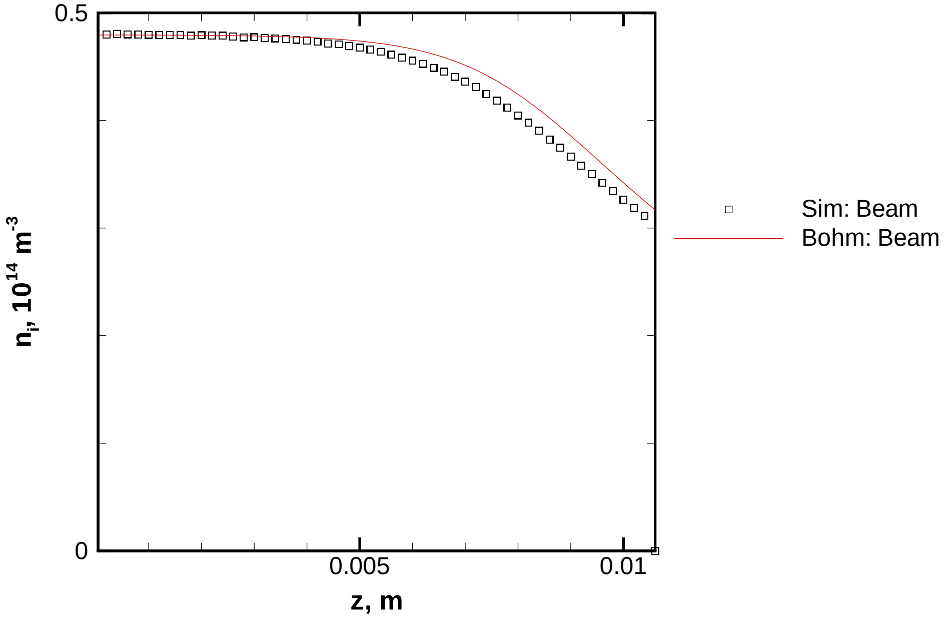

Figure 5.21: Profiles of ion number density near the centerline for the beam component case.

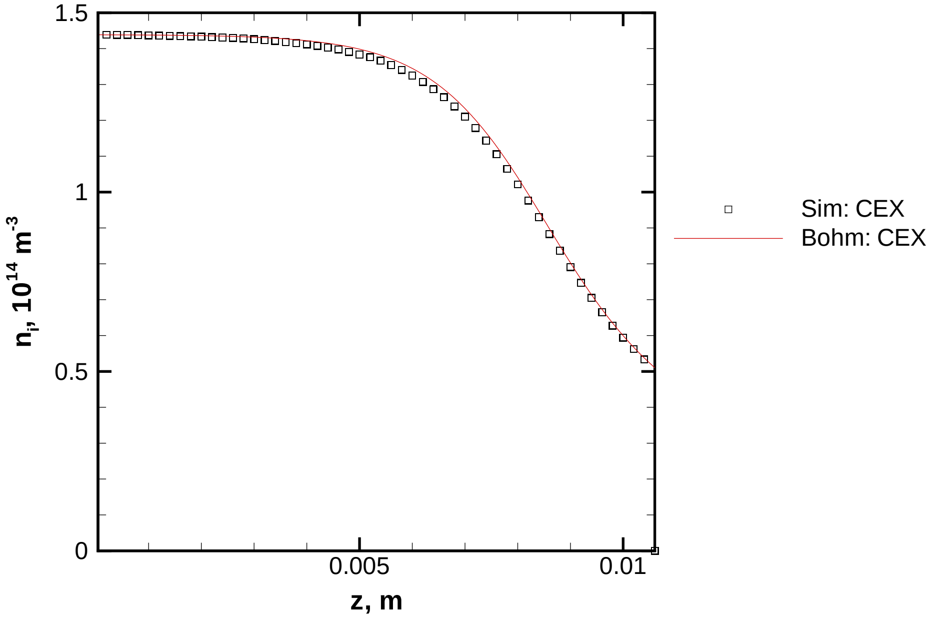

Figure 5.22: Profiles of ion number density near the centerline for the CEX component case.

Figure 5.23 shows the profiles of beam and CEX ion number densities when simulated as two components of the same plasma. A third profile labeled "All ions" gives the profile of charge density in the sheath, and is compared against the Bohm sheath solution calculated from the electron properties. Both of the component species maintain essentially independent sheaths, while the total charge density appears to follow the Bohm sheath solution calculated from the total charge density.

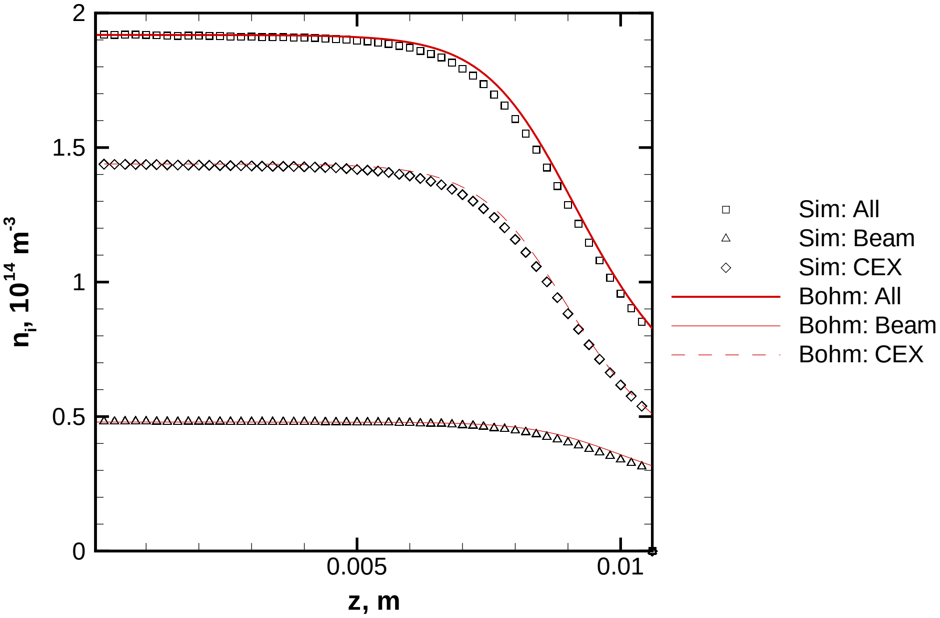

Figure 5.23: Profiles of total and component ion number density near the centerline for the beam-CEX case.

Contours of percent difference in density between the separate simulations and the combined beam-CEX simulation in Figs. 5.24-5.25 show that the individual component densities only interact in a region just upstream of the probe surface. This is consistent with the collective behavior of the plasma. Since the flow is collisionless, individual particles only interact with the collective electrostatic field. The presence of a second component population increases the charge density of the plasma and decreases the Debye length, which shields the bulk plasma more effectively.

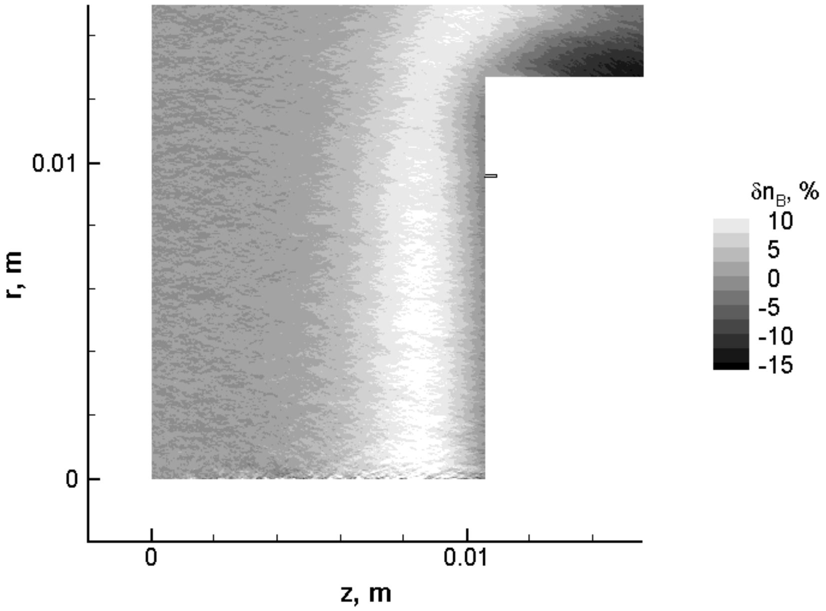

Figure 5.24: Contours of percent difference in beam ion number density for the beam-CEX case.

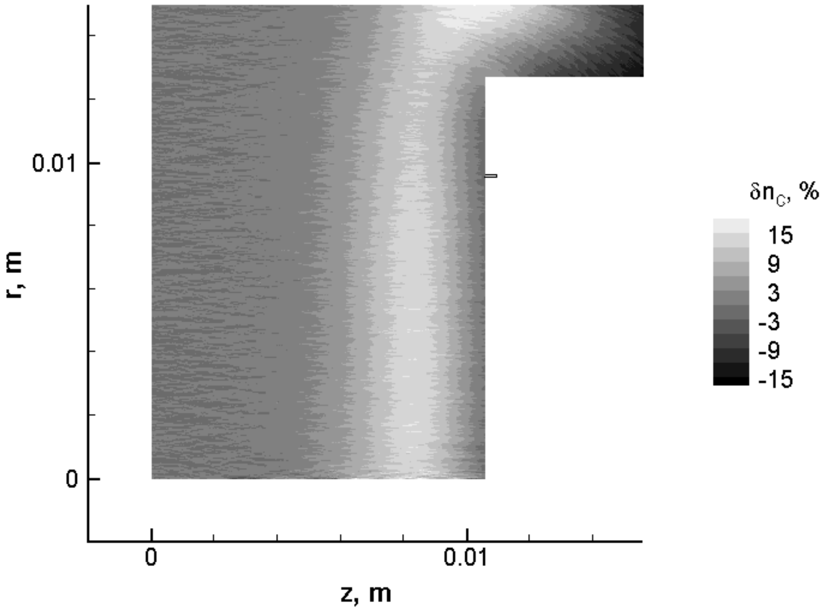

Figure 5.25: Contours of percent difference in CEX ion number density for the beam-CEX case.

Individual particles do not feel the electrostatic forces until closer to the probe.

However, since the boundary conditions enforce a fixed potential on the probe walls, the particles must fall through the same total potential drop. As a result, the particles achieve the same velocity at the surface of the probe as if there were no other ion components shielding them from the potential. Therefore the component ion number densities approach the expected values from their respective Bohm sheath solutions at the surface of the probe.

The same trends are observed when adding a double component. The separate simulation of the double component produces the profile in Fig. 5.26, and the composite simulation produces the profiles in Fig. 5.27. The simulated total charge density very accurately reproduces the Bohm sheath solution calculated from the electron properties.

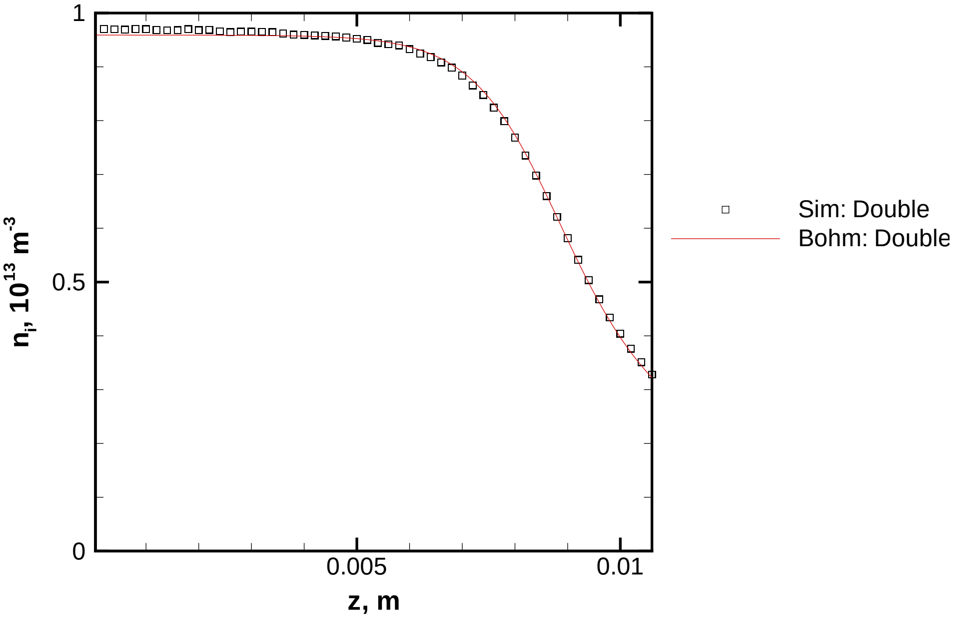

Figure 5.26: Profiles of ion number density near the centerline for the double component case.

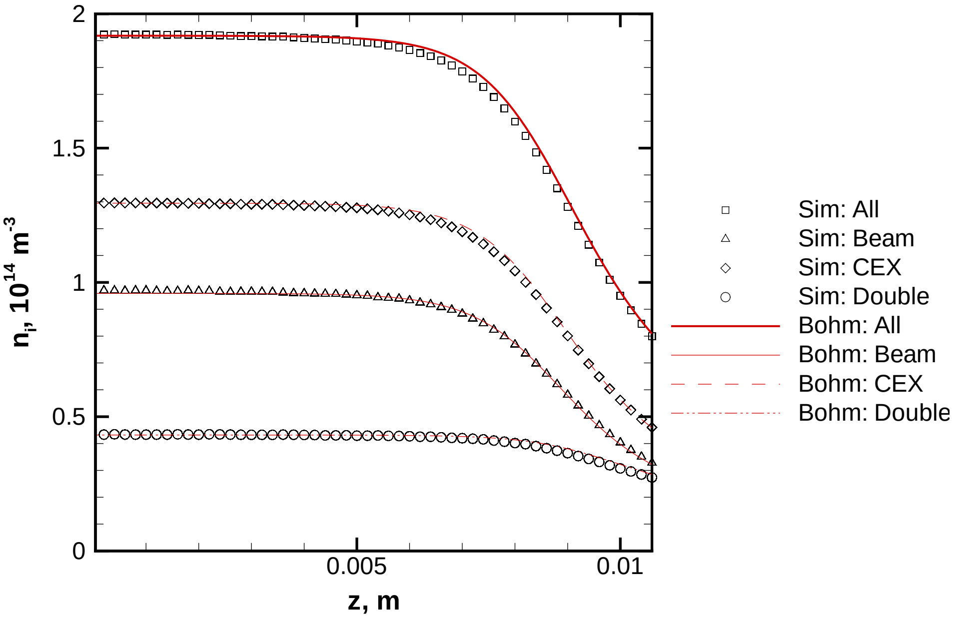

Figure 5.27: Profiles of total and component ion number density near the centerline for the beam-CEX-double composite case.

As could be expected from the beam-CEX results, adding a double charge component does not significantly affect the properties of the other component distributions at the surface of the probe.

5.3.4 Guard ring bias study

In most experimental setups, the guard ring is biased to the same potential as the collecting surface. This is intended to produce a uniform sheath over the probe surface, so that there is little or no focusing of current density onto the collecting surface. Then the area of the collecting surface is equal to the area of the current flux tube in the plasma, and the current density can be calculated by dividing the collected current by the collecting area.

This study uses the Boltzmann model to investigate how the collected current and streamlines of current are affected if the guard ring were intentionally or accidentally biased to a different potential than the collecting surface. The collecting surface is biased to −5 V in this study, and two cases are presented: a first case where the guard ring bias is set to −10 V, and a second case where the guard ring bias is set set to 0 V. Additional cases are not presented here, since they do not demonstrate any new features.

The beam-CEX distribution is used in this study so that any effects could be analyzed for relative trends on components with different average speeds and temperatures. For example, the CEX ions generally have a lower axial speed than the beam ions, and might be deflected near the edge of the collecting area while the beam ions are unaffected. However, no significant differences between the two populations were identified.

Contours of plasma potential and charge density are shown in Figs. 5.28 and 5.29 for the −10 V guard ring bias, and in Figs. 5.30 and 5.31 for the 0 V ring bias. In this case it is more useful to observe the streamlines of current in the flow.

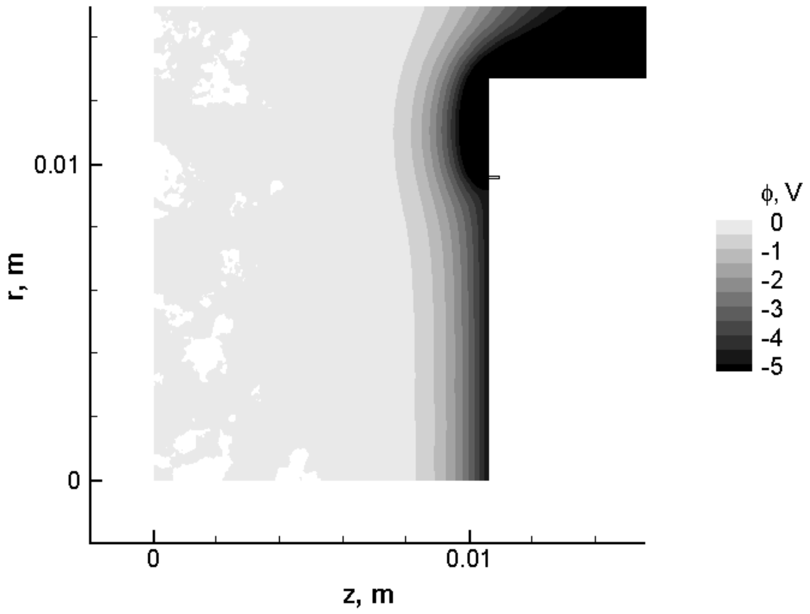

Figure 5.28: Contours of plasma potential for the guard ring bias of -10 V.

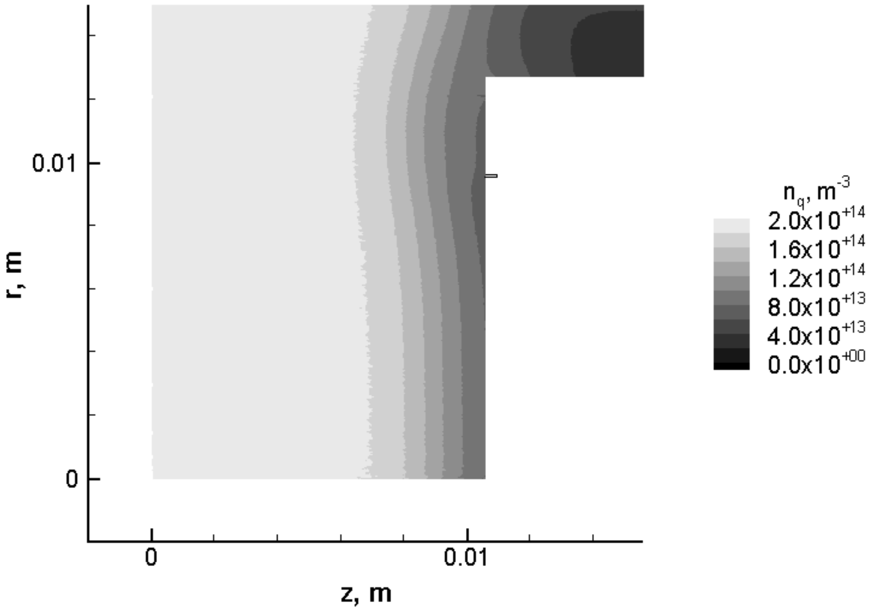

Figure 5.29: Contours of charge density for the guard ring bias of -10 V.

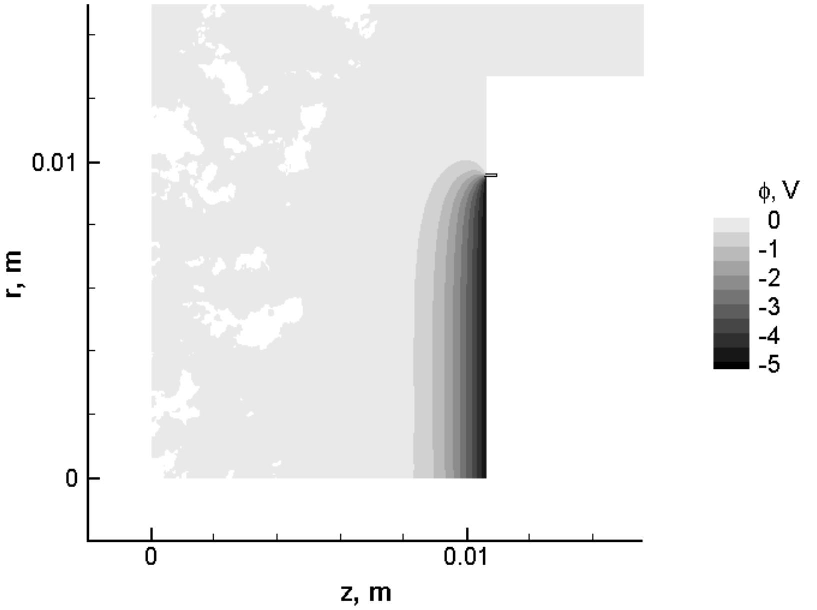

Figure 5.30: Contours of plasma potential for the guard ring bias of 0 V.

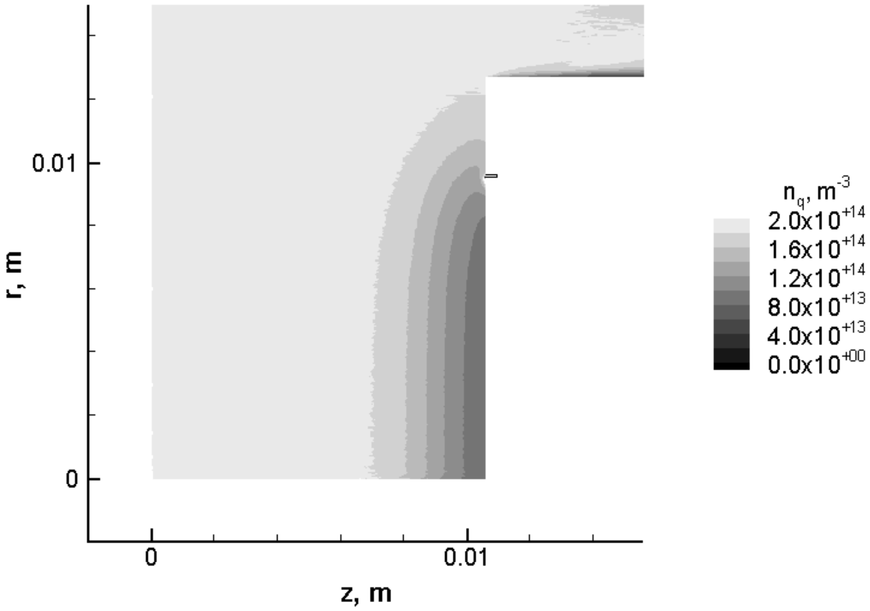

Figure 5.31: Contours of charge density for the guard ring bias of 0 V.

Streamlines are shown for the −10 V guard ring bias case in Fig. 5.32, for the uniform −5V bias case in Fig. 5.33, and for the 0V guard ring bias case in Fig. 5.34. In each figure there is a streamline originating at a radius of 0.00952 m that corresponds to the radius of the collecting surface. Ideally, that streamline should connect to the notch in the probe that separates the collecting surface from the guard ring. The best alignment occurs for the uniform −5 V bias case. However, the effect of a ±5 V difference between the guard ring and the collecting area does not drastically alter the streamlines.

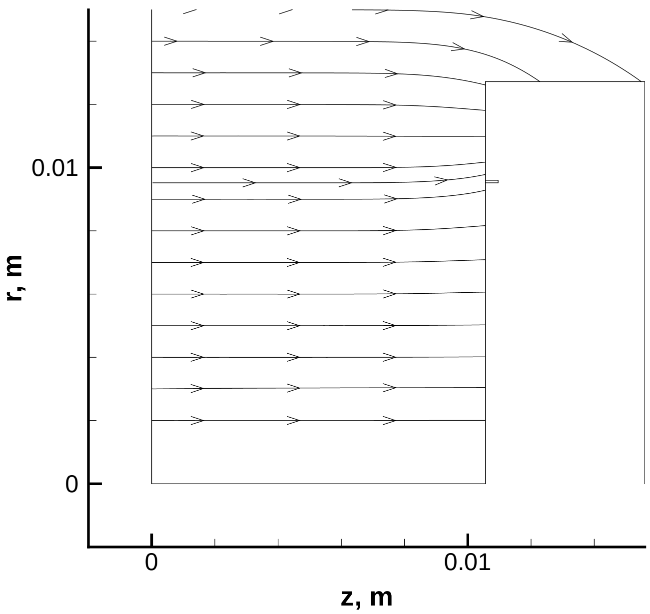

Figure 5.32: Streamlines of current for the guard ring bias of -10 V.

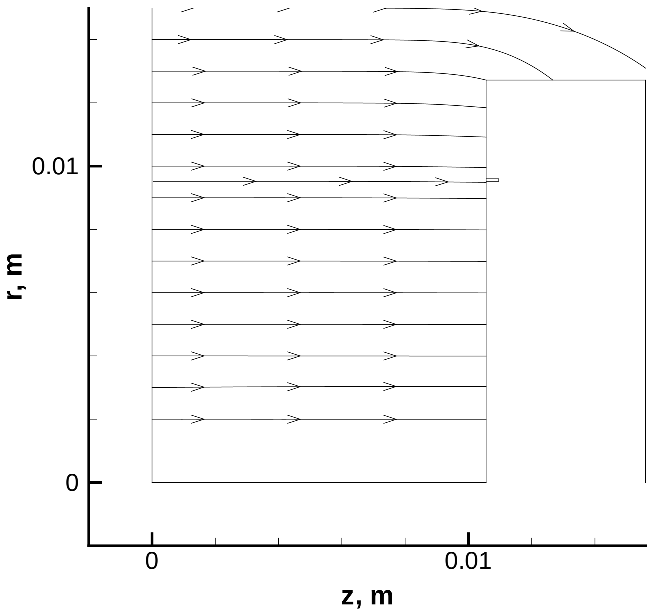

Figure 5.33: Streamlines of current for the uniform bias of -5 V.

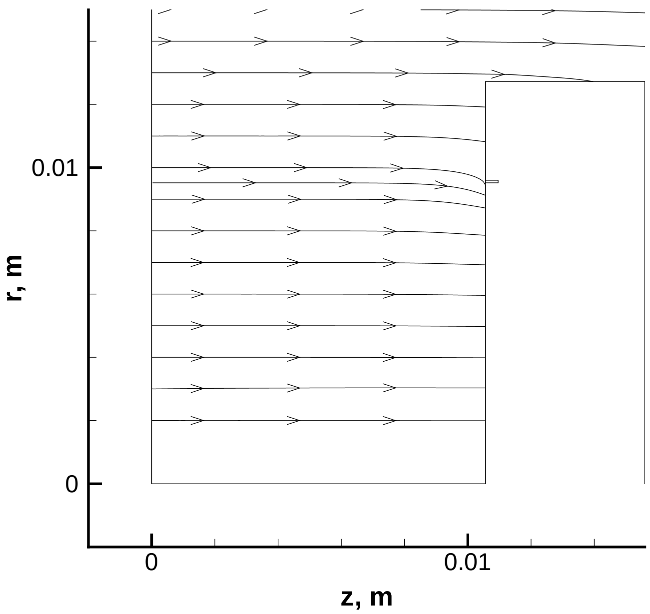

Figure 5.34: Streamlines of current for the guard ring bias of 0 V.

The simulated collected ion current for each of these guard ring cases is shown in Fig. 5.35 and reported in Table 5.4. The simulated collected ion current is compared with the theoretical ion current based on the current density in the freestream. Although there is a small error in the uniform bias case, it is not large enough to justify changing the guard ring bias.

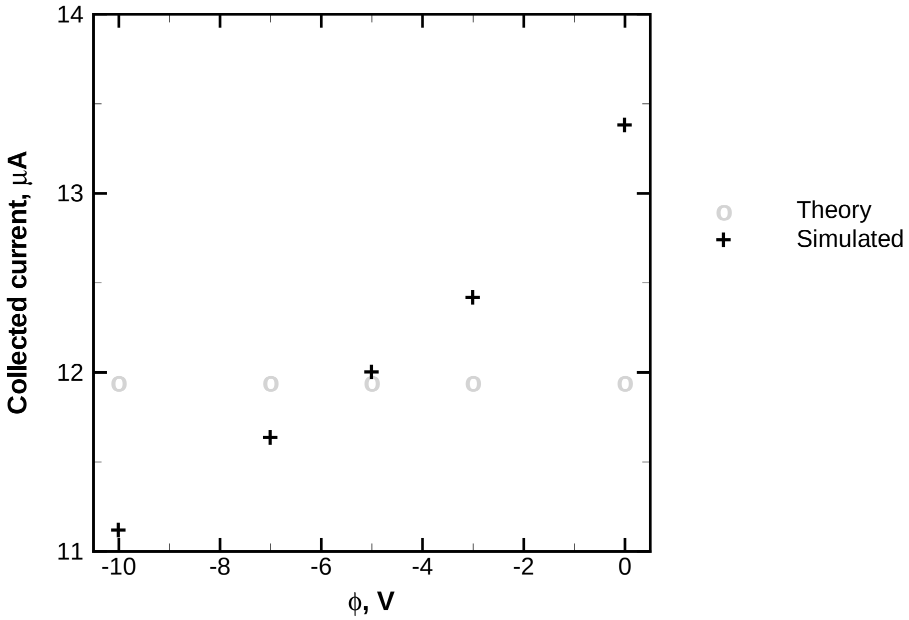

Figure 5.35: Simulated collected current as a function of guard ring bias.

Table 5.4: Simulated collected current for the guard ring relative bias.

ϕ_w, V	$J_{i,Sim}$, μA	$J_{i,Theory}$, μA	Error, μA	Error, %
0	13.383	11.948	1.435	12.01
-3	12.421	11.948	0.473	3.96
-5	12.004	11.948	0.056	0.47
-7	11.638	11.948	-0.310	-2.60
-10	11.121	11.948	-0.827	-6.92

5.3.5 Bias voltage sweep study

The final study with the Boltzmann fluid model is a sweep of the probe bias voltage from 0 V to -10 V, with the entire probe biased to a uniform potential. This study is intended to assess the accuracy of the Faraday probe over the range of current collecting conditions. At a large negative potential, the probe only collects an ion current since nearly all electrons are repelled. At zero potential, the probe collects approximately equal ion and electron currents.

The beam-CEX distribution is used in this study for consistency with the guard ring bias study. Since the entire probe body is biased uniformly, the different components are not expected to show different behaviors.

Properties in the flow fields are not important in this study, except to note the consistent level of agreement with the applicable Bohm sheath solution. The simulated collected currents are shown graphically in Fig. 5.36, and reported in Table 5.5. The theoretical total collected current is calculated at each probe bias setting from the freestream ion current and the fraction of electron current with sufficient velocity to reach the probe.

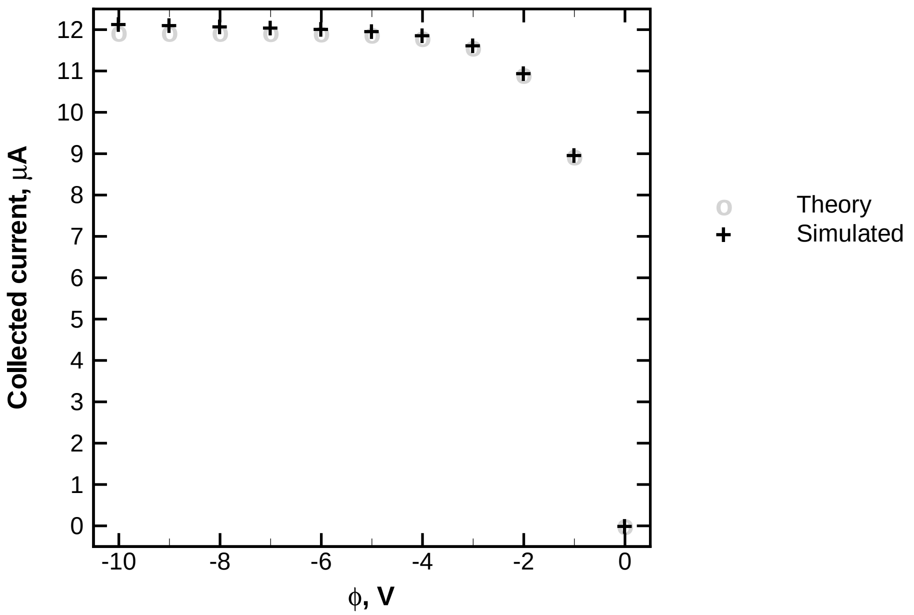

Figure 5.36: Simulated collected current over a range of probe bias.

Table 5.5: Simulated collected current for the probe bias sweep.

ϕ_w, V	$J_{Tot,Sim}$, μA	$J_{Tot,Theory}$, μA	Error, μA	Error, %
0	-0.007	0.020	-0.027	135.
-1	8.961	8.957	0.003	0.04
-2	10.940	10.930	0.011	0.10
-3	11.614	11.590	0.024	0.21
-4	11.857	11.820	0.037	0.32
-5	11.958	11.902	0.056	0.47
-6	12.011	11.931	0.080	0.67
-7	12.043	11.942	0.101	0.85
-8	12.072	11.946	0.126	1.05
-9	12.102	11.947	0.155	1.30
-10	12.128	11.948	0.180	1.51

From these results it is expected that the Faraday probe accurately measures the undisturbed freestream current. The apparently large error at 0 V is due to taking the difference between two small values of total current. At all other bias potentials the error in collected current is less than 2%.

There is a correlation between probe bias voltage and error in the collected current, which corresponds to sheath expansion. Recall that the plasma potential contours are curved near the outer edge of the probe, indicating a radial component of the electric field that tends to focus ions toward the centerline of the probe. The sheath extends farther from the probe for a larger potential drop, so the electric field focuses a larger volume toward the centerline. In this case the ions have a large axial velocity, so the focusing effect is small.

5.3.6 Comparison with experiment

The experiment in Ref. [77] provides one experimental datum for comparison. In that experiment the Faraday probe was biased uniformly to -5 V. The experimentally measured current at the point 50 cm downstream and 75° off-axis in the BHT-200 Hall thruster plume is reported as $12.3\,\mu$A. The simulated measurement for the -5 V case in Table 5.5 is slightly lower, at $11.958\,\mu$A. This is deemed very good agreement, with less than 3% difference between the values.

The numerical parameters of the simulations in the preceding sections were constructed to simulate the plasma flow at the same point in the plume for the same probe operating condition as in the experiment. However, recall from Sec. 5.1.1 that the initial estimate of the plasma conditions was taken from a previous numerical simulation of the BHT-200 plume. The good agreement between the simulated collected current and the experimental collected current is a further confirmation that the particular details of the ion distribution do not have a significant effect on the probe measurement.

5.4 Hybrid PIC Non-neutral detailed model study

The non-neutral detailed model is only used to simulate the cold ion case, which is intended to serve as a validation case by approximating the conditions of the planar Bohm sheath model. This case reveals a serious problem with the implementation, so no additional studies are conducted using this model.

Recall that the flow conditions for the cold ion case are intended to reproduce the assumptions of the planar Bohm sheath model. The ion temperature is $T_i = 300\,\mathrm{K}$, with the number density, velocity, and electron properties described in Sec. 5.1.1 and summarized in Table 5.1.

The contours and profile of plasma potential in Figs. 5.37 and 5.38 reveal a significant problem with the non-neutral model: the new results are not remotely similar to the Bohm sheath solution. The plasma potential profile in the sheath appears parabolic, with a large gradient at the inlet edge of the domain.

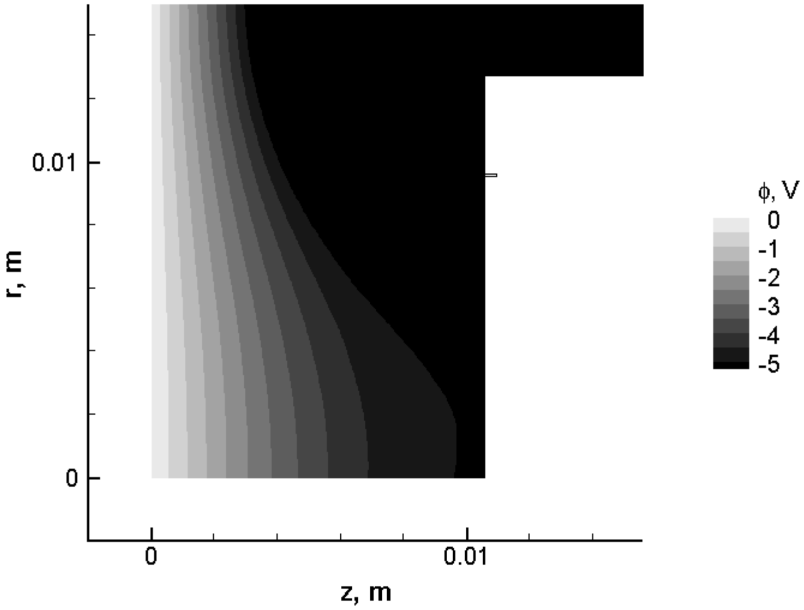

Figure 5.37: Contours of plasma potential for the cold ion case.

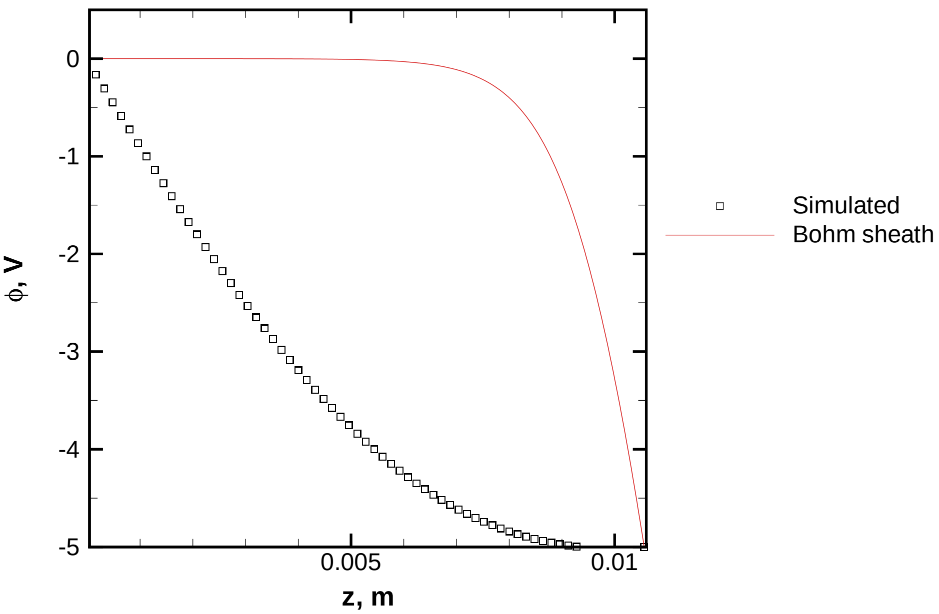

Figure 5.38: Profiles of plasma potential near the centerline for the cold ion case.

Contours of electron number density in Fig. 5.39 and ion number density in Fig. 5.40 appear almost identical. The electron number density contours show statistical scatter that is an artifact of the calculation that uses the instantaneous ion number density from the PIC module. However, no sampling is performed on the electron number density.

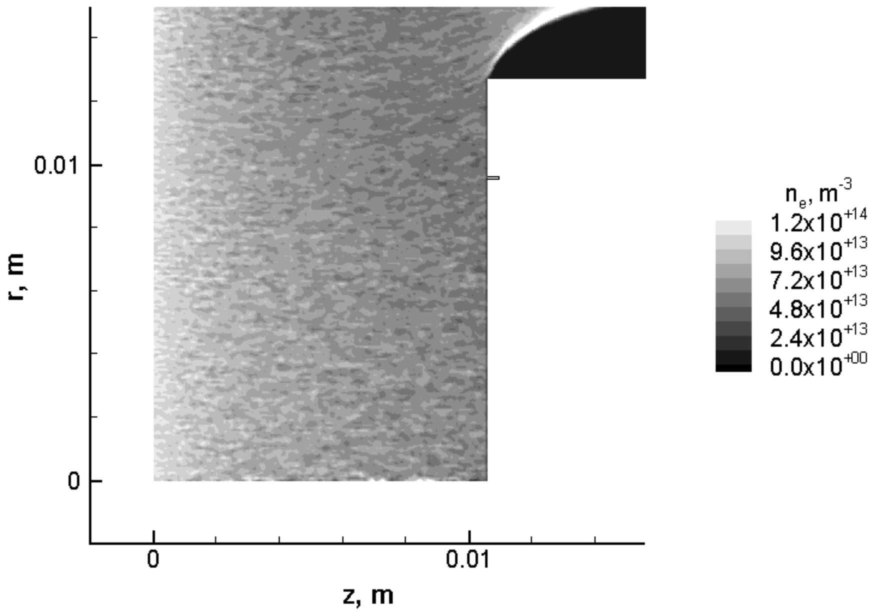

Figure 5.39: Contours of electron number density for the cold ion case.

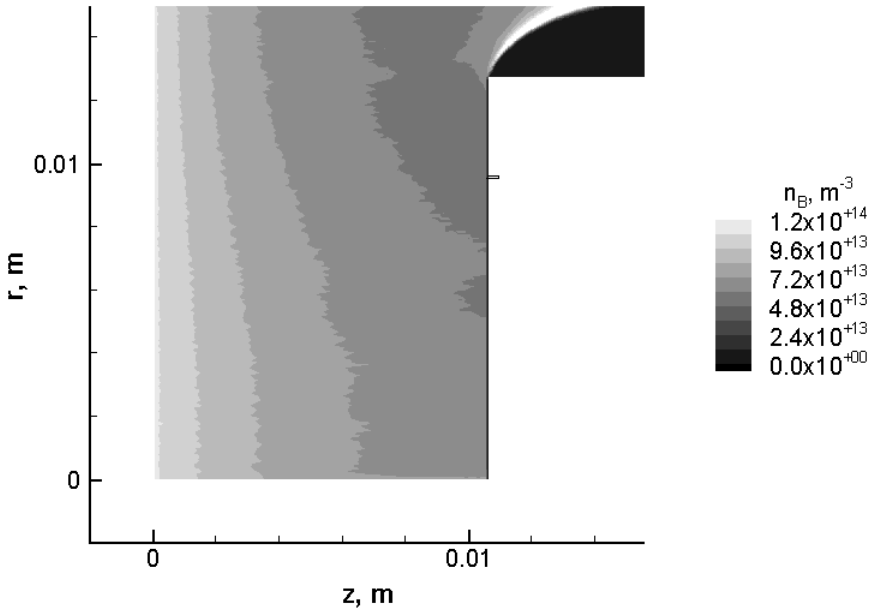

Figure 5.40: Contours of ion number density for the cold ion case.

Except for the statistical scatter, the profiles of electron number density in Fig. 5.41 and ion number density in Fig. 5.42 also appear identical. This indicates a neutral plasma up to the probe surface, which is not consistent with the expected physical processes in the sheath.

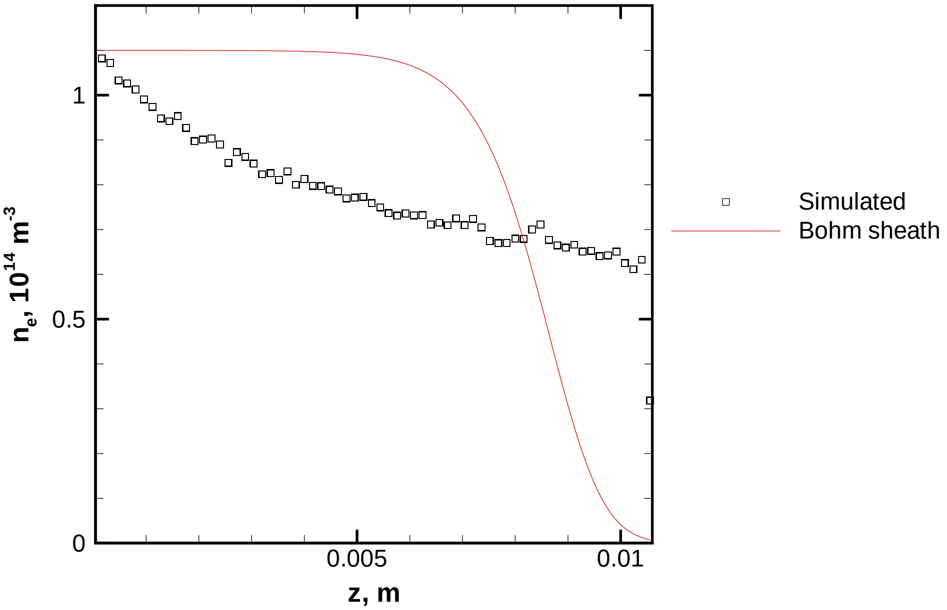

Figure 5.41: Profiles of electron number density near the centerline for the cold ion case.

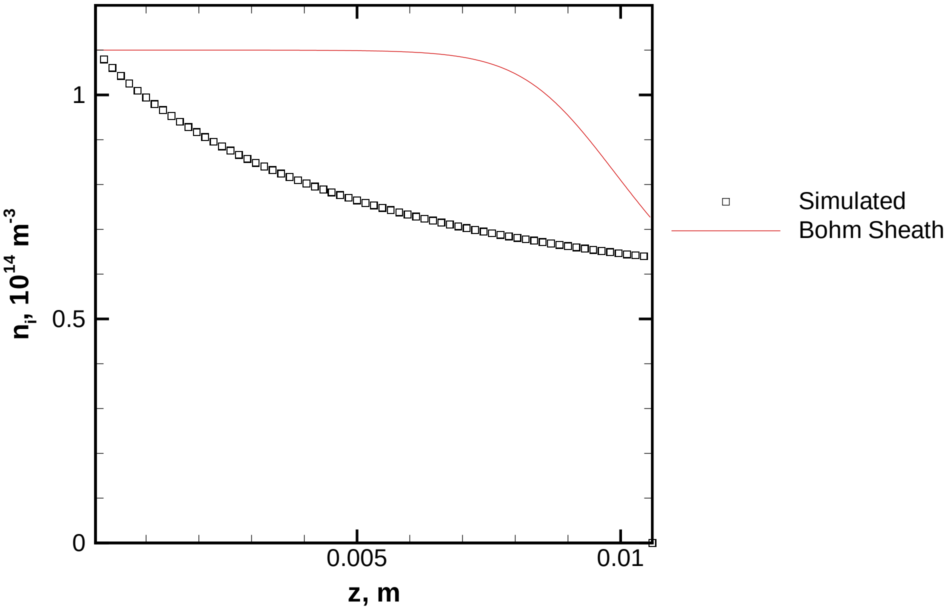

Figure 5.42: Profiles of ion number density near the centerline for the cold ion case.

Neither the plasma potential nor the number density results from the simulation are consistent with the expected features of an electrostatic sheath. The electric field is expected to vanish in the bulk plasma. That would correspond to approximately zero gradient in plasma potential at the inlet, rather than the large value seen in the results. The plasma is expected to become non-neutral where the negative probe potential repels electrons and accelerates ions, rather than remaining neutral throughout the sheath as in the results.

The neutral plasma result leads to an understanding of how this model fails. The simulation is initialized with uniform ion and electron number densities and uniform plasma potential equal to the inlet values. The initial value of $\nabla^2\phi$ is therefore zero throughout the domain. Electric fields are calculated and the ion particles are accelerated and moved, giving new values of ion number density. The electron number density is then calculated from the existing plasma potential and new ion number density according to the Poisson equation form in Eq. 4.31 of Chapter IV. Since the value of $\nabla^2\phi$ is zero, this calculation is equivalent to assuming neutrality. The differential equation for plasma potential is solved next, but the source term is zero since the ion and electron densities are equal. Over many iterations the plasma potential evolves to accommodate the boundary conditions, but the plasma remains neutral throughout the domain. This set of initial conditions together with this iteration procedure can only lead to a neutral plasma result.

Although it may be possible to rearrange the iteration steps to obtain a non-neutral result, this model is not developed any further in this dissertation. The Poisson-consistent model is available as an alternative, and successful, detailed model. Additionally, the non-neutral detailed model is significantly more time intensive than the Poisson-consistent model due to the larger number of ion particles required to limit statistical scatter and maintain stable electron number density calculations.

5.5 Hybrid PIC Poisson-consistent detailed model studies

The Poisson-consistent detailed model is used in two main studies that parallel the Boltzmann model studies of the plasma flow field. The first study uses the Poisson-consistent model to simulate the cold ion case for comparison with the Bohm sheath solution. The second study uses the Poisson-consistent model to simulate the composite multiple ion component case, and identifies a possible limitation of the model.

5.5.1 Bohm sheath validation case

Once again, the flow conditions for the cold ion case approximate the assumptions made in the planar Bohm sheath model. The ion temperature is $T_i = 300$ K. The electron properties and the ion number density and velocity are described in Sec. 5.1.1

and summarized in Table 5.1.

The contours of plasma potential in Fig. 5.43 show a nearly uniform sheath over the entire collecting surface, with edge effects limited to the outermost 0.002m (3 λ_D) of the probe surface. The profile of plasma potential in Fig. 5.44 is in excellent agreement with the Bohm sheath solution.

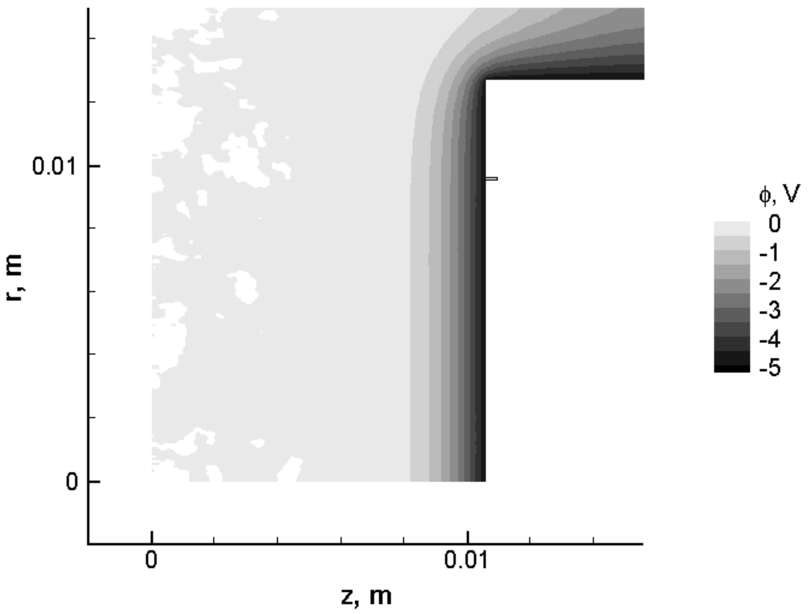

Figure 5.43: Contours of plasma potential for the cold ion case.

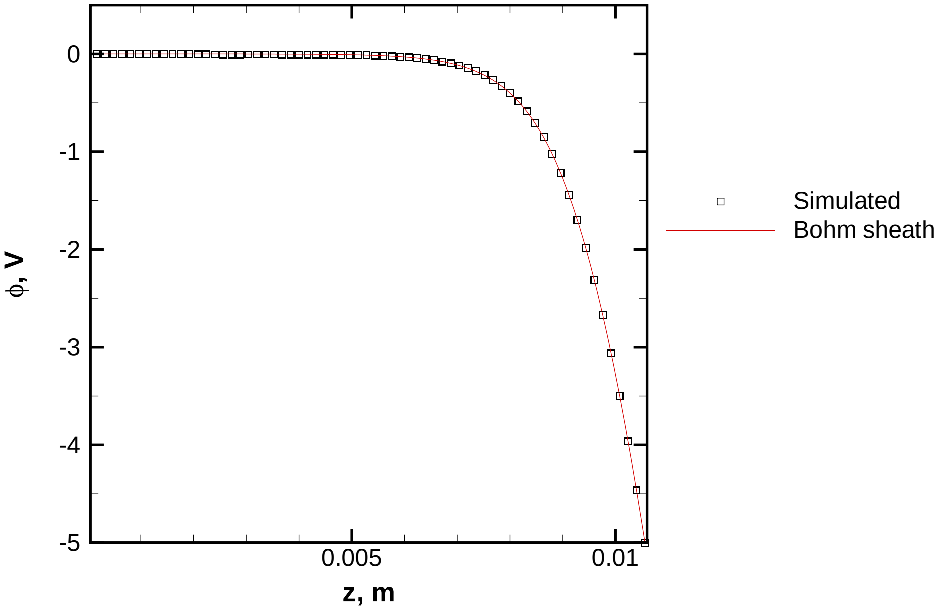

Figure 5.44: Profiles of plasma potential near the centerline for the cold ion case.

The contours of electron number density in Fig. 5.45 are solved from the differential equation in Eq. 4.32 of Chapter IV. Some statistical scatter is evident in the contours, and is expected since the electron number density is coupled to the ion number density by way of the electrostatic Poisson equation.

Although the differential equation is significantly more complicated than the Boltzmann relation, the electron number density profile in Fig. 5.46 still shows excellent agreement with the Bohm sheath solution. This indicates that the Boltzmann relation is an appropriate assumption for these conditions.

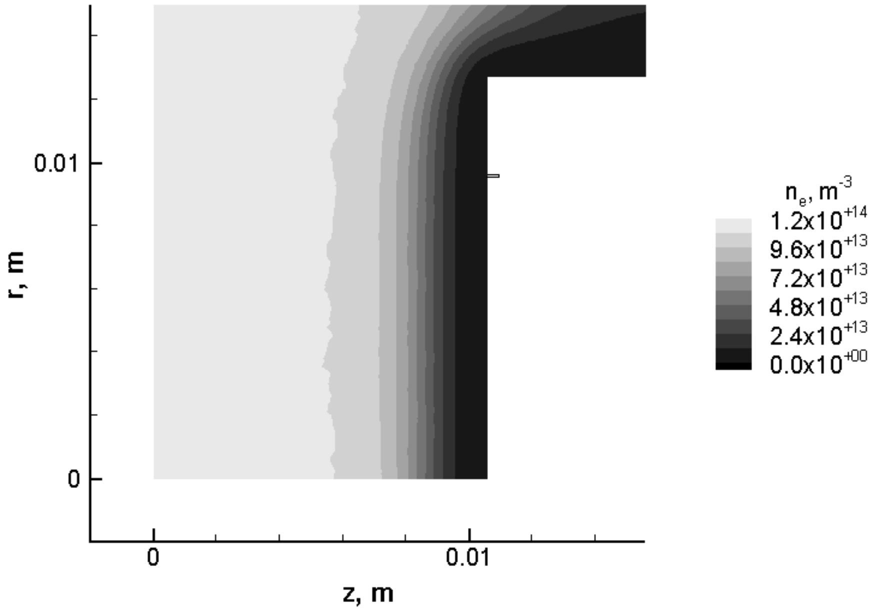

Figure 5.45: Contours of electron number density for the cold ion case.

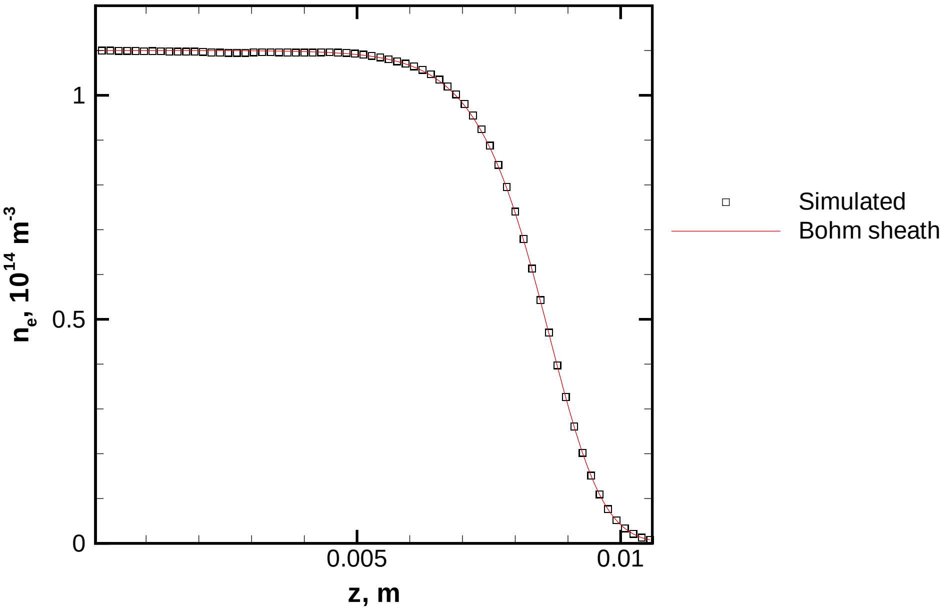

Figure 5.46: Profiles of electron number density near the centerline for the cold ion case.

The contours and profile of ion number density in Figs. 5.47 and 5.48 are likewise in excellent agreement with the Bohm sheath solution.

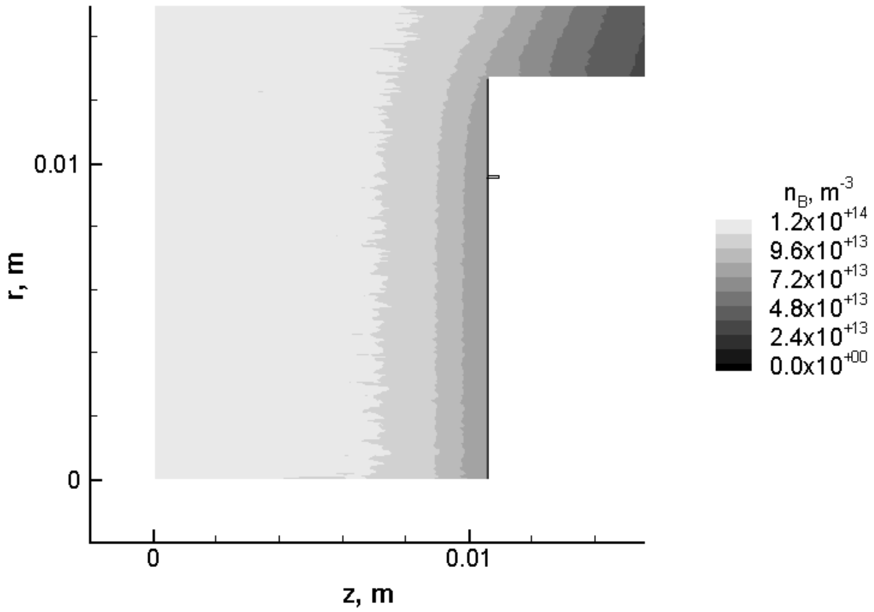

Figure 5.47: Contours of ion number density for the cold ion case.

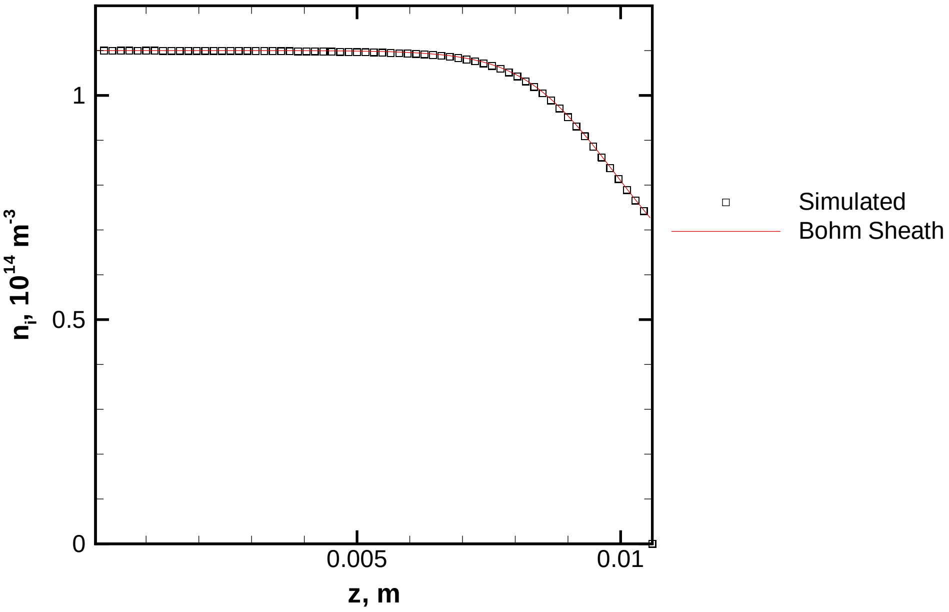

Figure 5.48: Profiles of ion number density near the centerline for the cold ion case.

The Poisson-consistent model very accurately reproduces the Bohm sheath solution for the cold ion case, which verifies the basic formulation and implementation of the model. The boundary conditions for electron number density also appear to work well. The ADI solver shows no difficulties with the differential equation for electron number density, despite concerns about its complexity and non-linearity.

5.5.2 Multiple component plasma studies

Intermediate studies of the hot ion case and the beam-CEX case are omitted for brevity, since the Poisson-consistent model yields consistently good agreement with the Bohm sheath solutions for those cases. A modified composite beam-CEX-double distribution case is more interesting, since it can be used to show a limitation in the predictive capabilities of the Bohm sheath model.

The inflow ion distribution here is a variation of the original composite case described in Sec. 5.3.3, referred to as the hot composite case. The beam component is unchanged. The density and drift velocity of the CEX component remains unchanged, but the temperature is raised to 11,600 K. Charge exchange ions are born in collisions with cold neutral gas that diffused out of the thruster. The charge exchange collisions can take place anywhere from the exit plane of the thruster to the surface of the probe, so a broad distribution in particle velocity develops depending on the relative potential drop from the point of formation to the probe. The high CEX temperature is intended to better represent the spread in velocities.

The properties of the double charge component are calculated by assuming that 10% of the freestream current density is carried by the double charge particles. The particles are assumed to be formed in the same locations and the same ratio as the beam and CEX components, and the electrostatic acceleration produces velocity that is larger by a factor of $\sqrt{2}$ due to the double charge. The velocity for the double charge component is then $\sqrt{2}$ times the mean velocity of the beam and CEX components. The double component number density is then calculated from the known current density and velocity.

The conditions for the hot composite case are summarized in Table 5.3. Since the hot composite case demonstrates unexpected behavior, a cold composite case will also be simulated for comparison. The only difference between the cases is that the CEX component temperature is 300 K for the cold composite case. All other properties for the inflow distributions remain unchanged from the values in the table.

Table 5.6: Plasma properties for the hot composite case.

	n_i, $10^{14}\,\mathrm{m}^{-3}$	v_i, $\frac{\mathrm{m}}{\mathrm{s}}$	T_i, K
Beam	0.432	2,381	11,600
CEX	1.295	1,026	11,600
Double	0.068	1,930	11,600
Electrons	1.863	1,406	11,600

Simulations using the Poisson-consistent model produce contours of the hot composite and cold composite cases that appear very similar to one another and to previous results. It is therefore most effective to compare the profiles of plasma properties in the sheath.

The profile of plasma potential for the hot composite case in Fig. 5.49 is seen to be consistently about 0.1 V lower than the Bohm sheath solution through much of the sheath. This is a much larger departure than expected from the Poisson-consistent model. In contrast, the plasma potential profile for the cold composite case in Fig. 5.50 is in excellent agreement with the Bohm sheath profile.

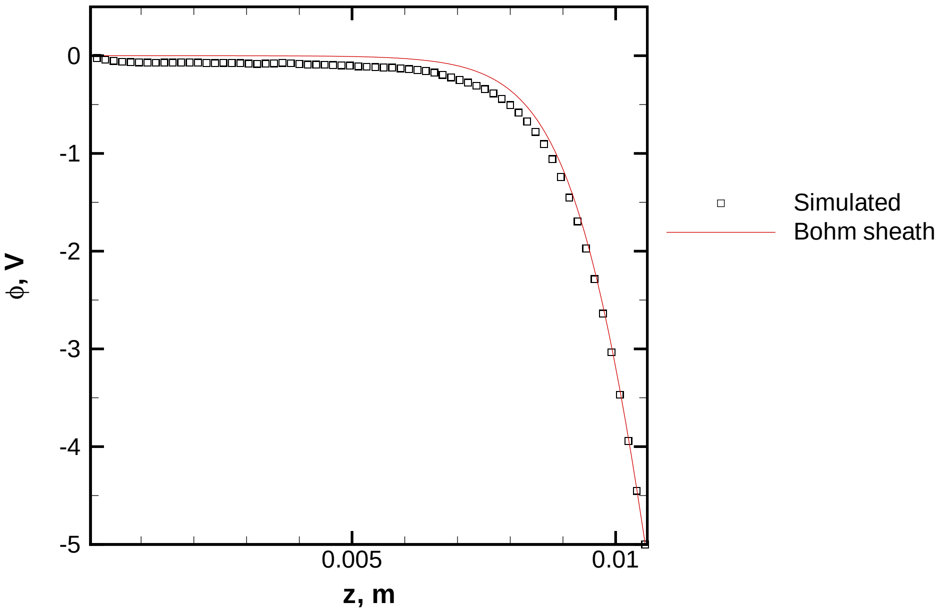

Figure 5.49: Profiles of plasma potential near the centerline for the hot composite case.

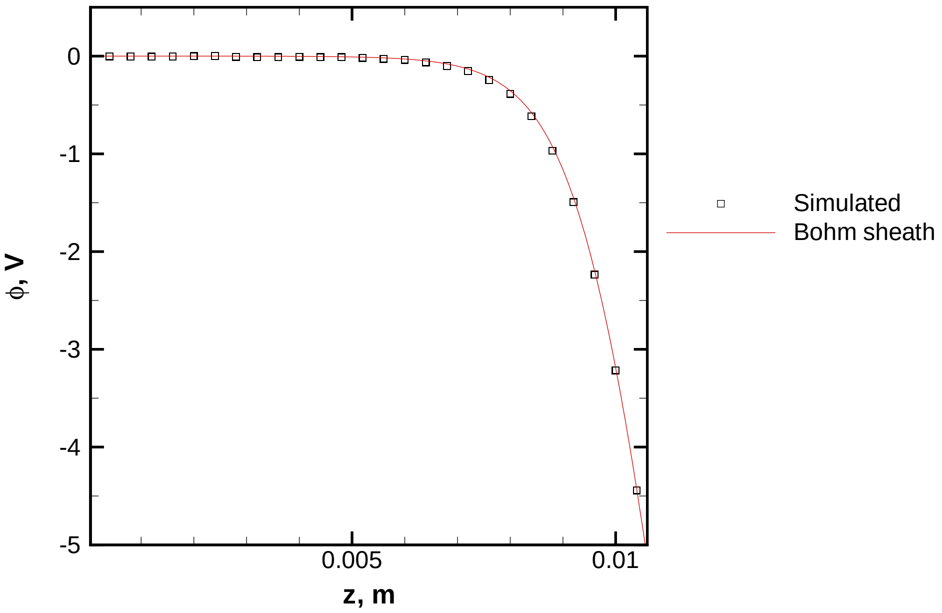

Figure 5.50: Profiles of plasma potential near the centerline for the cold composite case.

The electron number density profile for the hot composite case also shows a significant difference from the Bohm sheath solution in Fig. 5.51. However, the same profile for the cold composite case is in good agreement with the Bohm sheath solution in Fig. 5.52.

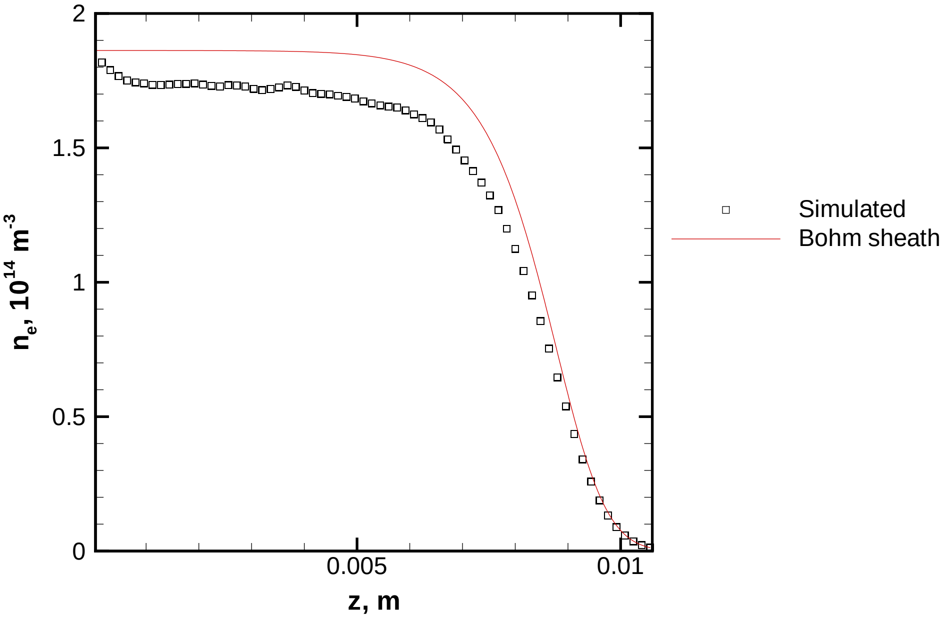

Figure 5.51: Profiles of electron number density near the centerline for the hot composite case.

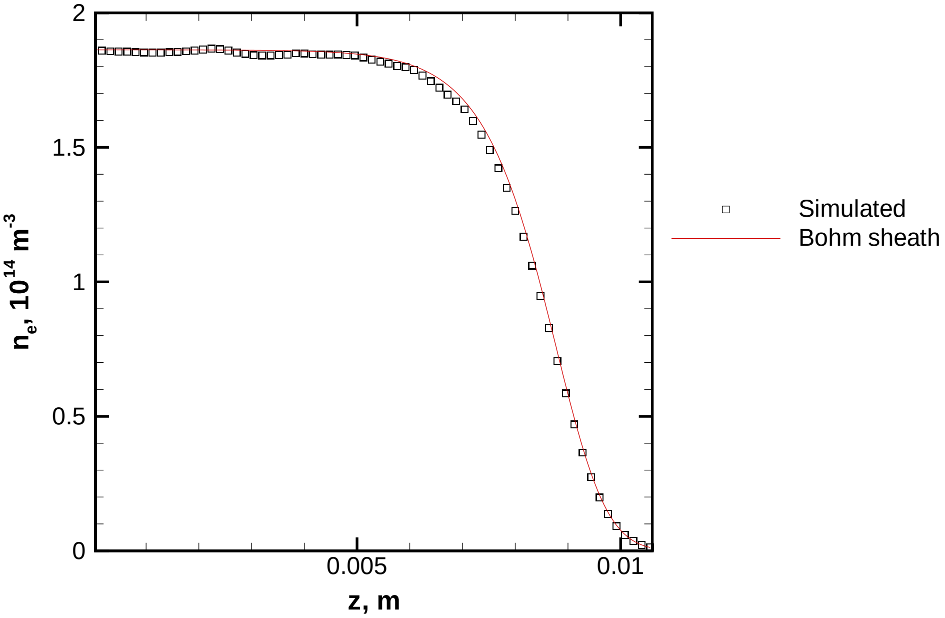

Figure 5.52: Profiles of electron number density near the centerline for the cold composite case.

Comparing the profiles of ion number density from the hot composite case, Fig. 5.53, with the cold composite case, Fig. 5.54, begins to explain the difference between the two cases. The CEX component of the hot composite shows a significant deviation from the Bohm sheath solution at the inlet and throughout the sheath. In contrast, the cold composite CEX component is in very good agreement with the Bohm sheath solution at all points. The beam and double components appear essentially the same for both cases, indicating that the difficulty in the hot composite case lies with the CEX component.

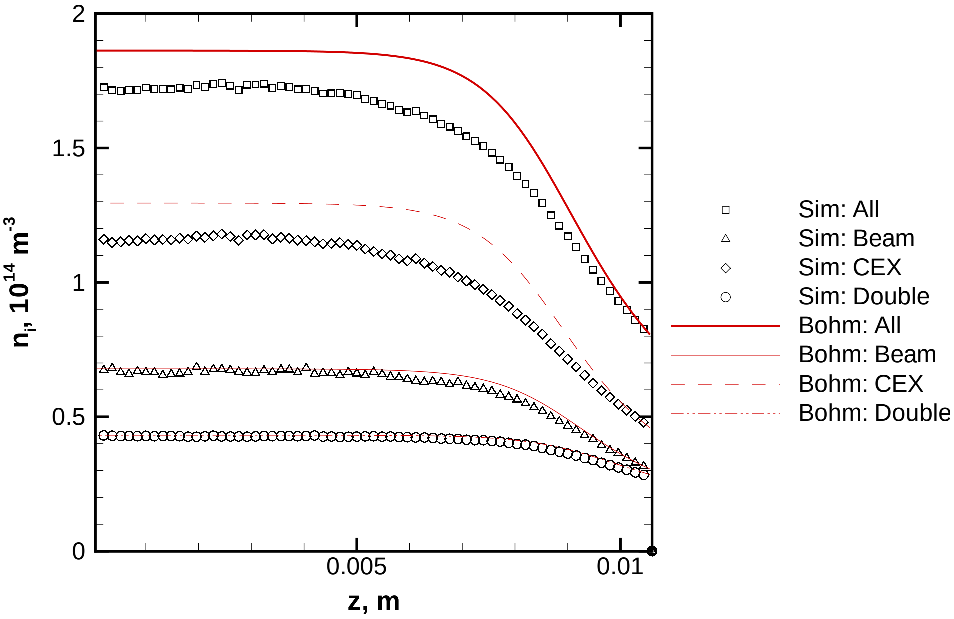

Figure 5.53: Profiles of total and component ion number density near the centerline for the hot composite case.

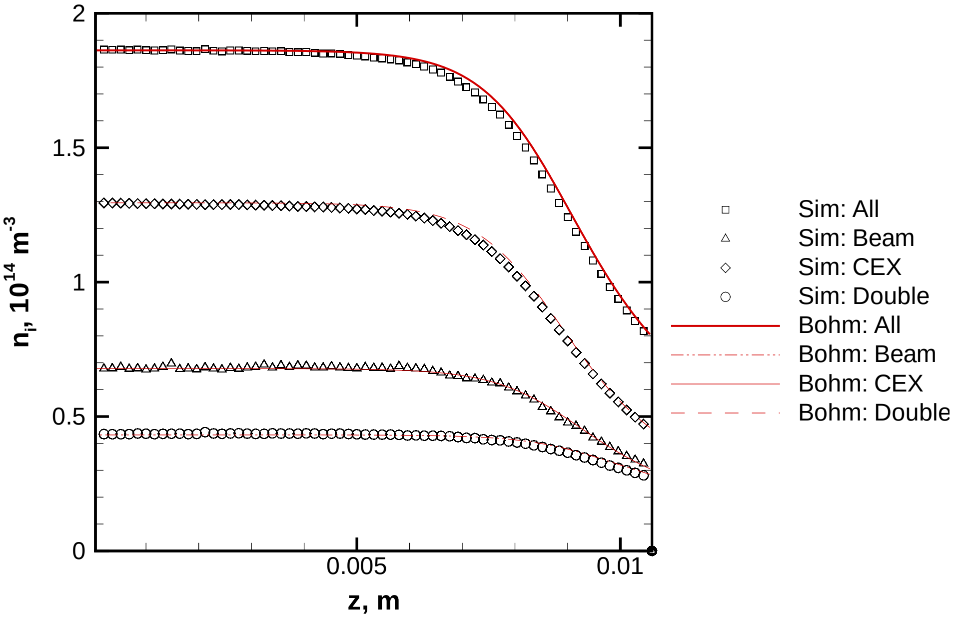

Figure 5.54: Profiles of total and component ion number density near the centerline for the cold composite case.

The normalized distribution functions for the hot composite and cold composite cases are shown in Fig. 5.55. A feature that stands out is that nearly 11.5% of the hot composite CEX distribution is backflow, i.e., $v_i < 0$. For comparison, just 0.27% of the beam component distribution is backflow, and 1.2% of the double component distribution is backflow. The cold CEX component distribution has negligible backflow.

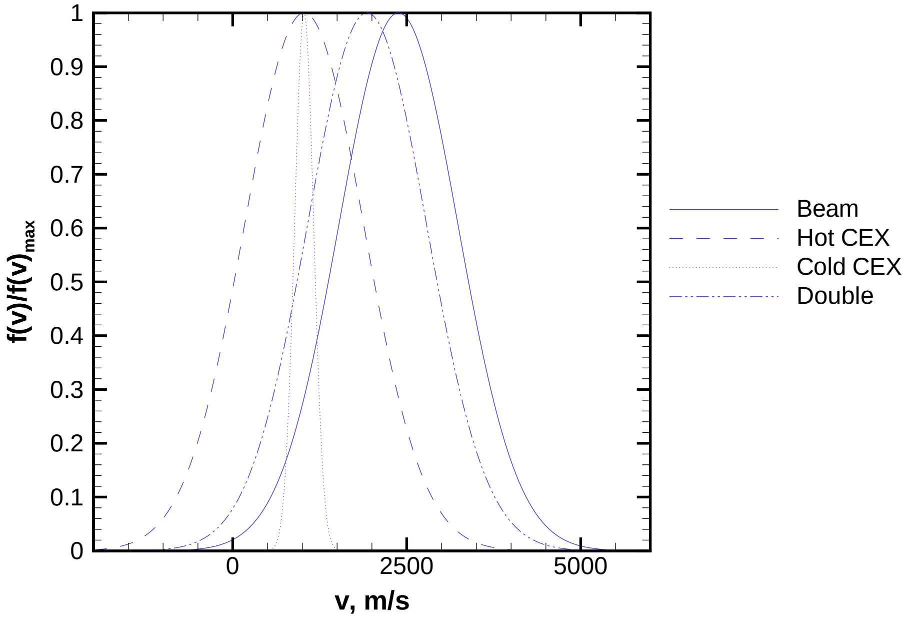

Figure 5.55: Normalized distribution functions for the hot composite and cold composite cases.

The Bohm sheath solution assumes cold ions with a uniform positive velocity. However, a significant portion of the hot composite CEX distribution is backflow, which explains why the simulated density does not match the predicted number density far from the probe. An estimate of the density for just the forward flowing ions in the hot composite CEX component is 88.5% of the freestream density, or 1.15×10^{14}, m^{-3}. This is much closer to the simulated value of hot composite CEX density far from the probe in Fig. 5.53. The Bohm sheath solution calculated from freestream conditions is not a reliable predictor for the sheath structure or collected current when a significant backflow component is included. This limitation is loosely related to the Bohm criterion.

The PIC model used in the Poisson-consistent simulations injects particles into the domain with velocities chosen statistically from the freestream distribution. Therefore some of the CEX component particles introduced along the outer radial edge of the domain are likely to be backflowing particles. There are not enough of those particles to completely replenish the backflowing distribution everywhere upstream of the probe, so the simulation partly resembles a geometric shadowing sheath that reaches upstream from the probe. At present the PIC model only injects particles into the domain with positive velocity from the two inlet edges at the upstream and outer radial edges of the domain. This could be improved by also injecting backflow particles from the downstream edge of the computational domain, along region 4 in Fig. 5.2.

The Poisson-consistent model simulations are in very good agreement with the Bohm sheath solution, provided there is not a significant fraction of backflow. By including backflowing particles, the Poisson-consistent model offers the possibility to simulate plasma sheaths for conditions where the Bohm sheath cannot obtain a stable solution, such as in low Mach number flows or in stationary plasmas.

5.6 Conclusions and implications for probe design

The results in this chapter lead to several conclusions about plasma behavior in a probe sheath, and a few design and operational guidelines for Faraday probes.

The planar Bohm sheath solution is found to be an excellent predictor for plasma properties near the centerline in the sheath. A high temperature Maxwellian ion distribution alters the ion number density in the sheath, lowering it by a few percent from the Bohm sheath profile. A plasma composed of one or more Maxwellian ion components forms a sheath that is more compact than any individual component, since each component contributes to shielding the plasma from the probe potential. The Bohm sheath solution calculated from total charge density and mean velocity at the inlet is an excellent predictor for plasma potential and total charge density in the sheath of a composite distribution. Additionally, the Bohm sheath solutions for number density calculated using the overall plasma potential remain good predictors for each component in the sheath of a composite distribution.

If the plasma conditions include a significant reverse flow component, the Bohm sheath solution is not a reliable predictor. This limitation is essentially a restatement of the Bohm criterion. A significant reverse flow component sets up a geometric shadowing situation, which cannot be handled with the planar Bohm sheath model. The hybrid fluid PIC models may still be capable of accurate prediction of the sheath, provided that ion particles are injected with forward and backward velocities from appropriate inlets.

The two dimensional edge effects of the probe are limited to an annular region near the outer edge of the probe. In the studies reported here, the effects were limited to about $3\,\lambda_D$ from the edge of the probe. A Faraday probe should therefore be designed with a guard ring that is at least $3\,\lambda_D$ wide, as calculated for the largest anticipated Debye length. The separation between the collecting area and the guard ring should be minimized to maintain a uniform sheath over the entire probe surface.

The guard ring should be biased to the same potential as the collecting surface. This configuration can reliably measure the freestream current with less than 2% error from $0\,\mathrm{V}$ to $-10\,\mathrm{V}$ bias potential for the plasma conditions considered. However, sheath growth occurs as the potential bias is made more negative, and two dimensional focusing effects increase the collected ion current. The error in the current density measurement due to sheath growth is about 0.25% per Volt for the probe and plasma conditions described.

Chapter VI

Multigrid Methods

Simulations using the hybrid fluid PIC model take considerable time to complete, from 25 hours for the quasi one dimensional cases to 35 hours for the multiple component cases described in Chapter V. The computational domain needed to resolve an electrostatic sheath is two to three times larger for a wake surface than for a ram surface. The associated computational time requirement scales accordingly, making it impractical to attempt simulations of a reversed Faraday probe without first improving the speed of the computational code.

The computational time of the hybrid fluid PIC code is evaluated in this chapter. As part of that evaluation, routines that operate on the particles are identified as major contributors to the overall time. A multigrid method is introduced that allows a coarser grid to be used for the PIC model in order to reduce the total particle count and speed up the code. The multigrid version of the hybrid fluid PIC code is found to be substantially faster than the single grid version while obtaining the same precision and accuracy.

6.1 Time profiling

A time profile of the hybrid fluid PIC computational code is performed using built-in compiler options and running the code for 15,000 iterations. The results are reported in Table 6.1. Routines accelerate, move, collide, weight_to_grid, and sample carry out the steps of the PIC model for the simulated particles. Routines e_continuity, e_momentum, e_energy, and e_poisson set up the coefficient matrices and conduct the ADI iteration of the discrete differential equations in the electron fluid model. Routine thomas_adi is the solver that is called from each of the fluid model routines to actually solve the differential equations for each line or column. There are also other routines that are called infrequently, including initialization and data output routines, that contribute a small amount to the overall simulation time.

Table 6.1: Time profile results of the hybrid fluid PIC computational code.

Routine	Time, s	Time, %	Type
accelerate	10,645.00	18.96	particle
weight_to_grid	8,590.00	15.30	particle
sample	8,475.00	15.09	particle
move	6,570.46	11.70	particle
e_energy	6,302.90	11.22	fluid
thomas_adi	4,855.80	8.65	fluid
e_poisson	4,362.23	7.77	fluid
e_momentum	3,866.20	6.89	fluid
e_continuity	1,395.50	2.49	fluid
collide	687.87	1.23	particle
others	399.90	0.70	-
Total	56,151.06	100.00	

The final column of the table indicates whether the time spent in each routine scales with the number of particles or the number of nodes in the fluid grid. The four most time intensive routines all operate on particles, and together those routines account for 61% of the total simulation time. The next five routines all operate on the fluid grid, and account for 37% of the total simulation time. A reduction in either particle count or grid node count could lead to a significant speedup.

6.2 Multigrid technique

In Chapter V the grid spacing is driven by the requirements of the fluid model, and cannot be increased significantly without affecting the accuracy of the simulation results. However, the spacing is much smaller than required to obtain accurate results from the PIC or DSMC particle models. Since the particle count per cell is held near 20 to maintain good statistical properties, the total number of simulated particles is very high in the hybrid fluid PIC simulations.

The disparity in grid spacing requirements suggests that an approach related to the multigrid methods developed in computational fluid dynamics might be useful here. In a CFD application, a multigrid method is used to accelerate the solution of a system of differential equations. The equations are first solved on a coarse grid to obtain an approximate solution. That solution is "prolonged" or interpolated to provide the initial estimate of the solution on a fine grid. The equations are solved on the fine grid, and the fine solution can then be restricted back to the original coarse grid, or prolonged to a finer grid and solved again [81, 82].

In the hybrid fluid PIC setting, a multigrid method can solve different models on separate grids. The particle model is used on the coarse "PIC grid" to obtain the ion and neutral number densities. Those densities are prolonged to a fine "fluid grid." The electron fluid model equations are then solved on the fluid grid. By introducing a multigrid system, the number of PIC cells and particles can be reduced on the coarse grid, while still maintaining the fine spacing required for the fluid model solutions on the fluid grid.

The modifications and additions to the computational code are not extensive. Support for separate PIC and fluid grids must be added. A new interpolation step must be added to prolong the particle densities to the fluid grid, and the electric field acceleration calculation must be modified to weight electric fields from the nodes of the fluid grid to the particles. The multigrid iteration cycle is essentially the same as the original iteration cycle in Sec. 4.4, except that the interpolation step is added:

1. Weight particle density to the nodes of the PIC grid
2. **New:** Interpolate particle density to nodes of the fluid grid
3. Solve electron continuity equation on fluid grid
4. Solve electron momentum equation on fluid grid
5. Solve electron energy equation on fluid grid
6. Repeat steps 4-5 to converge coupled equations
7. **Modified:** Weight electric fields from fluid grid nodes to particles
8. Move particles on the PIC grid
9. Collide PIC particles in PIC grid cells
10. Sample particle properties on PIC grid

For simplicity, the PIC grid and the fluid grid are constructed with coincident nodes. The PIC grid has twice the cell spacing of the fluid grid, so that each rectangular PIC cell contains exactly four rectangular fluid cells. The interpolation routine transfers values from the PIC grid to the fluid grid at shared nodes, and uses linear interpolation to calculate values at the additional fluid grid nodes.

6.3 Validation and speedup assessment of multigrid version

The new multigrid version of the hybrid fluid PIC computational code is validated by repeating several of the cases from Chapter V. The composite case using the Poisson-consistent detailed model is considered the most difficult simulation, and those results are compared here. Contours of the potential, Fig. 6.1, electron density, Fig. 6.2, and charge density, Fig. 6.3, are very consistent between the original and multigrid simulations.

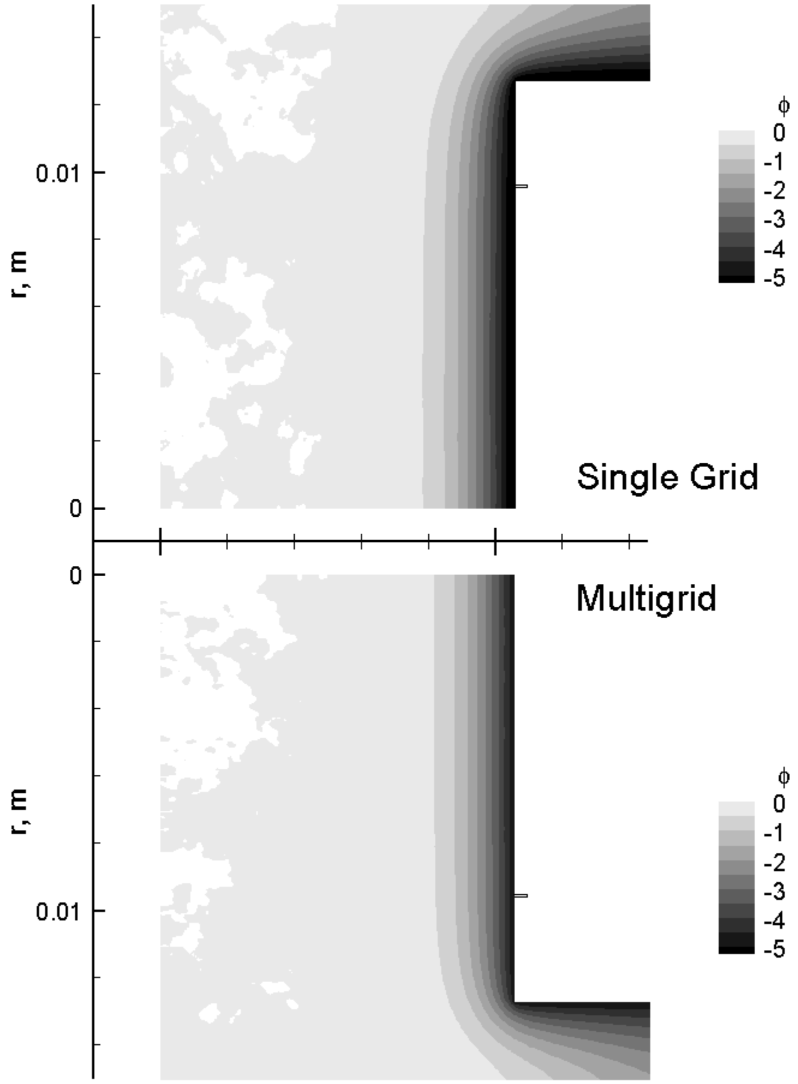

Figure 6.1: Contours of potential for the original and multigrid composite simulations.

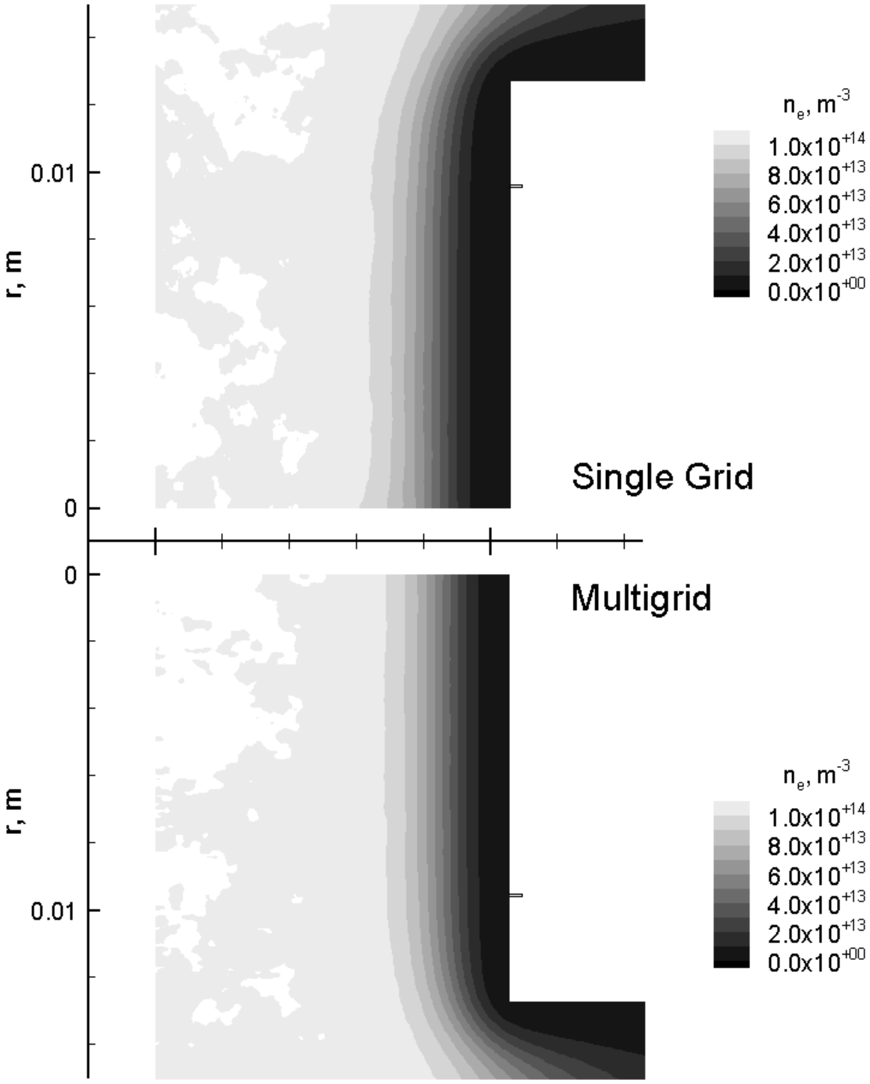

Figure 6.2: Contours of electron number density for the original and multigrid composite simulations.

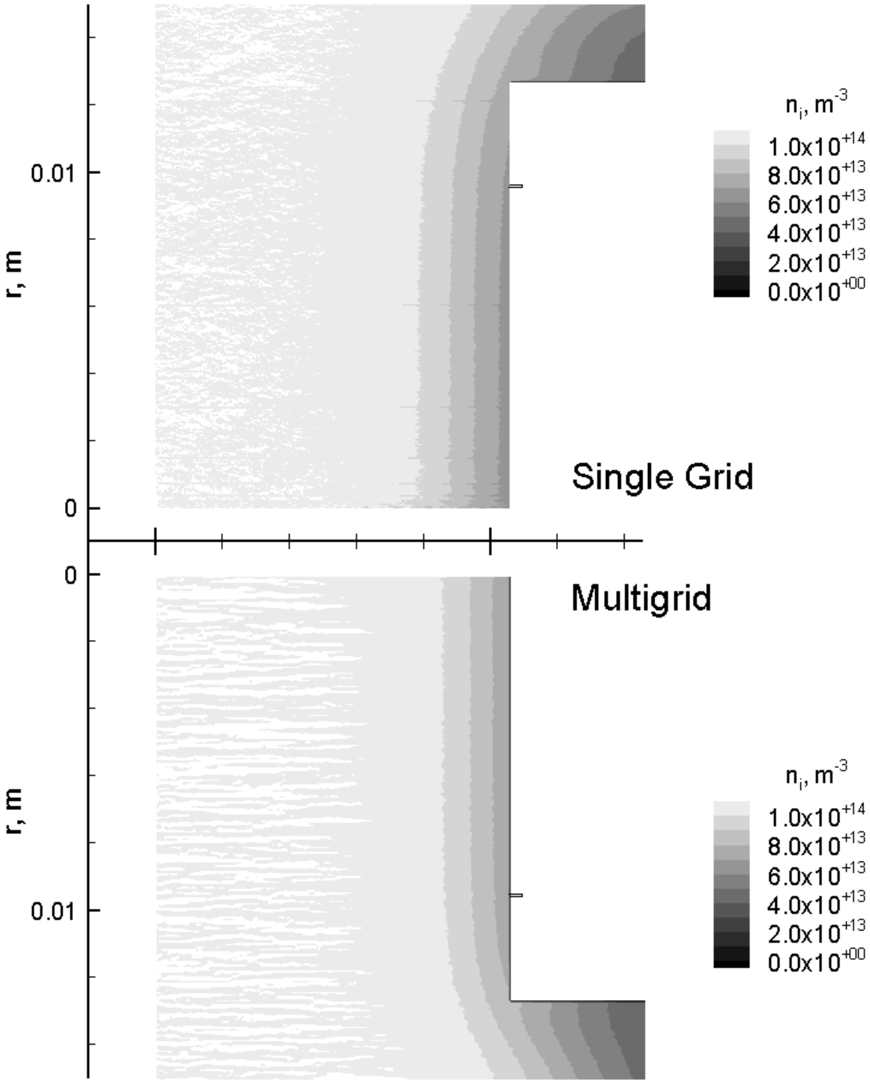

Figure 6.3: Contours of charge density for the original and multigrid composite simulations.

There are no apparent systematic differences or large local differences between the original and multigrid simulation results. The differences can be quantified at the coincident nodes on the PIC grid, giving a maximum error of ±2% from the original solution. From these comparisons it is concluded that the multigrid version accurately obtains the same solution as the original code.

The expected speedup factor for the multigrid version is based on the assumption that the time spent in particle routines scales linearly with the total particle count, while the time spent in fluid routines scales linearly with the number of fluid grid nodes. The multigrid PIC grid has a factor of 4 fewer cells than the original grid, so the particle count drops by the same factor and the expected speedup factor is 4 for all of the particle routines. The multigrid fluid grid is identical to the original grid, so the fluid routines should take the same amount of time, giving an expected speedup factor of 1 for all of the fluid routines.

The speedup of the multigrid version of the code is evaluated by performing a time profile using the same built-in compiler options as before. The profile results are shown in Table 6.2 for the new multigrid version time, MG Time, together with the original single grid version time, SG Time, for comparison.

The actual speedup factor is computed as the ratio of the original time to the new time. Each of the fluid routines show a small speedup which is probably due to uncontrolled secondary effects, such as better use of cache memory. The particle routines show a speedup factor that meets or exceeds the anticipated factor of 4. The routines move, weight_to_grid, and sample achieve a speedup that is nearly a factor of 2 higher than expected. The new interpolation routine is added into routine weight_to_grid, making the speedup factor even more impressive.

The multigrid version achieves an overall speedup of 2.22, meaning that the same domain and plasma conditions can be simulated in less than half the total time of the original version. This is enough of a speedup so that the computational time for a simulation of a reversed Faraday probe should be comparable to the time previously

Table 6.2: Time profile results of the multigrid hybrid fluid PIC computational code.

Routine	SG Time, s	MG Time, s	MG Time, %	Expected Speedup	Actual Speedup
accelerate	10,645.00	2,634.00	10.42	4	4.04
weight_to_grid	8,590.00	1,218.20	4.82	4	7.05
sample	8,475.00	1,048.90	4.15	4	8.08
move	6,570.46	941.15	3.72	4	6.98
e_energy	6,302.90	5,729.00	22.66	1	1.10
thomas_adi	4,855.80	4,461.80	17.65	1	1.09
e_poisson	4,362.23	4,037.85	15.97	1	1.08
e_momentum	3,866.20	3,555.90	14.07	1	1.09
e_continuity	1,395.50	1,277.90	5.06	1	1.09
collide	687.87	141.40	0.56	4	4.86
others	399.90	232.04	0.92	1	1.72
Total	56,151.06	25,278.14	100.00	1.88	2.22

required for a Faraday probe simulation.

Chapter VII

Reversed Faraday Probe Simulations

The multigrid version of the hybrid fluid PIC simulation code is used to simulate the axisymmetric flow around a reversed Faraday probe, with emphasis on resolving flow features on the wake side of the probe. For these cases the planar Bohm sheath solution will not be useful, since it cannot provide a stable sheath solution for ions flowing away from the probe surface. The geometric shadowing model solution could be useful for comparison with the simulation results, provided an estimate of the exchange frequency can be found to determine a physical scaling.

A geometric shadowing DSMC model will be developed by modifying the hybrid fluid PIC model to reproduce the assumptions of the geometric shadowing model. The resulting model is then used to perform a gasdynamic simulation of the ion particles. The shadowing DSMC model does produce a flow field that is consistent with the expectations of the shadowing model. However, no satisfactory geometric shadowing sheath solution can be found to fit the ion number density profile from the simulation.

The Boltzmann fluid model is used in the hybrid fluid PIC model to perform a plasmadynamic simulation of the same flow that includes electric fields. This flow field solution is significantly more complex than predicted by the shadowing model. Two dimensional effects introduce important flow features on the wake side of the probe that cannot be described by a one dimensional theory. The geometric shadowing sheath model is of little or no use in this situation.

The Poisson-consistent detailed fluid model is also used to simulate the flow. Minor differences from the Boltzmann model are noted, but generally the models are in good agreement. The Poisson-consistent model predicts more gradual plasma potential variation over a larger area than the Boltzmann model, and the flow structures in the wake are affected accordingly. Again, the geometric shadowing sheath does not provide useful predictions of the flow.

The numerical simulations are used to calculate estimates of the exchange frequency by recording the rate that simulated particles cross into a region in the wake. The shadowing DSMC model demonstrates an approximately constant exchange frequency for particles moving into the wake, but a much lower, variable frequency for particles moving out of the wake. The Boltzmann and Poisson-consistent models produce more complicated profiles of exchange frequency, with strong variations due to the flow features. The assumption of a constant exchange frequency at all points in the sheath is very poor for these models.

7.1 Flow conditions

The flow conditions are selected to obtain an interesting physical situation that remains representative of the conditions in an EP plume, while maintaining a practical simulation time. The geometric shadowing model provides some guidance about the properties of the sheath on the wake side of the probe. In Eq. 7.1 the solution for the distribution function in the wake region is repeated. Since the sheath length is defined where the exponential term is arbitrarily small, the sheath will extend far downstream if the Mach number is large.

$$f\left(z,M\right)=f_{\infty}\left(M\right)\left[1-\mathrm{H}\left(M\right)\exp\left(-\frac{W}{M}z\right)\right] \tag{7.1}$$

In the interest of keeping a smaller computational domain and limiting the time requirement, the flow should be kept near a Mach number of one. The electron temperature is assumed to be 11,600 K as in the previous conditions, which gives a Bohm velocity $v_B = 857.2\,\frac{\mathrm{m}}{\mathrm{s}}$. This suggests a drift velocity $v_D = 1000\,\frac{m}{s}$ giving a Mach number with respect to Bohm velocity of $M_D = 1.167$.

To match the cold ion case that was used repeatedly as a validation case, the number density is set at $n_i = 1.1 \times 10^{14}\,\mathrm{m}^{-3}$, although the ion number density does not appear as a parameter in the shadowing model. The ion temperature is set at $T_i = 300\,\mathrm{K}$, which determines the temperature ratio for the shadowing model as $\tau_{\infty} = 0.0259$. The low ion temperature avoids a significant backflow component, which can be demonstrated from the gaskinetic Mach number. The acoustic speed is calculated as $v_a = \sqrt{\gamma k_B T_i / m_i}$, giving $v_a = 178.0\,\frac{\mathrm{m}}{\mathrm{s}}$ for xenon at 300 K. This produces a strongly supersonic Mach number $M_{D,a} = 5.619$.

The flow conditions and model parameters for the ions are summarized in Table 7.1. For the hybrid fluid PIC models, it will be necessary to have conditions for the electrons at the inlet as well. The plasma is assumed to be co-flowing and neutral, so that $n_i = n_e$ and $v_i = v_e$ in the freestream.

Table 7.1: Ion plasma properties for reversed Faraday probe simulations.

$v_D = 1,000.\,\frac{\mathrm{m}}{\mathrm{s}}$	$n_i = 1.1 \times 10^{14}\,\mathrm{m}^{-3}$
$v_B = 855.7\,\frac{\mathrm{m}}{\mathrm{s}}$	$M_D = 1.167$
$T_i = 300\,\mathrm{K}$	$\tau_{\infty} = 0.0259$
$v_a = 178.0\,\frac{\mathrm{m}}{\mathrm{s}}$	$M_{D,a} = 5.619$

7.2 Simulation domain and numerical parameters

The computational domain for the reversed Faraday probe is similar to that used for the probe simulations. In this case, the extent of the domain on the wake side of the probe is estimated using a kinetic argument. The boundary conditions are essentially unchanged. Since the reversed Faraday probe simulations are conducted with a multigrid method, numerical parameters for the computational grid must satisfy the more demanding requirements.

7.2.1 Computational domain

The geometric shadowing model does not provide a physically scaled solution, so no sheath length is available to give the required domain length. Instead, a kinetic argument is used to size the domain on the wake side of the probe.

Ion particles at a sufficiently large initial radius will flow past the side of the probe body and diffuse into the wake region. Electrostatic fields tend to accelerate particles toward the centerline on the wake side of the probe, so the electric field is neglected to arrive at a conservative estimate of the domain length. Without electric fields, radial diffusion is due to random thermal velocity of the particles.

To fully resolve the wake, the domain should be long enough for particles of every radial speed to diffuse across the diameter of the probe. Since there are particles with very low radial speed, this still results in a domain that is impractically long. Instead, consider the fastest particles to be at three times the mean speed. For xenon at 300 K, these particles have a radial speed of $v_{r,max} = 660\,\frac{\mathrm{m}}{\mathrm{s}}$.

The streamline for a particle that just passes the edge of the probe with the maximum radial speed gives the geometry in Fig. 7.1. From this geometry, it can be determined that the domain must extend at least 1.52 probe diameters downstream

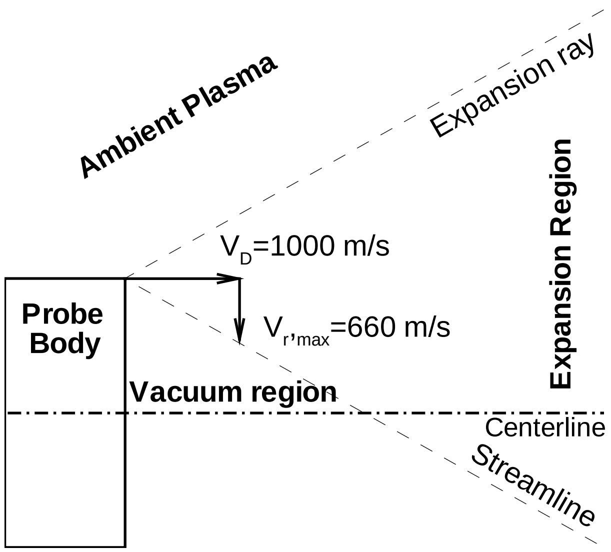

Figure 7.1: Schematic of the wake behind a reversed Faraday probe, with the leading expansion ray and the streamline for particles with the fastest radial speed.

for these particles to diffuse across the diameter of the probe. No particles diffuse from the vacuum region of the wake into the ambient plasma, so an expansion region extends into the plasma as indicated by the dashed streamline for the imaginary particle flowing outward at the maximum radial speed. By symmetry, this streamline reaches a radius of 1.5 diameters at the minimum domain length, giving the radial extent of the domain.

The simulation domain will be extended 20% farther downstream to allow some particles with lower radial speed to diffuse completely across the probe. The final simulation geometry is shown in Fig. 7.2, dimensioned in terms of the probe diameter and the physical dimensions of the JPL Faraday probe. A region of flow upstream and alongside of the probe is simulated to obtain consistent ambient conditions on the wake side of the probe.

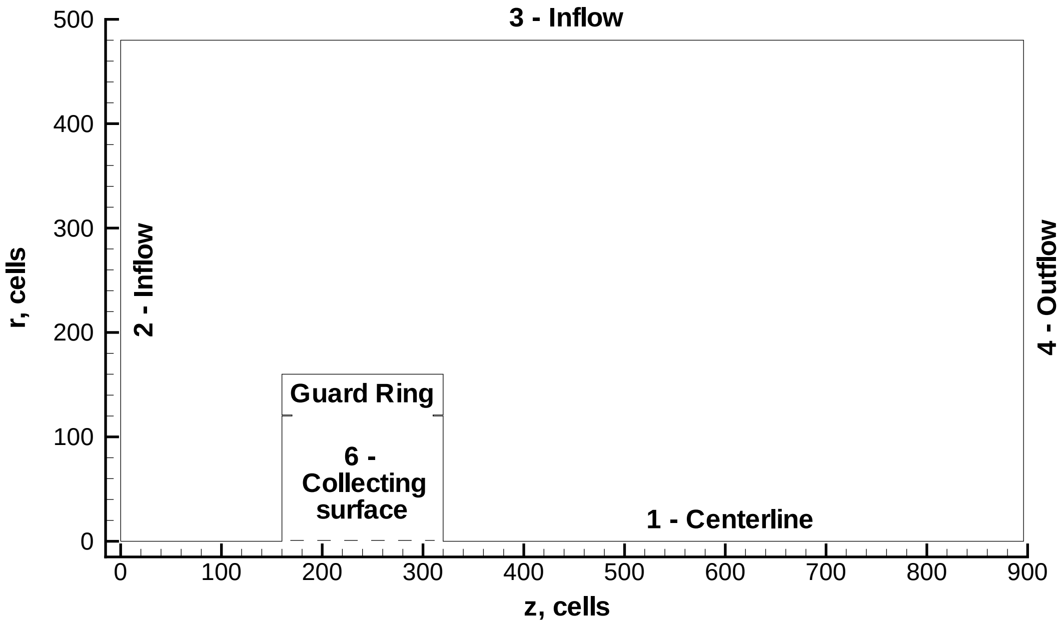

Figure 7.2: Computational domain for reversed Faraday probe simulations.

7.2.2 Computational grid

Since this flow will be simulated with the multigrid version of the hybrid fluid PIC code, two computational grids are required. The fluid grid is developed first and the PIC grid is then constructed using every second node of the fluid grid. This ensures that each PIC cell contains exactly four fluid cells, and that each PIC grid node is coincident with a fluid grid node.

The rectangular cells of the fluid grid are uniformly sized at 8×10^{-5} m on a side. The final geometry extends 7.168 cm (896 cells) along the probe axis and 3.840 cm (480 cells) radially. The probe body is 1.280 cm (160 cells) long with 0.96 cm (120 elements) along the collecting surface and 0.320 cm (40 elements) along the guard ring surface. The front surface of the probe is 1.28 cm (160 cells) from the upstream inlet of the domain, and the back surface of the probe is 4.608 cm (576 cells) from the downstream exit of the domain. Altogether there are 404,480 fluid cells outside of the probe body.

The PIC cells are then 1.6×10^{-4} m on a side, and the domain has 448 cells along the probe axis and 240 cells radially. The probe body is 80 cells long, with 60 cells along the collecting surface of the probe and 20 elements along the guard ring. Altogether there are 101,120 PIC cells outside of the probe body. Note that the number of PIC cells is actually slightly smaller than in the original Faraday probe simulations. At steady state, there are approximately 1.7 million particles in the domain.

The simulation time step is selected so that the fastest ions travel less than one cell length per iteration. Assuming a probe potential of -5 V, ions that enter at twice the thermal speed beyond the drift velocity arrive at the probe with a velocity of $3,070 \ \frac{\mathrm{m}}{\mathrm{s}}$. Dividing the cell length by this speed and rounding down sets the time step at 5×10^{-8} s.

The simulation is allowed to iterate for 10,000 time steps to reach a converged state, followed by 20,000 sampled time steps. The total simulation time is approximately 45 hours. The performance gain of using multigrid is in full evidence: this domain has 3.6 times the number of fluid cells in the Faraday probe domain, but requires just 30% more computational time.

7.2.3 Boundary conditions

The boundary conditions on this domain are identical to the conditions on the Faraday probe simulations. Referring to the labels in Fig. 7.2, there are six regions of boundary conditions that are repeated here.

Region 1 is the axisymmetric centerline. Particles are automatically rotated at the centerline as part of the axisymmetric move routine. A zero gradient condition is enforced on the radial component of all variables in the fluid models, including the stream function Ψ, plasma potential, electron number density, and electron temperature.

Region 2 is the upstream inlet for the flow. Particles are introduced at this boundary with a random position and statistically sampled velocity in each cell. Particles that cross this boundary are removed from the simulation. The electron temperature and gradient of stream function are assigned along this edge. The plasma potential and electron number density are set using third kind boundary conditions.

Region 3 is the outer radial inlet. Particles are injected along this edge using the same procedure as in Region 2, and particles that cross this boundary are removed from the simulation. A constant gradient condition is enforced on the radial component of the stream function, and zero gradient conditions are enforced on the radial component of plasma potential, electron number density, and electron temperature.

Region 4 is the downstream flow exit. Particles are only removed along this edge, since the Maxwellian distribution for the ions has negligible backflow. The gaskinetic Mach number is strongly supersonic, further reinforcing this point. A constant gradient condition is enforced on the stream function, and zero gradient conditions are enforced on the axial component of plasma potential, electron number density, and electron temperature.

Region 5 includes the guard ring and side body of the probe. Particles undergo diffuse reflection from this surface with full thermal accommodation, and ion particles are neutralized. The gradient of stream function is assigned, which is equivalent to specifying the electron current flux to the surface. The plasma potential, electron number density, and electron temperature are assigned at the surface. In keeping with experimental practice, the entire side of the probe body is biased to the same potential as the collecting surface.

Region 6 is the collecting surface of the probe. The same boundary conditions as in Region 5 are enforced on particles and electron fluid variables. When ion particles are neutralized at this surface, the collected current is incremented by the charge of the ion particle. This gives the simulated collected current, which is averaged over the sampling time steps.

7.3 Geometric shadowing DSMC model

The geometric shadowing model assumes zero electric fields and plasma neutrality, so several of the hybrid fluid PIC model capabilities must be deactivated to obtain an equivalent computational model. The neutrality condition allows the electron fluid equations for continuity, momentum, and energy to be disabled. The assumption of zero electric fields allows the electrostatic Poisson equation to be disabled, and removes the need to calculate electrostatic acceleration on the particles.

The remaining computational code is just a DSMC model for the ion particles, since all of the fluid model equations and PIC electric field routines are disabled. This model performs purely gaskinetic simulations. However, these simulations should most closely reproduce the sheath solution from the geometric shadowing model.

Contours of simulated ion number density are shown in Fig. 7.3. The flow structure reflects the assumptions used to size the domain. A vacuum region is formed immediately behind the probe. Particles at the outer edge of the probe diffuse toward the centerline, and the expansion spreads into the freestream flow beyond the probe radius. The flow rejoins smoothly at the centerline, increasing from vacuum to

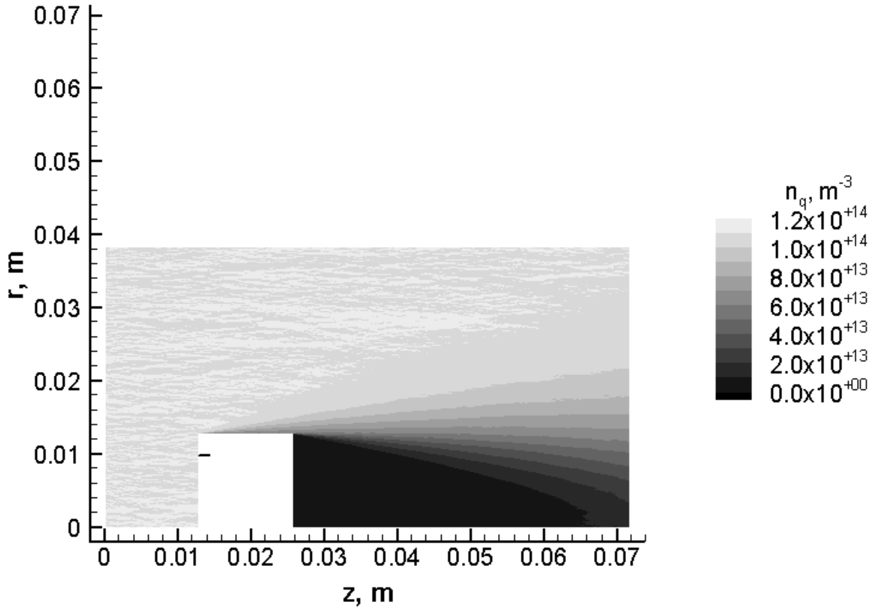

Figure 7.3: Contours of ion density for the reversed Faraday probe case.

the freestream density. No overcompression region develops, since there is no force to accelerate particles toward the centerline.

A radial average of properties near the centerline does not provide a useful comparison with the geometric shadowing sheath model in the wake region of the flow, since the shadowing sheath model cannot predict the vacuum region. Instead, the cylindrical surface at the outer diameter of the probe is a fair representation of the situation in one dimension. Profiles of ion density at a radius equal to the outer edge of the probe cylinder are shown in Fig. 7.4. Since there has been no radial averaging, the statistical scatter in the profile is readily evident.

The exchange frequency is not known *a priori* to calculate the shadowing sheath in physical dimensions, so a least-squares method is used to seek an exchange frequency that provides the best fit. However, there is not a satisfactory fit using a single value of exchange frequency. This result is not unreasonable, since the Maxwellian

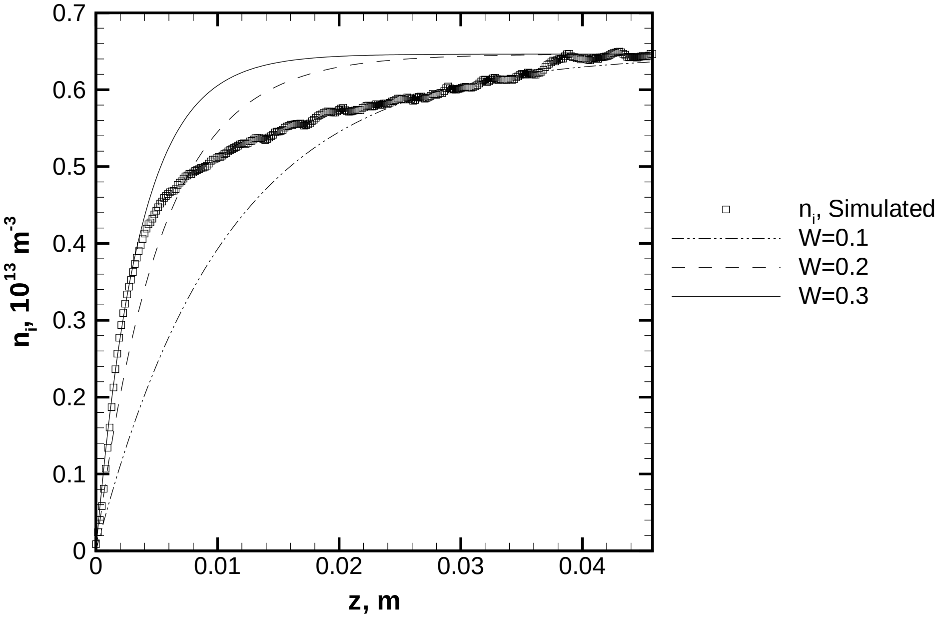

Figure 7.4: Profiles of ion number density at the outer edge of the probe.

distribution of radial speeds in the simulation leads to different transport rates at different radial speeds. Essentially the exchange frequency has a functional dependence on radial speed in the simulation, while the shadowing sheath assumes a constant exchange frequency.

Streamlines of current are shown in Fig. 7.5. The vacuum region behind the probe is clearly delineated, and extends approximately 2 cm ($28\,\lambda_D$) along the centerline. Tracing the streamlines that expand into the wake region backward, it is seen that much of the wake flow originates in a thin annulus immediately surrounding the probe cylinder.

Although the shadowing DSMC numerical model reproduces the assumptions of the shadowing sheath model, there are significant differences in the calculated sheath properties. The one dimensional formulation does not predict a vacuum region, so the shadowing sheath model is not directly applicable except at the outer edge of the

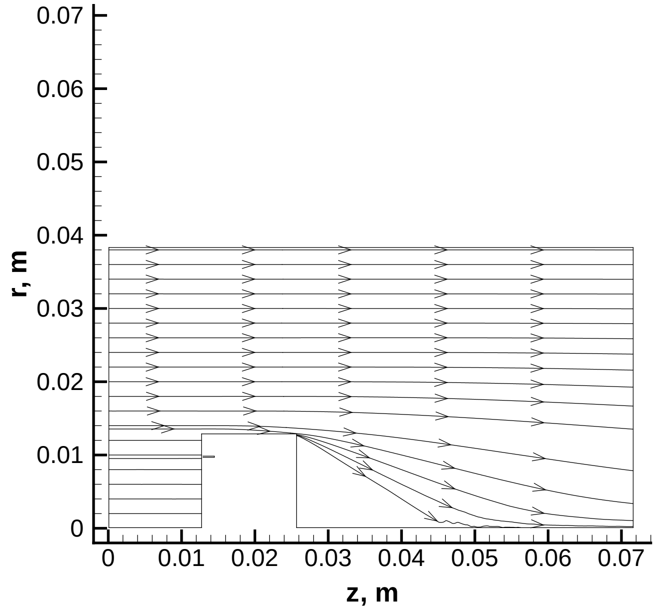

Figure 7.5: Streamlines of current for the reversed Faraday probe case.

probe. Even there, the sheath model cannot be brought into good agreement with the simulation. In the DSMC simulation the particle velocity distribution leads to a variable exchange frequency, which is oversimplified to a constant in the shadowing sheath model.

The shadowing sheath model does a poor job of predicting the sheath properties on the wake side of the probe for the shadowing DSMC simulation, so it is unlikely to be a useful predictor for the hybrid fluid PIC simulations.

7.4 Hybrid PIC Boltzmann model

In terms of simulating a plasma, the hybrid fluid PIC models represent a large step up from the shadowing DSMC model. The single most important difference is the inclusion of electrostatic fields. Plasmas are distinguished from gases primarily by the electrical charge of the particles, and the associated interactions with electric and magnetic fields. It should come as no surprise then, that results from the hybrid

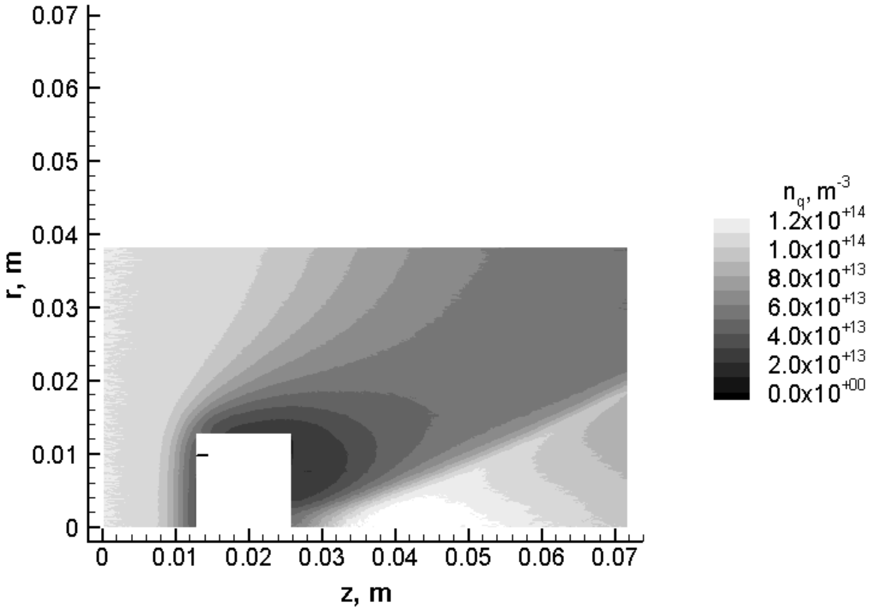

Figure 7.6: Contours of ion density for the reversed Faraday probe case.

models show distinctly different flow features from the DSMC simulation results.

Contours of ion number density calculated with the hybrid PIC Boltzmann fluid model are shown in Fig. 7.6. The wake structure is complicated, and differs from the DSMC simulation results in three main features. First, the electrostatic sheath causes a region of decreased density upstream of the probe and alongside the probe body. Second, the flow expands to a low density in the immediate wake of the probe, but does not develop a vacuum region. Third, a conical overcompression region forms slightly downstream of the probe surface.

The contours of electron number density in Fig. 7.7 can be compared with the ion number density contours to give a rough impression that the flow throughout most of the domain is nearly neutral. The electron number density only varies significantly from the ion number density near the probe surfaces. These contours appear noisy since the Boltzmann relation is used to calculate the electron number density from

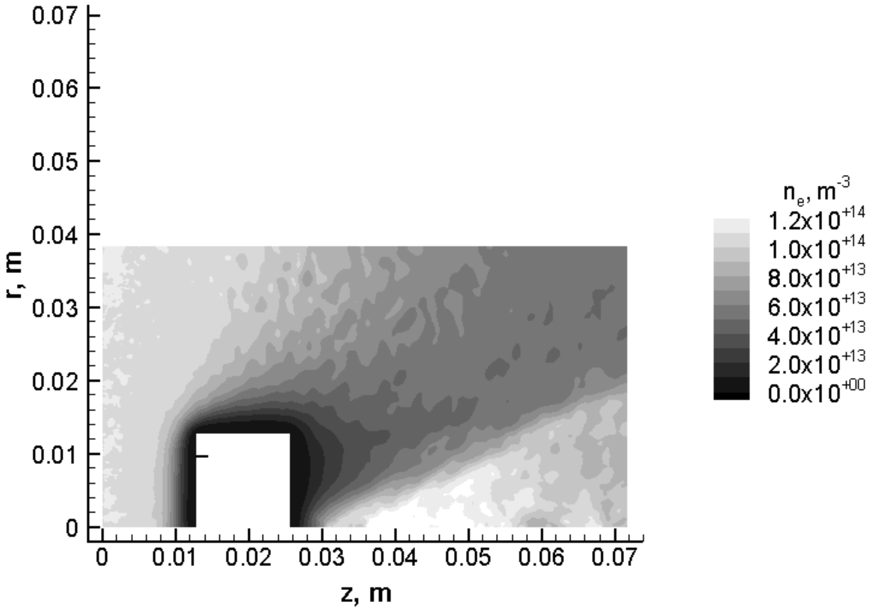

Figure 7.7: Contours of electron density for the reversed Faraday probe case.

the plasma potential. The exponential relation magnifies small variations in plasma potential to much larger variations in electron number density.

The complicated features in the ion flow field can be explained by the electrostatic sheaths along the probe surfaces, which alter the ion trajectories significantly. The contours of plasma potential in Fig. 7.8 and the current streamlines in Fig. 7.9 are useful for illustrating the explanations.

The first difference is in the regions of decreased density upstream of the probe and extending outward radially from the side of the probe. The behavior upstream of the probe is familiar from the Faraday probe simulations in Chapter V. As the plasma potential drops near the front face of the probe, ions are accelerated toward the probe and the density falls. The same process acts along the side of the probe, except that the freestream flow is initially parallel to the surface and the electrostatic acceleration turns ions toward the probe. The flow farther from the probe surface is

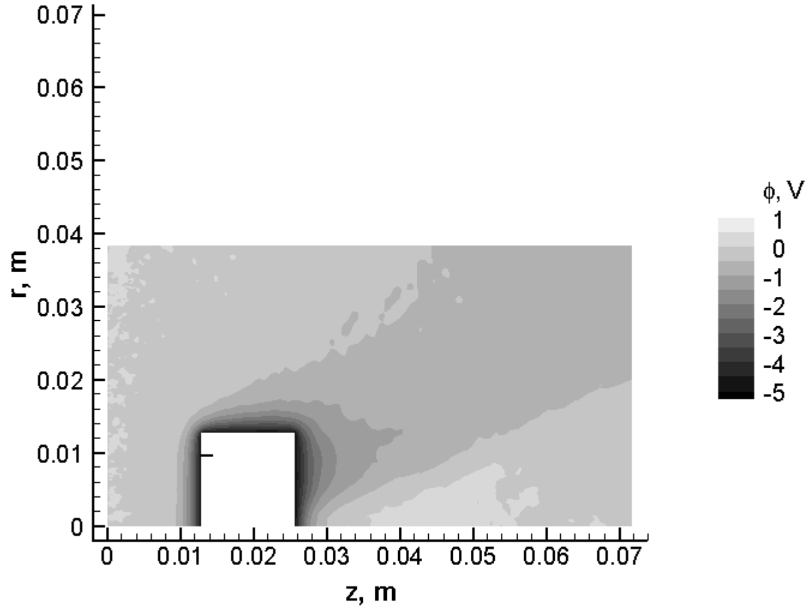

Figure 7.8: Contours of plasma potential for the reversed Faraday probe case.

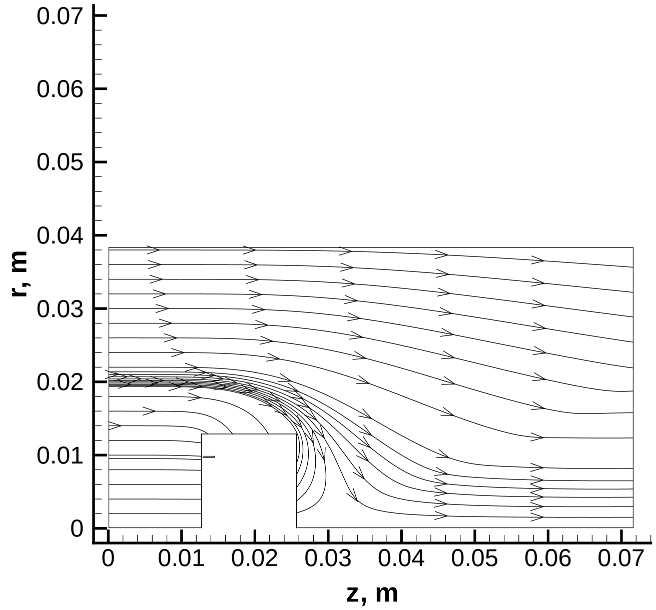

Figure 7.9: Streamlines of current for the reversed Faraday probe case.

shielded from the potential drop, but expands toward the centerline in response to the density gradient closer to the probe.

The second difference is in the wake region immediately behind the probe. As seen in the streamlines, the flow that arrives in this region has been turned by passing through the sheath on the side of the probe. This flow has a larger average radial speed than in the DSMC simulation, and the electric fields in the wake-side sheath act to turn the ions toward the rear face of the probe. Together these effects are sufficient to turn the flow completely around the corner of the probe without forming a vacuum region.

The third difference is the conical overcompression region downstream of the probe. The flow that reaches the area immediately behind the probe has been turned by passing through the sheath alongside the probe body, and then expanded toward the centerline when the adjacent flow was turned toward the rear face of the probe. This results in a radially converging flow that comes to a stagnation point approximately 0.6 cm ($8.5\,\lambda_D$) downstream of the probe. Moving downstream, the flow that was expanded from alongside the probe converges toward the centerline and compresses the flow there. Meanwhile, the flow near the centerline expands along the axis.

The ion number density profile at the outer edge of the probe in Fig. 7.10 reflects the complicated structure of the wake. Ion number density near the probe surface, from 2.56 cm to 2.76 cm, is approximately constant at 2.4×10^{13} m^{-3}. In that region the flow is uniformly expanded and is essentially parallel to the rear face of the probe. From 2.76 cm to about 5.4 cm, the ion number density shows a gradual increase that corresponds to moving across the expansion to a higher density region. The number density then increases more quickly, which corresponds to moving across

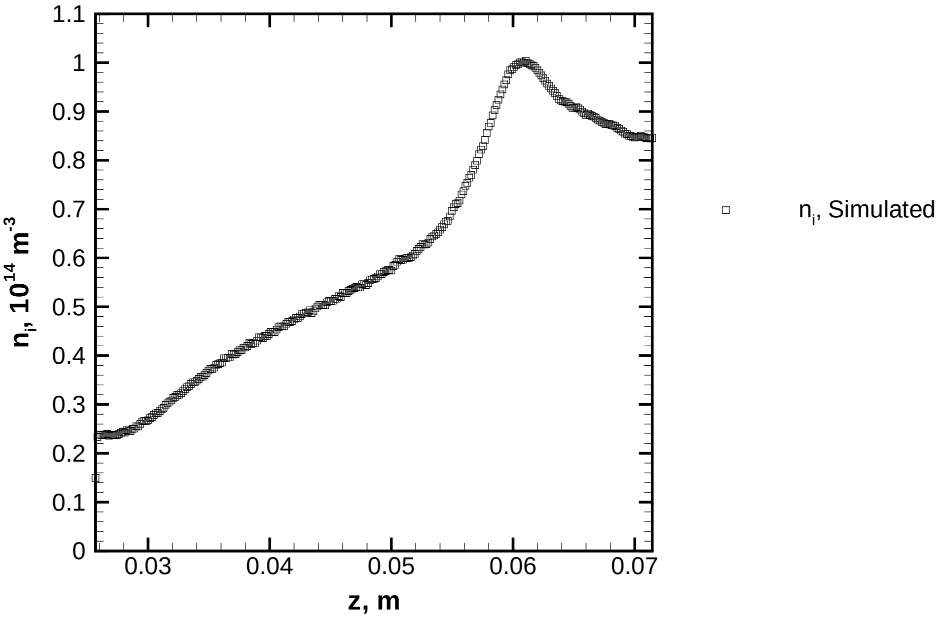

Figure 7.10: Profiles of ion number density at the outer edge of the probe.

the compression region. The peak density of $1.0 \times 10^{14}\,\mathrm{m}^{-3}$ is reached at 6.2 cm, and beyond that point the expansion along the axis causes the number density to begin decreasing again.

It should be noted that the particulars of the ion density profile are not unique. The radius of the probe, the bias potential on the probe, and the ratio of ion drift velocity to thermal velocity all contribute to the shape of this profile. The downstream location and magnitude of the maximum ion density depend strongly on the radius of the probe and how effectively the electrostatic sheath focuses the flow toward the centerline. However, the qualitative properties of the profile are expected to be consistent for similar flow geometries.

The ion number density profile is not consistent with the exponential form expected in the geometric shadowing sheath model, so no attempt is made to fit this profile with a shadowing sheath solution. This upholds the expectation that the shadowing sheath model would not be a useful predictor for the sheath properties on the wake side of the probe.

7.5 Hybrid PIC Poisson-consistent detailed model

The main difference between the Poisson-consistent detailed model and the Boltzmann model is that the Poisson-consistent model solves the all three electron fluid conservation laws. Recall from Chapter V that the differences between the model results are small for the Faraday probe simulations. Not surprisingly, simulation of the reversed Faraday probe using the hybrid PIC Poisson-consistent model yields results that are very similar to the Boltzmann model results.

The main structures of the wake are shown in the contours of ion number density in Fig. 7.11. As seen previously, there is a region of decreased density alongside and upstream of the probe body. Immediately behind the probe is a low density region, and an overcompression region farther downstream. Comparing the ion number density with the contours of electron number density in Fig. 7.12, it appears that the flow is still nearly neutral except within a few Debye lengths of the probe surfaces.

There are two related minor differences from the contours calculated in the Boltzmann model simulations. The first is that the low density region along the side of the probe body extends almost radially from the front of the probe, where it was swept back from the front surface in the Boltzmann simulation results. The second difference is that the overcompression region in these results forms a cone with a smaller half-angle and a lower peak number density than in the Boltzmann simulation.

The first difference can be explained by the curvature of the plasma potential contours in Fig. 7.13, which is less pronounced than in the Boltzmann model results. The gradients in plasma potential extend farther into the plasma in the Poisson-

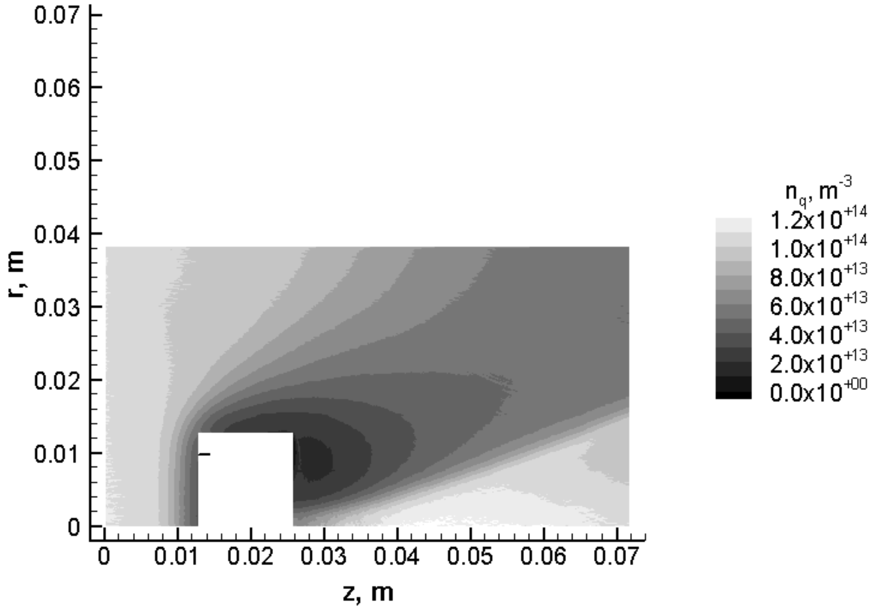

Figure 7.11: Contours of ion density for the reversed Faraday probe case.

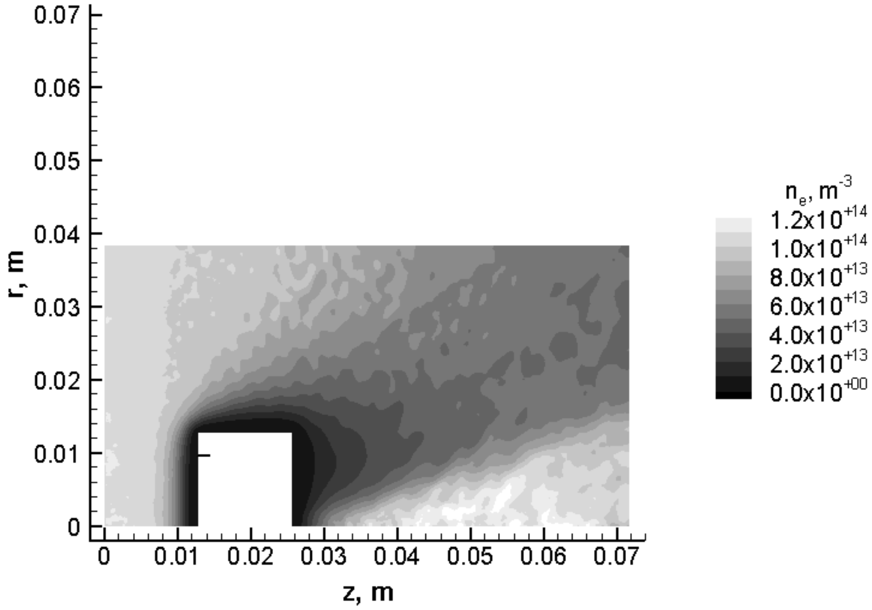

Figure 7.12: Contours of electron density for the reversed Faraday probe case.

consistent simulation, so weak electric fields affect more of the flow. In this case the electrostatic acceleration produces a component of acceleration along the flow direction as well as a component of expansion toward the centerline. This is visible in Fig. 7.14 as a less pronounced focusing of the current streamlines near the front surface of the probe.

The gradients in plasma potential are smaller than in the Boltzmann simulation, so the electric fields are weaker in the Poisson-consistent simulation. Since this generates a smaller force and the flow also develops a higher axial velocity, the flow does not turn around the edge of the probe as quickly. This leads to a region of lower density immediately behind the probe, and a generally lower potential in the wake region behind the probe. When the flow converges on the centerline in the Poisson-consistent simulation, the higher axial speed carries particles downstream faster. This reduces the particle residence time, which decreases the peak number density and narrows the cone of the overcompression region. This process explains the second difference in the simulation results.

The profile of ion number density at the outer edge of the probe in Fig. 7.15 shows the same trends as described for the Boltzmann model simulation. The ion number density is constant at approximately $2.0 \times 10^{13}\,\mathrm{m}^{-3}$ near the face of the probe, from 2.56 cm to 2.8 cm. The ion number density then increases gradually across the expansion until the edge of the compression region, which has moved downstream to 6.0 cm. Across the compression region the ion number density rises to a maximum of $8.6 \times 10^{13}\ \mathrm{m}^{-3}$ at 6.9 cm, before beginning to decrease as the flow accelerates downstream.

This profile is also incompatible with the geometric shadowing sheath model, so no attempt to fit a shadowing sheath is made. There is qualitative agreement between

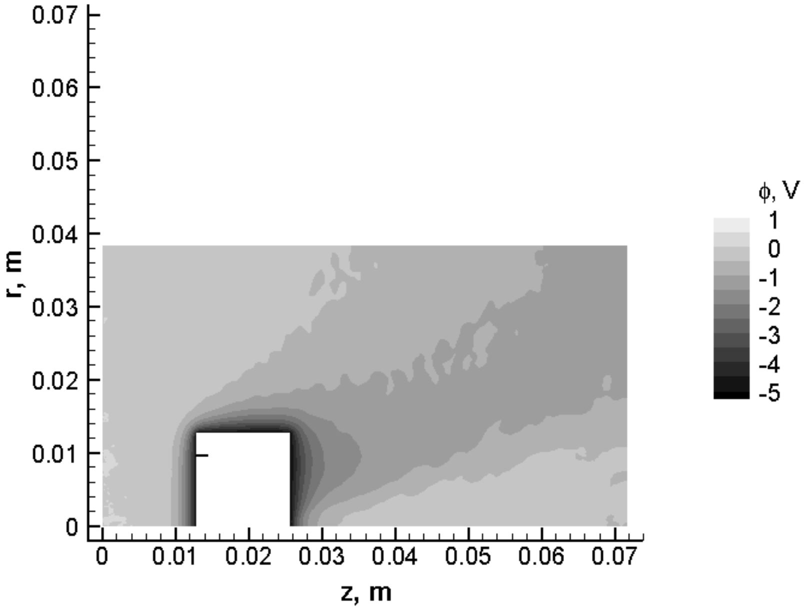

Figure 7.13: Contours of potential for the reversed Faraday probe case.

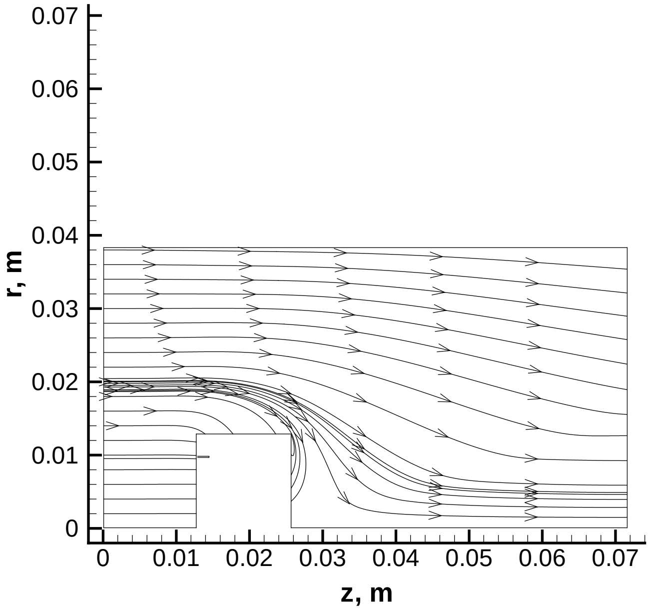

Figure 7.14: Streamlines of current for the reversed Faraday probe case.

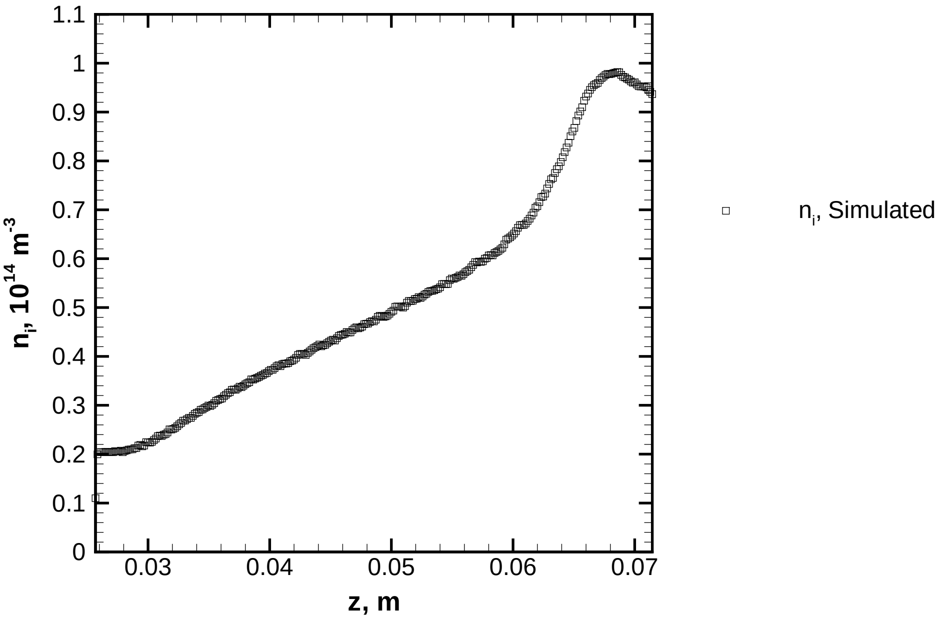

Figure 7.15: Profiles of ion number density at the outer edge of the probe.

the results from the Boltzmann model simulation and the Poisson-consistent model, but the values of number density or plasma potential at a point in the flow vary by 10-15% between the simulations. The minor differences between the electron fluid models become more significant over the extended sheath on the wake side of the probe.

7.6 Exchange frequency results

The hybrid fluid PIC models can also be used to obtain an estimate of the exchange frequency for use in the geometric shadowing sheath model. Since the models simulate particles rather than the particle distribution functions, it is useful to relate the exchange frequency to a more easily calculated property.

The source term in the shadowing sheath model resembles a rate of change of the local distribution function, as in Eq. 7.2. There is no difficulty in integrating over all velocities to obtain the source term for ion number density in Eq. 7.3, since the exchange frequency is assumed to be constant.

$$\frac{df}{dt} = w\left(f_\infty - f\right) \tag{7.2}$$

$$\int_v n_\infty \frac{df}{dt} dv = \int_v n_\infty w\left(f_\infty - f\right) dv \longrightarrow \frac{dn}{dt} = w\left(n_\infty - n\right) \tag{7.3}$$

The numerical models operate on a discrete computational grid, so it is useful to integrate over the volume of the cell as in Eq. 7.4 to obtain the rate of change of particle count in the cell.

$$\int_V \frac{dn}{dt} dV = \int_V w\left(n_\infty - n\right) dV \longrightarrow \frac{dN}{dt} = w\left(N_\infty - N\right) \tag{7.4}$$

The source term can be readily divided into separate terms for the addition and removal of particles from the cell, giving the form in Eq. 7.5. The forms in Eq. 7.6 can be used to calculate the exchange frequencies w_{in} for particle addition and w_{out} for particle removal, based on the particle count and the transfer rate.

$$\left.\frac{dN}{dt}\right|_{in} - \left.\frac{dN}{dt}\right|_{out} = w_{in} N_\infty - w_{out} N \tag{7.5}$$

$$w_{in} = \frac{1}{N_\infty} \left.\frac{dN}{dt}\right|_{in} \qquad w_{out} = \frac{1}{N} \left.\frac{dN}{dt}\right|_{out} \tag{7.6}$$

In the numerical simulations, every time an ion macroparticle crosses in to or out of the cylinder downstream of the outer edge of the probe, an event counter is incremented. Multiplying the number of events by the macroparticle weight and dividing by the total simulation time gives the average transfer rates $\frac{dN}{dt}$. Profiles of the normalized exchange frequencies are shown in Figs. 7.16-7.18 for all three of the numerical models. Particle exchange is relatively rare in the shadowing DSMC model, so the profiles for that model show larger statistical scatter than the Boltzmann or Poisson-consistent model profiles.

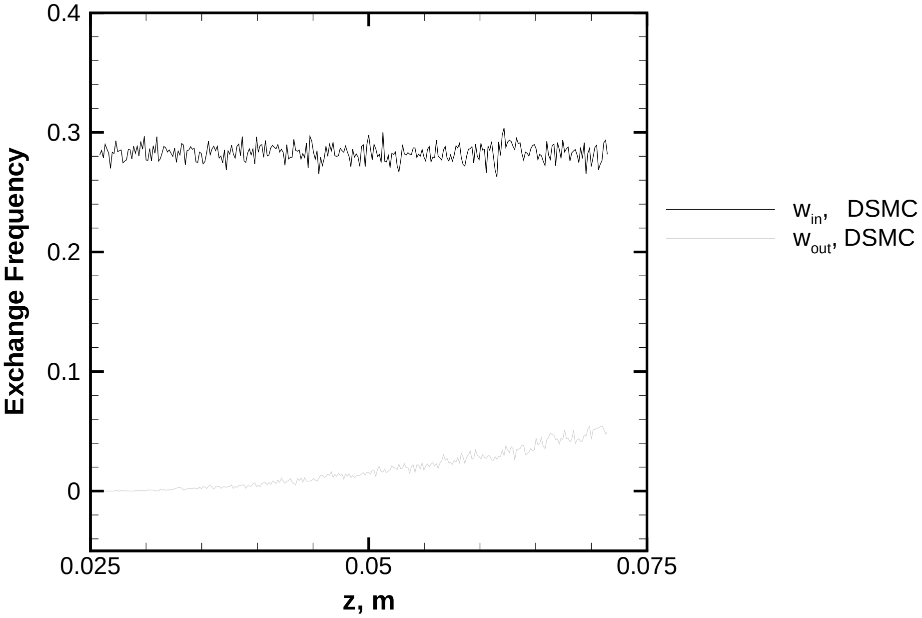

Figure 7.16: Profiles of simulated exchange frequency calculated using the shadowing DSMC model.

The profiles from the shadowing DSMC model are closest to the assumptions made in the geometric shadowing sheath model. The exchange frequency for particles moving into the cylinder is essentially constant, averaging near $w_{in} = 0.29$. This corresponds very well with the $w = 0.3$ value calculated in Sec. 7.3 to fit the ion number density profile near the surface. The exchange frequency for particles moving out of the cylinder is much lower and shows a distinct trend. This is a departure from the geometric shadowing sheath assumption, and helps to explain why no satisfactory fit value could be found previously.

The exchange frequency profiles for the Boltzmann model and the Poisson-consistent model are very similar. The exchange frequency into the cylinder immediately downstream of the probe is very high, since the flow has turned around the edge of the probe and is directed into the cylinder. Moving farther downstream, the exchange frequency drops to a plateau where the flow is expanding toward the centerline. Since

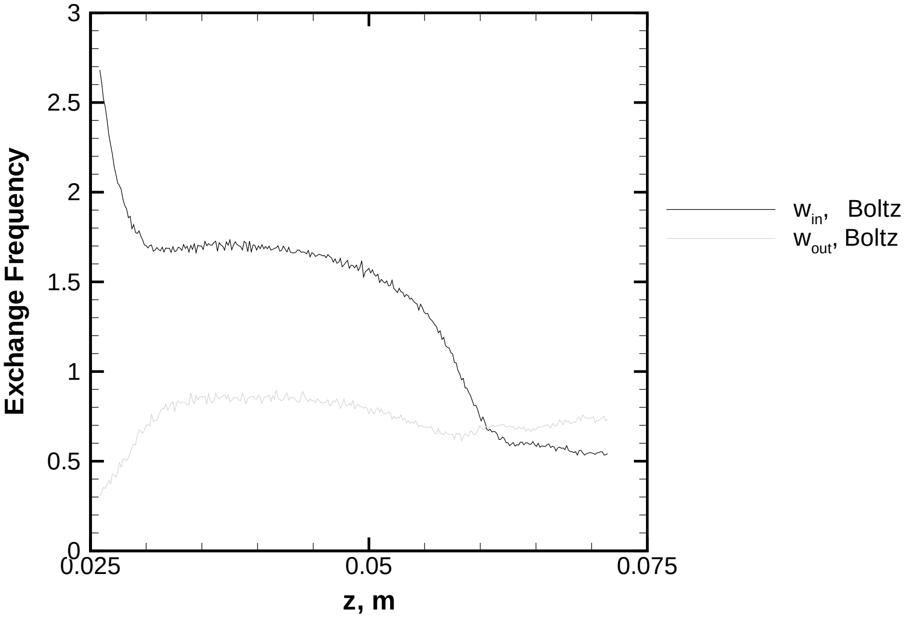

Figure 7.17: Profiles of simulated exchange frequency calculated using the Boltzmann model.

the radial speed is lower, the exchange frequencies into and out of the cylinder are closer together. The onset of the overcompression region appears as a second drop in the exchange frequency into the cylinder. Eventually the exchange frequency out of the cylinder becomes larger than the exchange frequency in to the cylinder, indicating the expansion along the axis. The exchange frequency into the cylinder levels off to a second plateau in the expansion.

Again, the assumptions that the exchange frequency is constant and equal for transfer in to and out of the cylinder are not appropriate for these profiles. The exchange frequency shows so much variation that no estimate is likely to produce a geometric shadowing sheath solution that resembles the observed ion number density profiles.

These results can still be used to make order of magnitude estimates of the exchange frequency for the gasdynamic and plasmadynamic cases. The gasdynamic

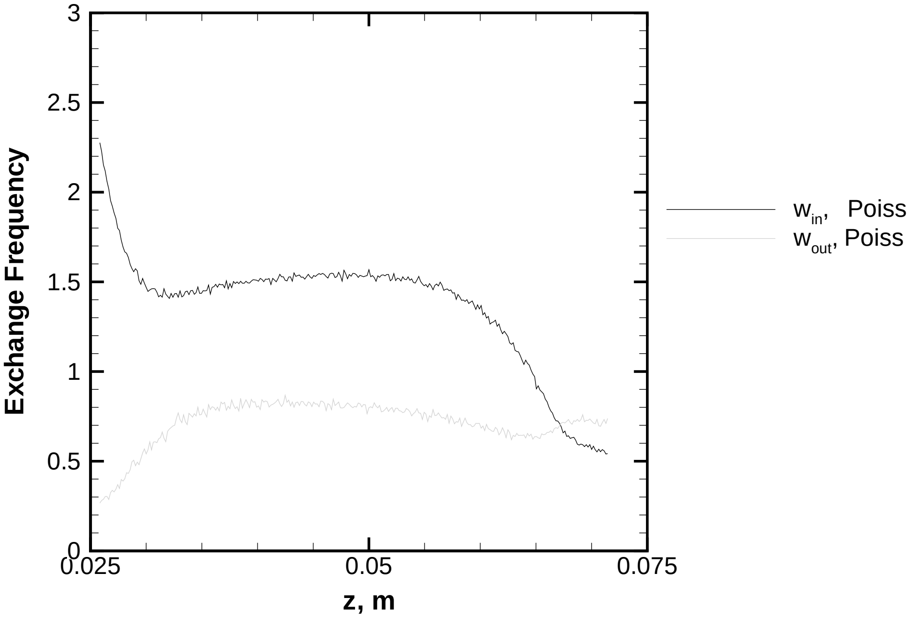

Figure 7.18: Profiles of simulated exchange frequency calculated using the Poisson-consistent model.

case in the DSMC model simulation shows a nearly constant, relatively low exchange frequency into the cylinder, on the order of $w = 0.3$. The exchange frequency out of the cylinder is zero near the surface of the probe and slowly rises as the wake is filled in. The plasmadynamic cases in the Boltzmann and Poisson-consistent simulations show a relationship between the flow orientation and the exchange frequency. The exchange frequency can become very large if the direction of flow is normal to the surface. If the flow is primarily parallel to the sheath, the exchange frequency shows a range of $w = 1.4 - 1.8$ for expansion into the sheath and a range of $w = 0.5 - 0.6$ for expansion out of the sheath in the overcompression region.

7.7 Conclusions for model usage and probe design

Simulations of the reversed Faraday probe with the shadowing DSMC model, the hybrid Boltzmann model, and the hybrid Poisson-consistent model are not in good agreement with the geometric shadowing sheath solution. The calculated exchange frequencies show significant variation and cannot be represented well by a constant value. Additionally, the number density in the wake is very low, so the exchange frequency out of the probe is much smaller than the exchange frequency into the probe. These differences cannot be addressed without redeveloping the shadowing sheath model altogether.

The two dimensional effects are also a significant factor, introducing vacuum regions that the one dimensional shadowing sheath model cannot predict. Electrostatic acceleration helps develop a more uniform flow immediately downstream of the probe, since charged particles can turn around the edge of the probe to reach the rear face of the probe without forming a vacuum region. However, this accelerates the flow toward the axis and creates an overcompression region that is also beyond the predictive capabilities of the geometric shadowing sheath.

Electrostatic acceleration produces an extended expansion region alongside the probe, and leads to a compression region downstream of the probe. These effects are not predicted in the shadowing DSMC model, which illustrates the importance of the electric fields for accurate simulation of a plasma. The electric fields can also significantly alter the direction of the flow, and can completely reverse the direction of flow.

This may be an important consideration for a reversed Faraday probe use. The current streamlines from the Boltzmann and Poisson-consistent model simulations indicate that all of the current that reaches the rear face of the probe originates from an annular region at slightly larger radius than the probe. Obstructions off axis and upstream from the probe might not affect measurements on the upstream face, but could interfere with measurements on the reversed face of the probe. Features on the side of the probe body such as a mounting spar will certainly affect the flow to the rear face of the probe.

Chapter VIII

Conclusion

In this chapter the important results and conclusions described in the course of this dissertation are reviewed. In fulfillment of one of the major objectives of this work, a few recommendations are made regarding Faraday probe use.

8.1 Summary and Review

Standard diagnostic techniques assume that properties measured at the surface of a probe can be related directly to undisturbed plasma properties. However, an immersed Faraday probe affects the ambient plasma by introducing physical obstructions and electrostatic sheaths. Perturbations caused by the probe may lead to systematic differences between the probe measurements and the undisturbed plasma properties.

The work in this dissertation was intended to develop and use computational models to identify and quantify any differences caused by the presence of an immersed Faraday probe in a plasma. Both of these objectives have been accomplished, as is summarized in the following sections.

8.1.1 One dimensional analytic models

In order to obtain an initial understanding of the flow features in a plasma sheath, two analytical models were developed as reference cases in Chapter III. Both models were derived from very general kinetic or fluid descriptions of the plasma by assuming steady, collisionless, one dimensional flow.

The geometric shadowing sheath model was derived from kinetic theory and the Boltzmann transport equation in Sec. 3.2, with physical obstruction of particle trajectories causing variation of the plasma properties in the sheath. A diffusion-like source term was used to model the transfer of particles between the distribution function in the ambient plasma and the distribution function in the sheath. The rate of particle transfer was scaled by introducing an exchange frequency. An analytic solution was then obtained by neglecting the electric fields.

The shadowing sheath solution described an exponential depletion of the backflowing distribution as the flow approaches the probe. Moments of the local distribution could be calculated to obtain profiles of the ion number density and velocity in the sheath. However, this solution could not be scaled into physical dimensions unless a value of the exchange frequency could be estimated by some other means.

The planar Bohm sheath model was derived from fluid theory in Sec. 3.3, using the conservation equations for mass and energy of the ions and assuming the Boltzmann relation for the electrons. The electrostatic Poisson equation was then written as a differential equation for the plasma potential and integrated using a numerical method. It was noted that a steady solution was only possible if the ion drift velocity was greater than or equal to the Bohm velocity at the edge of the sheath. This condition is the Bohm criterion.

The Bohm sheath solution gave profiles of the plasma potential and the ion and electron number densities in the sheath. Since the sheath coordinate scaled with the Debye length, the Bohm sheath solution could be scaled into physical dimensions.

The one dimensional models were compared in Sec. 3.4 using conditions that achieved partial similarity. A shadowing sheath solution was calculated for a given freestream Mach number. The plasma potential in the shadowing sheath model was calculated by assuming neutrality and then assuming the Boltzmann relation, so that the plasma potential could be expressed as a function of the ion number density. A planar Bohm sheath solution was then calculated for the same freestream Mach number and plasma potential at the probe surface. A least-squares fit was performed on the ion number density profiles to estimate the value of the exchange frequency. The best fit was found with an exchange frequency $W = 0.088$, that is, the exchange frequency was 0.088 times the plasma frequency. However, it was noted that this value is specific to the conditions $M_D = 1$ and $\tau_\infty = 1$.

8.1.2 Two dimensional computational models

The axisymmetric hybrid fluid PIC models were described in Chapter IV. The large difference between the electron and ion time scales in a plasma was noted, and a hybrid model was employed that used kinetic models for the ions and neutrals and fluid models for the electrons.

The ions and neutrals were modeled using the well-known Particle In Cell (PIC) and Direct Simulation Monte Carlo (DSMC) methods as described in Sec. 4.1. Macroparticles were moved according to the electric fields calculated at nodes of the computational grid. Collisions were evaluated statistically in cells of the computational grid.

The electrons were modeled with one of three fluid models described in Sec. 4.2.

The first fluid model used the Boltzmann relation and solved the electrostatic Poisson equation for plasma potential. The Boltzmann fluid model closely approximated the assumptions of the planar Bohm sheath model.

The second fluid model was the non-neutral detailed model. This model solved all three of the fluid conservation equations and the electrostatic Poisson equation. The electron momentum equation was solved for plasma potential in this model, leaving only the electrostatic Poisson equation to solve for electron number density. The calculation for electron density was found to have poor resolution and high sensitivity to statistical scatter in the ion number density. This model was used previously as a neutral model, so that the Poisson equation could be replaced by neutrality.

The third fluid model was the Poisson-consistent detailed model. This model also solved the three fluid conservation equations and the electrostatic Poisson equation. This model solved the electron momentum equation for electron number density, and the Poisson equation for plasma potential. This model required additional boundary conditions for the electron number density, but was otherwise more robust than the non-neutral detailed model.

The electron fluid equations were discretized using the finite difference operators described in Sec. 4.4.

The differential equations for the plasma potential in the non-neutral detailed model and the electron number density in the Poisson-consistent model were complicated and not well characterized in terms of stability. In section 4.5, one dimensional formulations of the differential equations were solved using a one dimensional alternating direction implicit (ADI) solver. The solutions obtained with the ADI solver were in excellent agreement with the exact analytic solutions. This provided confidence that the ADI solver would also be able to obtain stable, accurate solutions on the axisymmetric computational domain.

8.1.3 Faraday probe simulations

The hybrid fluid PIC models were used to simulate the plasma flow around an axisymmetric Faraday probe geometry in Chapter V. Plasma conditions were selected to be representative of the conditions downstream and far off-axis in the plume of a low power Hall thruster. The computational domain was sized from the upstream length of the Bohm sheath solution and the radial dimensions of a JPL Faraday probe. The computational grid spacing was determined from the stability requirements of the fluid model differential equations, and the simulation time step was calculated such that the fastest simulated particles do not travel more than a cell length per iteration.

The hybrid PIC Boltzmann model was used extensively to investigate the effects of the inflow ion distribution on the properties in the sheath and at the surface of the probe. In Sec. 5.3.1 the model was used on a quasi one dimensional computational grid for a direct comparison with the planar Bohm sheath solution. The hybrid fluid PIC model very closely approximated the assumptions of the Bohm sheath solution, and the profiles of the quasi one dimensional results were in excellent agreement with the Bohm sheath profiles for the cold ion case. The hot ion case showed the effect of a higher ion temperature, which leads to a small decrease in local ion number density in the sheath. The collected current at the probe was unaffected.

The hybrid PIC Boltzmann model was next used on the probe geometry computational domain to investigate two dimensional effects. In Sec. 5.3.2 the edge effects are shown to be limited to within 0.0015 m or $2\,\lambda_D$ of the outer radial edge of the probe for both the cold ion case and the hot ion case.

Next the hybrid PIC Boltzmann model was used to simulate the plasma inflow conditions that incrementally approached the complicated composite distribution that consisted of beam, CEX, and double charge ions. The first combination included just beam and CEX ions, as the beam-CEX case. As was described in detail in Sec. 5.3.3, the presence of a second ion component acted to shield the particles from the potential drop until closer to the probe surface. The Bohm sheath solution calculated from the total ion density and bulk Mach number with respect to Bohm velocity was shown to be a good predictor for the number densities and plasma potential in the sheath. The component distributions formed essentially independent sheath structures that were accurately predicted by using the plasma potential and the component freestream Mach number with respect to Bohm velocity.

The beam-CEX-double composite distribution was simulated in the same way, and the same high level of agreement with the Bohm sheath was maintained. Adding a double charge component did not significantly affect the properties of the other components.

The hybrid PIC Boltzmann model was also used to investigate what effects changing the Faraday probe operating conditions had on the collected current. The first of these studies, in Sec. 5.3.4, changed the guard ring bias relative to the collecting surface bias. This created potential gradients and electric fields that would focus ions onto the collecting surface if the guard ring was at a smaller negative bias than the collecting surface. The collected current varied by 12% from the expected freestream current for a difference of 5 V between the collecting surface and the guard ring.

The second study of the effects of changing the Faraday probe operating condition was described in Sec. 5.3.5. The probe bias was varied over a range from 0 V to

-10 V, and the total collected current at each bias was compared to the theoretical total current. The error in the collected current showed a positive correlation with increasing negative bias, which was attributed to sheath expansion. However, the axial velocity was large in this case, and the probe showed less than 2% error over the range of bias potentials.

A comparison of simulated collected current with experimental measurement was made in Sec. 5.3.6. The simulated measurement was in close agreement with the experimental measurement, with less than 3% difference between the two. This level of agreement is somewhat surprising, considering that the simulation parameters were devised from a previous simulation of the BHT-200 plume, and that the details of the beam-CEX ion distribution were not determined rigorously. This reinforced the conclusion that the ion distribution does not have a significant impact on the collected current measurement.

The hybrid PIC non-neutral detailed model was used to simulate the cold ion case in Sec. 5.4. This simulation revealed a problem in the iteration scheme such that the Laplacian of plasma potential remained constant and approximately zero, and the electron density was equal to the ion density as a result. This model was retired since an alternative detailed model was available.

The hybrid PIC Poisson-consistent model was used in Sec. 5.5 to simulate the cold ion case, and produced results that were in excellent agreement with the Bohm sheath solution. The intermediate combinations leading up to the composite distribution were not shown, but two modified beam-CEX-double composite cases were. The cold composite case had a CEX temperature of 300 K, so that there was essentially no backflow in the plasma distribution. The hot composite case had a CEX temperature of 11,600 K, which gave a significant backflow of about 11.5% of the total distribution.

The Poisson-consistent model simulation of the cold composite case produced results that showed the usual good agreement with the Bohm sheath solution. However, the simulation of the hot composite case produced a CEX profile that was well below the Bohm sheath profile throughout the sheath. This discrepancy was discussed and attributed to the assumption made in the Bohm sheath solution that ions have a uniform positive velocity.

In assessment of the model performance, the Bohm sheath solution was shown to be a reliable predictor for plasma properties in the sheath, provided that the ion distribution did not have a significant backflow component. This limitation is loosely related to the Bohm criterion. It was noted that the Poisson-consistent model might be capable of simulating the sheath for plasma conditions where the Bohm criterion was not met and no Bohm sheath solution was available.

8.1.4 Multigrid methods

The simulation time required for the Faraday probe simulations was already 30-35 hours, so the three to four times larger domain required for reversed Faraday probe simulations could not be simulated in a reasonable amount of time. Chapter VI described the analysis of the code performance and the inclusion of a multigrid scheme to speed up the code.

A time profile of the computational code was performed in Sec. 6.1 that identified the particle models as the largest time expense. It was noted that fluid model stability considerations determined the computational cell size, which was much smaller than required for the PIC or DSMC models. A fixed number of particles per cell was enforced to maintain the statistics in the PIC model, leading to an excessive number of particles. A multigrid method was proposed and implemented that allowed the

PIC and DSMC models to be performed on a coarse PIC grid while the fluid models were performed on a fine fluid grid. This was expected to decrease the overall particle count by a factor four, which would speed up the particle routines by a similar factor.

In Sec. 6.3 a time profile of the multigrid version of the code was performed, and the overall speed up factor was shown to be 2.22. This value was slightly better than the expected speed up factor. The simulated properties in the flow field were shown to be essentially unchanged from the previous single grid version of the code, with a maximum error of ±2% relative to the single grid solution. This enabled the reversed Faraday probe simulations to be performed, since the multigrid version obtained the same results as the original version of the code and did so in less than half the total time.

8.1.5 Reversed Faraday probe simulations

In Chapter VII the plasma flow around a reversed Faraday probe was simulated. The Bohm sheath solution could not be used, since the ions did not satisfy the Bohm criterion on the back face of the probe. However, the shadowing sheath model could obtain a solution for the sheath on the back face of the probe. A modified version of the hybrid fluid PIC code was developed in Sec. 7.3 to better approximate the assumptions of the geometric shadowing sheath model and provide a direct comparison. The modifications included deactivating the electron fluid models and the electrostatic acceleration of the PIC model, so the remaining code was just a DSMC model for the ions. This model was called the geometric DSMC model.

The plasma conditions were selected to maintain a small computational domain in order to limit the required computational time. This suggested a Mach number with respect to Bohm velocity of slightly more than one. The ion number density and temperature were otherwise the same as the cold ion case. The computational domain was sized using the kinetic reasoning that the radial diffusion of the fastest particles would be several times faster than the mean radial speed. The domain was made long enough so that particles could diffuse across the diameter of the probe.

The results of the reversed Faraday probe using the shadowing DSMC model were described in Sec. 7.3. The observed flow structures generally reproduced the assumptions used to size the domain. A vacuum region was formed immediately behind the probe. No forces accelerated the particles toward the centerline, so the flow rejoined smoothly at the centerline with no overcompression. The cylindrical surface at the outer edge of the probe was the closest approximation to the one dimensional sheath in the geometric shadowing model. The profile of ion density along that surface was shown to have the same qualitative trends as the geometric sheath model profiles. However, no single value of exchange frequency gave a satisfactory fit of the simulated ion profile. The effective exchange frequency in the shadowing DSMC model appeared to have a functional dependence on the radial velocity, which was not compatible with the assumption of a constant exchange frequency in the geometric shadowing sheath model.

The hybrid PIC Boltzmann model was used to simulated the reversed Faraday probe in Sec. 7.4. The simulated flow field was shown to be much more complicated than predicted by the shadowing DSMC model. The electrostatic sheath created expansion regions upstream and along the side of the probe body. Particles that passed through the sheath on the side of the body were turned toward the centerline, which allowed particles to turn around the edge of the probe without forming a vacuum region. The acceleration toward the centerline also caused the formation of a conical overcompression region about the centerline in the wake downstream of the probe.

The hybrid PIC Poisson-consistent model results in Sec. 7.5 were similar to the Boltzmann model results, except that the contours of plasma potential showed less pronounced curvature throughout the domain. This produced a smaller potential gradient over a larger area that tended to accelerate the particles along the axis of the probe as well as toward the centerline. Combined with the weaker electric fields, the flow was not turned around the edge of the probe as quickly, resulting in a lower density region immediately behind the probe than in the Boltzmann model simulation. Since the axial velocity was higher where the flow converged on the centerline, particles were carried downstream faster. This narrowed the cone and decreased the peak density in the overcompression region.

The simulated exchange frequencies for the shadowing DSMC model and the hybrid PIC models were discussed in Sec. 7.6. The shadowing DSMC showed an approximately constant frequency for particles moving into the wake sheath, but a much lower frequency for particles moving out of the wake sheath. Both of the hybrid models showed a complicated pattern for the exchange frequency that was explained by the orientation of the flow velocity. The geometric shadowing sheath model could not make use of these results, since the exchange frequencies were not constant and were not equal for transfer into and out of the sheath.

8.2 Implications for probe design and technique

The results reported in Chapter V for the standard Faraday probe and in Chapter VII for the reversed Faraday probe can be interpreted to make several recommendations for the design and use of Faraday probes, fulfilling the third major objective of this dissertation.

In Chapter V, hybrid PIC models produce simulated properties near the centerline that are consistently in good agreement with the planar Bohm sheath solutions. This holds true over the full range of inflow plasma conditions, from the cold ion beam case to the beam-CEX-double composite case. Edge effects are observed, but the effects are limited to a few Debye lengths from the outer edge of the probe surface. Additionally, the total collected current at the surface of the probe is always in very good agreement with the theoretical current in the freestream.

The results from the guard ring bias study in Sec. 5.3.4 show that the collected current most accurately matches the theoretical current when the guard ring and collecting surface are biased to the same potential. This is reinforced by observing that the current streamlines to the collecting surface are normal to the surface when the guard ring and collecting surface are biased to the same potential.

The results from the probe bias sweep study in Sec. 5.3.5 show that the collected current matches the theoretical current within about 2% over a broad range of bias potential. There is a gradual increase in the error as the bias voltage is made more negative, which corresponds to sheath expansion. Provided that the plasma has a high axial velocity, the error introduced by sheath expansion will be small.

The recommendations for operation of a Faraday probe are in agreement with the established standard practices:

1. Use a guard ring that is a few Debye lengths wide to prevent edge effects from reaching the collecting surface.

2. Keep the space between the collecting surface and the guard ring smaller than a few Debye lengths to maintain a uniform sheath over the entire collecting surface.

3. Bias the collecting surface and the guard ring to the same potential.
4. Use the smallest bias potential that repels all of the electron current to avoid sheath expansion.

When these recommendations are followed, the collected current at the surface of a Faraday probe accurately reflects the ion current in the freestream.

Recommendations for the reversed Faraday probe are more difficult. Results from the hybrid PIC models in Chapter VII show a complicated wake structure with backflow to the probe and a stagnation point near the back surface of the probe. For a strongly flowing plasma, the current that reaches the back surface of the probe originates upstream of the probe and is turned around the edge of the probe by passing through the electrostatic sheath along the side of the probe body. To avoid interfering with the flow that arrives at the rear face of the probe, features along the side body of the probe should be minimized.

If instead the intention is to measure a backflow current that originates downstream of the probe, it is recommended that the body of the probe be allowed to float to the plasma potential. Then the forward flowing current along the side of the probe body would not be accelerated toward the centerline, and would not turn around the edge of the probe as easily. The bias potential on the rear collecting surface and guard ring should also use the smallest bias potential that still repels the electron current to avoid sheath expansion that might draw in forward flowing current.

8.3 Contributions

In the course of this dissertation a number of unique and original contributions have been made.

- Sec. 3.4: A least-squares fit of exchange frequency is performed to match a geometric shadowing sheath solution to a Bohm sheath solution. This is the first known quantitative assessment of the exchange frequency.
- Sec. 4.5: The differential equations of electron momentum conservation for the non-neutral detailed model and the Poisson-consistent detailed model are characterized as one dimensional constant coefficient differential equations. The use of a one dimensional ADI solver to investigate the stability and accuracy of the model equations had not been performed previously.
- Chapter V: Hybrid fluid PIC models are used for the first time to simulate the flow around a Faraday probe, including a simulated collected current at the probe surface.
- Sec. 5.3.3: Combinations of ion component distributions are simulated, and shown to form independent sheath structures that interact only with the collective plasma potential. The Bohm sheath solution using the average Mach number is shown to be a good predictor of the collective plasma potential and the total ion number density in the sheath.
- Chapter VI: This is the first known instance of a multigrid method being incorporated into a hybrid fluid PIC model.
- Chapter VII: Hybrid fluid PIC models are used for the first time to simulate the flow around a reversed Faraday probe.

- Sec. 7.6: The exchange frequencies into and out of the probe cylinder are simulated for axisymmetric DSMC and hybrid fluid PIC models for the first time.

8.4 Future work

There are several areas in this dissertation where interesting questions remain or where further efforts are needed.

The reversed Faraday probe simulations require a substantial time to run, so only a few basic cases have been simulated at this point. It would be interesting to simulate some of the composite ion distributions to identify whether or not there is significant separation of the different components on the wake side of the probe. It would also be interesting to investigate alternative boundary conditions for the bias potential on the body of the probe, which could help improve the recommendations for use of the reversed Faraday probe.

There is a ready opportunity to use the models in this work to produce simulations for comparison with experiments. Recent experimental investigations of the sheath formed in a plasma with multiple atomic species show that the different species attain significantly different velocities in the sheath [83, 84]. The models in this work are well-suited to consider a similar situation numerically, and would benefit from the generalization involved with simulating other atomic species. The highly successful performance of the Bohm sheath model for composite ion distributions suggests that it might also be useful for the sheaths in multiple ion species plasmas.

One physical effect that could affect probe performance that is not considered in the present work is secondary electron emission (SEE) at the collecting surface of the probe. An emitted electron current is indistinguishable from a collected ion current at the probe surface, and would result in an overestimate of the ion current in the ambient plasma [1]. The computational models described in this work could be modified to include a model for SEE as part of the boundary conditions at the probe surfaces. It is expected that the primary effect of SEE would be to modify the electron properties near the probe surface, but that the ion plasma would not be affected significantly.

With a few minor modifications to the existing computational code, particles could be injected at the downstream edge of the domain, allowing the simulation of weakly flowing plasmas. This would enable the investigation of the reversed Faraday probe for use in a quiescent plasma, and would allow better representation of ion distributions like the hot composite case that have a significant backflow component.

Efforts to extend the multigrid method to an additional level of computational grids could effect another significant speed up in the overall code performance by reducing the particle count by another factor of four. As the multigrid scheme is presently implemented, the fluid equations are only solved on the finest grid. Using a more traditional multigrid approach, the fluid equations could be solved on the coarse grid first, then prolonged and solved on the finer grid. For best results in a multigrid setting, the fluid equation solver should operate quickly rather than accurately. The ADI solver is therefore not well-suited for use in a multigrid scheme. A faster iterative method would be more appropriate.

The Poisson-consistent model is not practical for simulation of an extended plasma, since the fluid model requires fine cell spacing to maintain stability. In a region where the plasma potential is small and gradients in plasma potential are small, significant computational effort is expended to simulate practically neutral flow. This suggests a different sort of hybrid scheme where the Poisson-consistent model is only solved in the non-neutral sheath regions while faster neutral models are solved in the rest of the plasma.

One area for new development is the extension of the hybrid PIC Poisson-consistent model to a three dimensional implementation. The axisymmetric implementation used in this work cannot investigate situations where the plasma velocity is inclined relative to the centerline of the probe.

BIBLIOGRAPHY

BIBLIOGRAPHY

[1] Lieberman, M. A. and Lichtenberg, A. J., *Principle of Plasma Discharges and Materials Processing*, John Wiley and Sons, Inc., New York, NY, 1994.

[2] Langmuir, I., "The interaction of electron and positive ion space charges in cathode sheaths," *Physical Review*, Vol. 33, 1929, pp. 954–989.

[3] Bohm, D., *The Characteristics of Electrical Discharges in Magnetic Fields*, McGraw-Hill, New York, NY, 1949.

[4] Emmert, G. A., Wieland, R. M., Mense, A. T., and Davidson, J. N., "Electric sheath and presheath in a collisionless, finite ion temperature plasma," *Physics of Fluids*, Vol. 23, No. 4, 1980, pp. 803–812.

[5] Hutchinson, I. H., "A fluid theory of ion collection by probes in strong magnetic fields with plasma flow," *Physics of Fluids*, Vol. 30, No. 12, 1987, pp. 3777–3781.

[6] Riemann, K.-U., "Kinetic theory of the plasma sheath transition in a weakly ionized plasma," *Physics of Fluids*, Vol. 24, No. 12, 1981, pp. 2163–2172.

[7] Kaganovich, I. D., "How to patch active and collisionless sheath: a practical guide," *Physics of Plasmas*, Vol. 9, No. 11, 2002, pp. 4788–4793.

[8] Godyak, V. and Sternberg, N., "Good news: you can patch active plasma and collisionless sheath," *IEEE Transactions on Plasma Science*, Vol. 31, No. 2, pp. 303.

[9] Keidar, M. and Beilis, I. I., "Transition from plasma to space-charge sheath near the electrode in electrical discharges," *IEEE Transactions on Plasma Science*, Vol. 33, No. 5, 2005, pp. 1481–1486.

[10] Riemann, K.-U., "Plasma-sheath transition in the kinetic Tonks-Langmuir model," *Physics of Plasmas*, Vol. 13, No. 063508, 2006.

[11] PEPL Images, http://aerospace.engin.umich.edu/spacelab/gallery/Images/images.html.

[12] Walker, M. L. R., Victor, A. L., Hofer, R. R., and Gallimore, A. D., "Effects of backpressure on ion current density measurements in Hall thruster plumes," *Journal of Propulsion and Power*, Vol. 21, No. 3, 2005, pp. 408–415.

[13] Choueiri, E. Y., “A critical history of electric propulsion: the first 50 years (1906-1956),” *Journal of Propulsion and Power*, Vol. 20, No. 2, 2004, pp. 193–203.

[14] Goddard, R. H., *The Green Notebooks, Vol. 1*, The Dr. Robert H. Goddard Collection at Clark University Archives, Clark University, Worceseter, MA.

[15] Artsimovich, L. A., Andronov, I. P., Esipchuk, I. V., Morozov, A. I., Snarsky, R. K., and Kozubsky, K. N., “Development of a stationary plasma thruster (spt) and its testing on the earth artificial satellite Meteor,” *Kosmicheskie Issledovania*, Vol. 12, 1974, pp. 451–468, (in Russian).

[16] Zhurin, V. V., Kaufman, H. R., and Robinson, R. S., “Physics of closed drift thrusters,” *Plasma Sources Science and Technology*, Vol. 8, No. 1, 1999, pp. R1–R21.

[17] Marcucci, M. G. and Polk, J. E., “NSTAR xenon ion thruster on Deep Space 1: ground and flight tests,” *Review of Scientific Instruments*, Vol. 71, No. 3, 2000, pp. 1389–1400.

[18] Kuninaka, H., Nishiyama, K., Funaki, I., Shimizu, Y., Yamada, T., and Kawaguchi, J., “Assessment of plasma interactions and flight status of the Hayabusa asteroid explorer propelled by microwave discharge ion engines,” *IEEE Transactions of Plasma Science*, Vol. 34, No. 5, 2006, pp. 2125–2132.

[19] Milligan, D., Gestal, D., Camino, O., Estublier, D., and Koppel, C., “SMART-1 electric propulsion operations,” *AIAA-2004-3436*, 2004, presented at the 40th AIAA/ASME/SAE/ASEE Joint Propulsion Conference, Fort Lauderdale, FL.

[20] Jahn, R. G., *Physics of electric propulsion, 1st ed.*, McGraw-Hill, New York, NY, 1968.

[21] arcjet, http://www.daviddarling.info/encyclopedia/A/arcjet.html.

[22] XIPS, http://www.daviddarling.info/encyclopedia/X/XIPS.html.

[23] PPT, http://www.daviddarling.info/encyclopedia/P/pulsedplasmathruster.html.

[24] Sackheim, R. L., Wolf, R. S., and Zafran, S., *Space Mission Analysis and Design*, Microcosm, Inc. and Kluwer Academic Publishers, Torrance, CA and Norwell, MA, 1995.

[25] Serway, R. A., *Physics for Scientists and Engineers with Modern Physics, 4th ed.*, Saunders College Publishing, Chicago, IL, 1996.

[26] Biagioni, L., Ceccanti, F., Saverdi, M., Saviozzi, M., and Andrenucci, M., “Qualification status of the FEEP-150 electric micropropulsion subsystem,” *AIAA-2005-4261*, 2005, presented at the 41st AIAA/ASME/SAE/ASEE Joint Propulsion Conference, Tucson, AZ.

[27] Garner, C. E., Brophy, J. R., Polk, J. E., and Pless, L. C., "Cyclic endurance test of a SPT-100 statonary plasma thruster," *AIAA-1994-2856*, 1994, presented at the 30th AIAA/ASME/SAE/ASEE Joint Propulsion Conference, Indianapolis, IN.

[28] Pencil, E. J., Randolph, T., and Manzella, D., "End-of-life stationary plasma thruster far-field plume characterization," *AIAA-1996-2709*, 1996, presented at the 32nd AIAA/ASME/SAE/ASEE Joint Propulsion Conference, Buena Vista, FL.

[29] Britton, M., Waters, D., Messer, R., Sechkar, E., and Banks, B., "Sputtering erosion measurement on boron nitride as a Hall thruster material," *NASA TM-2002-211837*, 2002.

[30] Randolph, T., Pencil, E., and Manzella, D., "Far-field plume contamination and sputtering of the stationary plasma thruster," *AIAA-1996-2709*, 1996, presented at the 30th AIAA/ASME/SAE/ASEE Joint Propulsion Conference, Indianapolis, IN.

[31] Fife, J. M., Hargus, W. A., Jaworske, D. A., Jankovsky, R., Mason, L., Sarmiento, C., Snyder, J. S., Malone, S., Haas, J., and Gallimore, A., "Spacecraft Integration test results of the high performance Hall system SPT-140," *AIAA-2000-3521*, 2000, presented at the 36th AIAA/ASME/SAE/ASEE Joint Propulsion Conference, Huntsville, AL.

[32] Manzella, D., Jankovsky, R., and Hofer, R., "Laboratory model 50 kW Hall thruster," *AIAA-2002-3676*, 2002, presented at the 38th AIAA/ASME/SAE/ASEE Joint Propulsion Conference, Indianapolis, IN.

[33] Hargus, W. A. and Reed, G., "The Air Force clustered Hall thruster program," *AIAA-2002-3678*, 2002, presented at the 38th AIAA/ASME/SAE/ASEE Joint Propulsion Conference, Indianapolis, IN.

[34] Beal, B. E., Gallimore, A. D., and Hargus, W. A., "Preliminary plume characterization of a low-power Hall thruster cluster," *AIAA-2002-4251*, 2002, presented at the 38th AIAA/ASME/SAE/ASEE Joint Propulsion Conference, Indianapolis, IN.

[35] Beal, B. E., Gallimore, A. D., and Hargus, W. A., "The effects of clustering multiple Hall thrusters on plasma plume properties," *AIAA-2003-5155*, 2003, presented at the 39th AIAA/ASME/SAE/ASEE Joint Propulsion Conference, Huntsville, AL.

[36] Peterson, P. Y. and Gallimore, A. D., "The performance and plume characterization of a laboratory gridless ion thruster with closed electron drift acceleration," *AIAA-2004-3936*, 2004, presented at the 40th AIAA/ASME/SAE/ASEE Joint Propulsion Conference, Fort Lauderdale, FL.

[37] Ito, T., Gascon, N., Crawford, W. S., and Capelli, M. A., "Experimental characterization of a micro-Hall thruster," *Journal of Propulsion and Power*, Vol. 23, No. 5, 2007, pp. 1068–1074.

[38] Youngner, D. W., Lu, S. T., Choueiri, E., Neidert, J. B., Black, R. E., Graham, K. J., Fahey, D., Lucus, R., and Zhu, X., "MEMS mega-pixel micro-thruster arrays for small satellite stationkeeping," *AIAA-2004-3936*, 2000, presented at the 14th AIAA/USU Small Satellite Conference, North Logan, UT.

[39] Vacuum Facilities at the Plasmadynamics and Electric Propulsion Laboratory, http://aerospace.engin.umich.edu/spacelab/facilities/facilities.html.

[40] Hutchinson, I. H., *Principles of Plasma Diagnostics*, Cambridge University Press, New York, NY, 1987.

[41] de Grys, K. H., Tilley, D. L., and Aadland, R. S., "BPT Hall thruster plume characteristics," *AIAA-1999-2283*, 1999, presented at the 35th AIAA/ASME/SAE/ASEE Joint Propulsion Conference, Los Angeles, CA.

[42] Rovey, J. L., Walker, M. L. R., and Gallimore, A. D., "Magnetically filtered Faraday probe for measuring the ion current density profile of a Hall thruster," *Review of Scientific Instruments*, Vol. 77, 2006, Art. no. 013503.

[43] Laframboise, J. G., "Theory of spherical and cylindrical Langmuir probes in a collisionless, Maxwellian plasma at rest," *UTIAS Report No. 100*, 1966.

[44] Herman, D. A. and Gallimore, A. D., "A high-speed probe positioning system for interrogating the discharge plasma of a 30 cm ion thruster," *AIAA-2002-4256*, 2002, presented at the 38th AIAA/ASME/SAE/ASEE Joint Propulsion Conference, Indianapolis, IN.

[45] Eckman, R., Byrne, L., Cameron, E., and Gatsonis, N. A., "Triple Langmuir probe measurements in the plume of a pulsed plasma thruster," *AIAA-1998-3806*, 1998, presented at the 34th AIAA/ASME/SAE/ASEE Joint Propulsion Conference, Cleveland, OH.

[46] King, L. B., Gallimore, A. D., and Marrese, C., "Transport-property measurements in the plume of an SPT-100 Hall thruster," *Journal of Propulsion and Power*, Vol. 14, No. 3, 1998, pp. 327–335.

[47] Birdsall, C. K. and Langdon, A. B., *Plasma Physics Via Computer Simulation*, Adam Hilger, Bristol, England, U.K., 1991.

[48] Bird, G. A., *Molecular Gas Dynamics and the Direct Simulation of Gas Flows*, Oxford University Press, New York, NY, 1994.

[49] Sommier, E., Allis, M. K., and Capelli, M. A., "Wall erosion in 2D Hall thruster simulations," *IEPC-2005-189*, 2005, presented at 29th International Electric Propulsion Conference, Princeton, NJ.

[50] Fairweather, G., Gourlay, A. R., and Mitchell, A. R., "Some high accuracy difference schemes with a splitting operator for equations of parabolic and elliptic type," *Numerische Mathematik*, Vol. 10, No. 1, 1967, pp. 56–66.

[51] Yim, J. T., Falk, M., Keidar, M., and Boyd, I. D., "Calculation of Boron Nitride Sputter Yields Under Low Energy Xenon Ion Bombardment," *AIAA-2007-5313*, 2007, presented at 43rd AIAA/ASME/SAE/ASEE Joint Propulsion Conference, Cincinnati, OH.

[52] Boyd, I. D., Scavezze, K., Cai, C., Polk, J. E., and Choueiri, E. Y., "Analysis of plume backflow from a lithium magnetoplasmadynamic thruster," *IEPC-05-014*, 2005, presented at the 29th International Electric Propulsion Conference, Princeton, NJ.

[53] Kim, M., Keidar, M., Boyd, I. D., and Morris, D., "Plasma density reduction using electromagnetic ExB field during reentry flight," *ITC 07-19-03*, 2007, presented at the 43rd ITC/USA Conference, Las Vegas, NV.

[54] Cai, C. and Boyd, I. D., "3D Simulation of Plume Flows from a Cluster of Plasma Thrusters," *AIAA-2005-4662*, 2005, presented at the 36th AIAA Plasmadynamics and Lasers Conference, Toronto, Ontario.

[55] Alexeenko, A. A., Fedosov, D. A., Gimelshein, S. F., Levin, D. A., and Collins, R. J., "Transient heat transfer and gas flow in a MEMS-based thruster," *Journal of Microelectromechanical Systems*, Vol. 15, No. 1, 2006, pp. 181–194.

[56] Yim, J. T., Keidar, M., and Boyd, I. D., "An Investigation of Factors Involved in Hall Thruster Wall Erosion Modeling," *AIAA-2006-4657*, 2006, presented at the 42nd AIAA/ASME/SAE/ASEE Joint Propulsion Conference, Sacramento, California.

[57] Y., C., Keidar, M., and Boyd, I. D., "Effect of a Magnetic Field in Simulating the Very Near-Field Plume of an Anode Layer Hall Thruster," 2007, presented at 43rd AIAA/ASME/SAE/ASEE Joint Propulsion Conference, Cincinnati, OH.

[58] Chen, F. F., *Introduction to Plasma Physics and Controlled Fusion, Vol. 1: Plasma Physics, 2nd ed.*, Plenum Press, New York, NY, 1984.

[59] Gombosi, T. I., *Gaskinetic Theory*, Cambridge University Press, New York, NY, 1994.

[60] Mitchner, M. and Kruger, C. H., *Partially Ionized Gases*, John Wiley and Sons, Inc., New York, NY, 1992.

[61] Vincenti, W. G. and Kruger, C. H., *Introduction to Physical Gas Dynamics*, Krieger Publishing Company, Malabar, FL, 2002.

[62] Allis, W. P., Buchsbaum, S. J., and Bers, A., *Waves in Anisotropic Plasmas*, MIT Press, Cambridge, MA, 1963.

[63] Boyd, T. J. M. and Sanderson, J. J., *The Physics of Plasmas*, Cambridge University Press, Cambridge, United Kingdom, 2003.

[64] Chung, K.-S. and Hutchinson, I. H., "Kinetic theory of ion collection by probing objects in flowing strongly magnetized plasmas," *Physical Review A*, Vol. 38, No. 9, 1988, pp. 4721–4731.

[65] Chung, K.-S. and Hutchinson, I. H., "Effects of a generalized presheath source in flowing magnetized plasmas," *Physics of Fluids B*, Vol. 3, No. 11, 1991, pp. 3053–3058.

[66] Valsaque, F., Manfredi, G., Gunn, J. P., and Gauthier, E., "Kinetic simulations of ion temperature measurements from retarding field analyzers," *Physics of Plasmas*, Vol. 9, No. 5, 2002, pp. 1806–1814.

[67] Schwartzentruber, T. E., Scalabrin, L. C., and Boyd, I. D., "A modular particle-continuum method for hypersonic non-equilibrium gas flows," *Journal of Computational Physics*, Vol. 225, No. 1, 2007, pp. 1159–1174.

[68] Oh, D. Y., Hastings, D. E., Marrese, C. M., Haas, J. M., and Gallimore, A. D., "Modeling of Stationary Plasma Thruster-100 thruster plumes and implications for satellite design," *Journal of Propulsion and Power*, Vol. 15, No. 2, 1999, pp. 345–357.

[69] VanGilder, D. B., Boyd, I. D., and Keidar, M., "Particle simulations of a Hall thruster plume," *Journal of Spacecraft and Rockets*, Vol. 37, No. 1, 2000, pp. 129–136.

[70] Celik, M., Santi, M., Cheng, S., Martinez-Sanchez, M., and Peraire, J., "Hybrid-PIC simulation of a Hall thruster plume on an unstructured grid with DSMC collisions," *IEPC-03-134*, 2003, presented at the 28th International Electric Propulsion Conference, Toulouse, France.

[71] Pullins, S., Dressler, R. A., Chiu, Y.-H., and Levandier, D. J., "Ion dynamics in Hall effect and Ion thrusters: Xe+ + Xe symmetric charge transfer," *AIAA-2000-0603*, 2000, presented at the 38th Aerospace Sciences Meeting, Reno, NV.

[72] McEachran, R. P. and Stauffer, A. D., "Relativistic low-energy elastic and momentum transfer cross sections for electron scattering from xenon," *Journal of Physics B: Atomic and Molecular Physics*, Vol. 20, No. 14, 1987, pp. 3483–3486.

[73] Boyd, I. D. and Yim, J. T., "Modeling of the near field plume of a Hall thruster," *Journal of Applied Physics*, Vol. 95, No. 9, 2004, pp. 4575–4584.

[74] Peaceman, D. W. and Rachford, H. H., "The numerical solution of parabolic and elliptic differential equations," *Journal of the Society for Industrial and Applied Mathematics*, Vol. 3, No. 1, 1955, pp. 28–41.

[75] Teukolsky, S. A., Vetterling, W. T., Flannery, B. P., and Metcalf, M., *Numerical Recipes in Fortran 90: the art of parallel scientific computing*, Cambridge University Press, New York, NY, 1999.

[76] Inman, D. J., *Engineering Vibration*, Prentice Hall, Englewood Cliffs, NJ, 1994.

[77] Ma, T., "Quantification with two-dimensional spatial resolution of the ion flux emitted from a 200 W Hall effect thruster," 2004, California Institute of Technology, Pasadena, CA (unpublished).

[78] Ekholm, J. M. and Hargus, W. A., "ExB measurements of a 200W xenon Hall thruster," *AIAA-2005-4405*, 2005, presented at the 41st AIAA/ASME/SAE/ASEE Joint Propulsion Conference, Tucson, AZ.

[79] Hofer, R. R. and Gallimore, A. D., "Ion species fractions in the far-field plume of a high-specific impulse Hall thruster," *AIAA-2003-5001*, 2003, presented at the 39th AIAA/ASME/SAE/ASEE Joint Propulsion Conference, Huntsville, AL.

[80] Gallimore, A. D., "Near- and far-field characterization of stationary plasma thruster plumes," *Journal of Spacecraft and Rockets*, Vol. 38, No. 3, 2001, pp. 441–453.

[81] Briggs, W. L., *A multigrid tutorial*, Society for Indistrial and Applied Mathematics, Philadelphia, PA, 1987.

[82] Wesseling, P., *An introduction to multigrid methods*, John Wiley, New York, NY, 1992.

[83] Severn, G. D., Wang, X., Eunsuk, K., and Hershkowitz, N., "Experimental studies of the Bohm criterion in a two-ion-species plasma using laser-induced fluorescence," *Physical Review Letters*, Vol. 90, No. 14, 2003, 145001.

[84] Severn, G. D., Wang, X., Eunsuk, K., Hershkowitz, N., Turner, M. M., and McWilliams, R., "Ion flow and sheath physics studies in multiple ion species plasmas using diode based laser-induced fluorescence," *Thin Solid Films*, Vol. 506, 2006, pp. 674–678.